Photodissociation Dynamics of Triatomic van der Waals Molecules

Thesis by

Joseph Isaac Cline III

In Partial Fulfillment of the Requirements

for the Degree of

Doctor of Philosophy

California Institute of Technology

Pasadena, California

1988

(Submitted January 18, 1988)

Acknowledgements

I acknowledge my advisor, Ken Janda, for his leadership, advice, and friendship throughout my graduate career. His interest in the fundamental physics of chemistry has guided my own thinking about scientific problems, and his approach to science as a discipline, not as a business, has helped me to keep my perspective. Ken fostered a spirit of mutual support and sacrifice within his research group that is refreshing in an intensely competitive world.

I thank my fellow Techers Dwight Evard, Sally Hair, and Brian Reid for their many contributions to the work in this thesis and for many good times when we weren't working. I will always remember the camaraderie we shared that made the dreaded move to Pittsburgh something of an adventure. Dwight had a hand in most of the experiments in this thesis, while Sally's bright personality and wit kept me smiling through all but the cloudiest times. I greatly appreciate many wide-ranging, always fruitful scientific discussions with Brian. Without his help I would have never completed the theoretical calculations on $HeCl_2$. I also thank Fritz Thommen and Francis Celii for getting me started in the lab at Caltech, and for great adventures outside the lab.

N. Sivakumar deserves much of the credit for the

early pump-probe experiments at Pitt. We spent many long, often exciting nights in the lab together, which easily constitute the highlights of the work in this thesis. Siva's endurance and persistence as an experimentalist and his easy-going personality made him an ideal collaborator.

I also acknowledge many helpful conversations with Alberto Beswick and Nadine Halberstadt about the theoretical aspects of this work during their visits to Pittsburgh. Nadine supplied the programs that form the backbone of the $HeCl_2$ calculations in Chapter 3.

I thank Mike Sherman for his friendship and for keeping me physically fit and sane while in the "Boig." Craig Bieler deserves credit for assisting me with the last of the experiments I did in Pittsburgh. Craig, Sally Brian, and Jeff Tomer deserve special thanks for proofreading and helping to assemble this thesis. Thanks go to Rob Coalson for generously allowing me the use of his laser printer over the last year.

I thank my parents and family for their unwavering support and confidence, which played an indispensable role in seeing me through the crises of the last few years.

Finally, I gratefully acknowledge the National Science Foundation for a predoctoral fellowship and the financial support that made possible all of the research in this thesis.

Abstract

The spectroscopy and vibrational predissociation dynamics of triatomic van der Waals molecules are studied experimentally and theoretically at the state-to-state level of detail.

Laser-induced fluorescence spectra of $HeCl_2$ are measured and the geometry and vibrational predissociation rate are obtained by a rotational analysis of the spectra and the determination of homogenous linewidths. A laser pump-probe technique is used to measure the vibrational and rotational state population distribution of the product Cl_2. Although the Cl_2 fragment has little rotational energy, its rotational distribution is bimodal. A symmetry selection rule for the dissociation results from the symmetry of the $He\cdots Cl_2$ van der Waals potential. Quantum mechanical calculations on a realistic potential energy surface are successful in modeling the experimental spectroscopy and dynamics.

The vibrational predissociation dynamics of $NeCl_2$ is also measured using the pump-probe technique. In this case the Cl_2 fragment shows significantly more rotational excitation than in the dissociation of $HeCl_2$. The rotational distributions are bimodal and are relatively independent of the energy of the prepared state. The $NeCl_2$ binding energy is estimated from thresholds for the

populations of fragment rotational levels.

The vibrational predissociation of $NeBr_2$ is studied by dispersing the fluorescence of the Br_2 fragment. The product Br_2 is rotationally cold. The closure of vibrational product channels is used to determine the binding energy of the molecule.

Table of Contents

List of Figures

List of Tables

Chapter 1

Introduction

The research in this thesis concerns a basic dynamical problem. Consider the triatomic molecule ABC depicted in Fig. 1. If ABC has a non-linear geometry, then the molecule has 3 vibrational degrees of freedom: an A-B stretching motion, R; a C-(AB) stretching motion, r; and a bending vibration, γ. Furthermore, assume that the A-B potential energy surface is very deep and the A-B stretching frequency is very high relative to a shallow C-(AB) potential and low C-(AB) vibrational frequency. If vibrational energy is initially deposited into the A-B stretch in excess of the well depth of the C-(AB) potential, then any coupling among the vibrations will eventually lead to dissociation of the molecule. Since the frequency mismatch of the two vibrations is large, the coupling is inefficient and the dissociation process is relatively slow. The quantum numbers of the dissociating state can then be well defined.

This problem, vibrational predissociation, is of fundamental importance in chemical physics, and is the central topic of this thesis. It is closely related to a variety of other chemical phenomena, for example, intramolecular vibrational energy redistribution (IVR) and vibrationally and rotationally inelastic collisions. The formal theory often used to describe vibrational predissociation, that of the decay a zero-order, bound,

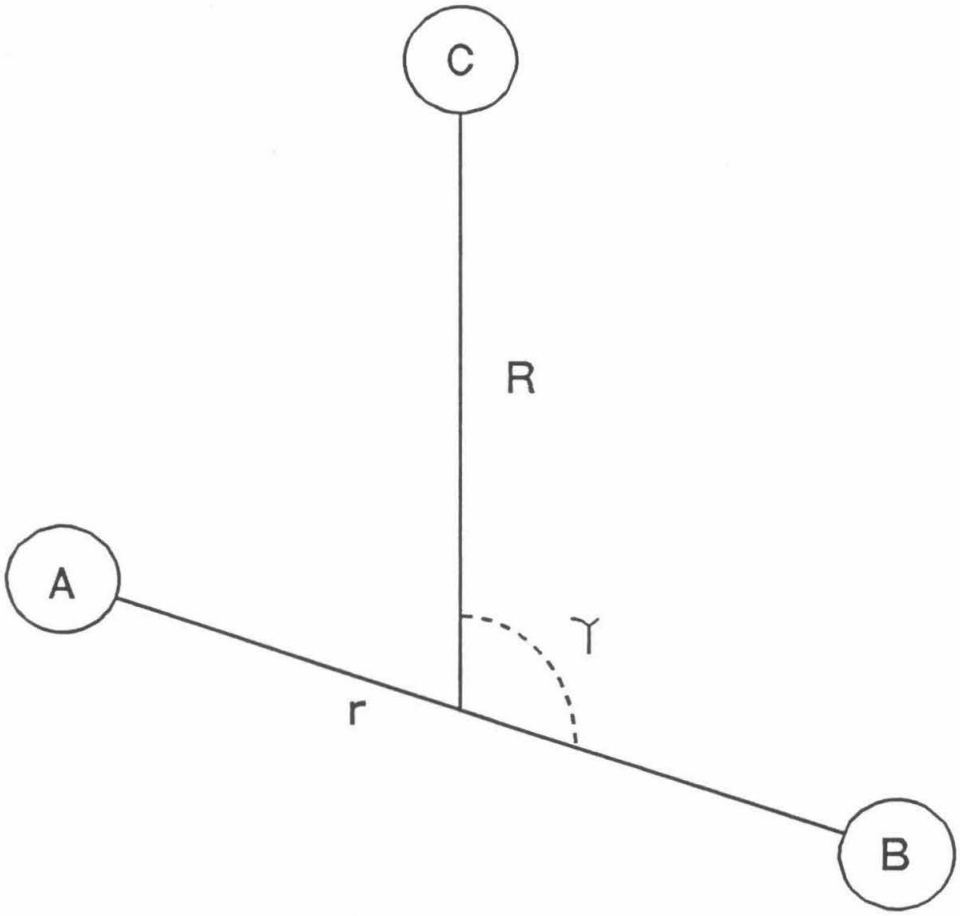

FIG. 1. Vibrational degrees of freedom for molecule ABC.

state embedded in a continuum,[1,2] is analogous to that for many other processes such as the radiative and non-radiative decay of electronically excited states.[3,4]

The questions explored in this thesis are, for a given potential energy surface and atomic masses, how rapidly the initially prepared state decays, and what the vibrational and rotational quantum states of the recoiling fragments are. Furthermore, we want to understand how changing the masses and the potential energy surface alters the dynamics of the molecule. This work has succeeded in experimentally measuring and theoretically calculating all the relevant degrees of freedom for such a process at the state-to-state level of detail.

van der Waals molecules[5] are excellent candidates for studies of this type because the dissociation dynamics generally occurs on a single electronic potential energy surface. The research in this thesis concerns a specific class of van der Waals molecules: the rare-gas halogen complexes. These molecules have additional characteristics that have made them the topic of many experimental and theoretical studies: First, the halogens have optical transitions to very long-lived, excited electronic states that fall in the range easily accessed by tunable lasers. Second, these transitions are very well characterized, so that the understanding of the closely related spectroscopy of the van der Waals species

is simplified. Third, vibrational predissociation is, in many cases, sufficiently slow that the molecule can be prepared in a quasibound state with precisely known electronic, vibrational, and rotational quantum numbers. Finally, the dynamics of these complexes is surprisingly rich, ranging from a nearly pure vibrational to translational energy transfer process in HeI_2,[6] to rotational rainbow phenomena in rare-gas ICl complexes,[7] observation of interference effects in $HeCl_2$,[8] to multistep IVR processes in $ArCl_2$.[9] The rare-gas halogens have also been intensively studied, theoretically,[10,13] because they constitute invitingly simple dynamical systems for which detailed calculations on realistic potential energy surfaces can be quantitatively compared to experimental data.

This thesis presents research on the vibrational predissociation of $HeCl_2$, $NeCl_2$, and $NeBr_2$, organized in order of increasing mass of the complex. In each case a quasibound vibrational level of the B electronically excited state of the molecule is prepared by a tunable dye laser pulse. The quantum state of the halogen fragment following decomposition is determined either by a second probe laser pulse or by dispersion of the fluorescence of the halogen fragment following dissociation. Because of the larger rotational constants of $HeCl_2$, it is possible to perform truly state-selected experiments that

are compared to detailed theoretical analysis, whereas the small rotational constants of $NeBr_2$ prevent rotational state resolution of the dynamics.

Chapter 2 of this thesis describes the laser-induced fluorescence spectrum of the B⟵X transition of $HeCl_2$. The rotational structure of individual vibrational bands is analyzed to obtain information about the molecular geometry, and the homogeneous broadening of the spectra is measured to obtain the decay rate of the quasibound state.

The experiment described in Chapter 3 uses the laser pump-probe technique to examine the dynamics of $HeCl_2$. It is possible to measure the product state distribution for decomposition of individual rotational levels of the complex. Although only a small fraction of the energy released during dissociation goes into rotational excitation of the products, the Cl_2 fragment shows an unusual bimodal rotational population distribution. A realistic potential energy surface is constructed for $He\cdots Cl_2$ for which three-dimensional quantum calculations agree with the measured spectroscopy. Use of the golden rule approximation in a quantum mechanical calculation of the dynamics gives good agreement with the experimental data. This work represents one of the most complete experimental and theoretical studies of vibrational predissociation yet performed for any molecule.

Chapter 4 discusses the vibrational predissociation

of $NeCl_2$, thus increasing the mass of atom C in Fig. 1. The Cl_2 fragment shows considerably more rotational excitation than in the dissociation of $HeCl_2$; all rotational levels allowed by conservation of energy are populated. A bimodal rotational population is also observed. The bond energy of $NeCl_2$ is obtained by the measurement of thresholds for the production of particular fragment rotational levels.

The effect of increasing the mass of the diatom AB is explored in Chapter 5, which presents a study of the vibrational predissociation of $NeBr_2$. The state of the Br_2 fragment is obtained by dispersing its fluorescence following dissociation. The larger rotational inertia of the Br_2 fragment results in significantly less rotational excitation than in the decomposition of $NeCl_2$. The binding energy of $NeBr_2$ is obtained by analysis of the partitioning of the fragments among the available vibrational product channels.

This research shows that, while the gross vibrational predissociation dynamics of these molecules is mostly consistent with the previous understanding of this process, rotationally resolved, state-to-state studies reveal new and exciting phenomena. It is shown that the symmetry of the van der Waals potential leads to dynamical selection rules in photodissociation analogous to those of inelastic scattering. Despite the fact that 3-dimensional

quantum calculations reproduce the experimentally observed rotational distributions of He- and Ne- Cl_2, they cannot be explained in terms of a simple physical model for the process. These results are exciting candidates for further semiclassical studies. Finally, the structural and binding energy information obtained in this research contributes to the general understanding of weak intermolecular forces.

REFERENCES

[1]A good introduction to this problem is given in C. Cohen-Tannoudji, B. Diu, and F. Laloë, *Quantum Mechanics*, Vol. 2 (Wiley, New York, 1977), p. 1343.

[2]U. Fano, Phys. Rev. **124**, 1866 (1961).

[3]M. Bixon and J. Jortner, J. Chem. Phys. **48**, 715 (1968).

[4]M. Bixon and J. Jortner, J. Chem. Phys. **50**, 4061 (1969).

[5]An introduction to the properties of van der Waals molecules is given in B.L. Blaney and G.E. Ewing, Ann. Rev. Phys. Chem. **27**, 533 (1976).

[6]D.H. Levy, Adv. Chem. Phys. **47**, 323 (1981).

[7]J.C. Drobits, J.M. Skene, and M.I. Lester, unpublished results presented at the Conference on the Dynamics of Molecular Collisions, July 1987, Wheeling, WV.

[8]Chapter 3 of this thesis.

[9]D.D. Evard, J.I. Cline, and K.C. Janda, manuscript in preparation; D.D. Evard, Ph.D. Thesis, California Institute of Technology, 1988.

[10]J.A. Beswick and J. Jortner, Adv. Chem. Phys. **47**, 363 (1981).

[11]N. Halberstadt, J.A. Beswick, and K.C. Janda, J. Chem. Phys. **87**, 3966 (1987).

[12]S.K. Gray, S.A. Rice, and M.J. Davis, J. Phys. Chem. **90**, 3470 (1986).

[13]S.B. Woodruff and D.L. Thompson, J. Chem. Phys. **71**, 376 (1979).

Chapter 2

The Laser-Induced Fluorescence Spectrum of the $HeCl_2$ van der Waals Molecule†

†Published in a similar form in J. Chem. Phys. **84**, 1165 (1986).

The Laser-Induced Fluorescence Spectrum of the $HeCl_2$ van der Waals Molecule

Joseph I. Cline,[a] Dwight D. Evard, Fritz Thommen,[b] and Kenneth C. Janda[c]

The Arthur Amos Noyes Laboratory of Chemical Physics,[d]
California Institute of Technology,
Pasadena, California 91125

ABSTRACT
Laser-induced fluorescence excitation spectra of free-jet expansions of He and Cl_2 have been recorded. Spectroscopic features observed ~ 3.5 cm^{-1} to the blue of the free $^{35}Cl_2$ vibronic origins of the 7-0 through the 12-0 bands of the $B^3\Pi(0_u^+) \leftarrow X^1\Sigma_g^+$ system were attributed to the $He^{35}Cl_2$ molecule. The observed spectra were well simulated by a T-shaped, rigid, asymmetric top model. The spectra were observed to display homogeneous broadening dependent on the vibrational band excited. Predissociation lifetimes were calculated and structural parameters determined by fitting the observed contours. The distance from the He atom to the Cl_2 center of mass is 3.8 ± 0.4 and 3.9 ± 0.4 Å for the ground and excited states, respectively.

[a] National Science Foundation Predoctoral Fellow.
[b] Present address: CIBA-Geigy, Basel, Switzerland.
[c] Camille and Henry Dreyfus Teacher-Scholar.
[d] Contribution No. 7283.

I. INTRODUCTION

van der Waals molecules consisting of a rare gas atom weakly bound to a diatomic molecule provide a simple system for which fundamental theories of molecular dynamical processes may be tested. The decay rate of a state vibrationally excited in the diatomic stretch is a strong function of how efficiently that state couples to a continuum of dissociative final states of the atom-diatom system. Spectral line broadening provides a means of measuring this rate.

The rare gas dihalogens (AX_2) provide systems well suited for such studies. The $B^3\Pi(0_u^+) \longleftarrow X^1\Sigma_g^+$ electronic transition has been carefully studied for the dihalogens, which greatly aids in the analysis of the van der Waals molecule spectra. The triatomic van der Waals molecule can be prepared in a free-jet expansion and is detected a few wavenumbers to the blue of the free diatomic vibrational bandheads. The rare gas atom only weakly perturbs the electronic structure of the halogen component. Fluorescence lifetimes for Cl_2, Br_2, and I_2 are $> 10^6$ s, whereas homogeneous linewidths indicate vibrational predissociation lifetimes of less than $\sim 10^{-9}$ s. Thus, dissociation occurs on the potential surface of one electronic state.

The pioneering work of Levy and co-workers[1-5]

characterized the general features of the dynamics of these systems in their studies of HeI_2. They determined that HeI_2 prepared in a vibrational state υ' dissociates, yielding an I_2 fragment in the $\upsilon'-1$ vibrational state with little rotational excitation. The structure of HeI_2 was determined to be triangular, the He atom being on the perpendicular bisector of the I_2 bond axis. Subsequently, ArI_2 and NeI_2,[1-5] $NeCl_2$,[6,7] $NeBr_2$,[8,10] and $HeBr_2$[11] have been studied.

Here we report the excitation spectrum of the $HeCl_2$ molecule. At this time a large body of data exists on these molecules, allowing comparisons to be made that reveal the nature of the dissociation dynamics and van der Waals molecular structure. All of these molecules share a T-shaped geometry and have vibrational state-dependent, dissociation rates consistent with the $\Delta\upsilon' = -1$ propensity rule, provided one quantum is sufficient to break the van der Waals bond. In addition, there is evidence that the lighter diatomic fragments may exhibit significantly greater rotational excitation than I_2.

Numerous theoretical approaches to the vibrational predissociation of HeI_2 have been made.[12-16] The results reproduce the experimentally observed I_2 fragment's rotational and vibrational state distributions. Beswick and Jortner[12] and Ewing[15] have given general equations that reproduce the trends in dissociation rates as a

function of υ' for AX_2 species. The diatomic and van der Waals potentials are assumed to be separable to zero order, and the spectroscopically prepared state has υ' quanta in the diatomic mode and a relative translational energy along the van der Waals coordinate equal to the diatomic vibrational spacing, $E_{\upsilon'}-E_{\upsilon'-1}$, less the dissociation energy of the van der Waals bond. The dissociation rate is roughly proportional to the square of the matrix element between the initial van der Waals wave function coupled by the potential perturbation operator to a rapidly oscillating plane wave with the relative translational energy of the dissociation. This "energy-gap" or "momentum-gap" model predicts that accessible states with rotational (or vibrational) excitation will have larger matrix elements because of a reduced relative translational energy.

In this paper we show that the observed trend in the $HeCl_2$ predissociation rate is consistent with this model. Structural information is obtained by a rotational analysis of the spectra. The results are compared to previous studies of related complexes.

II. EXPERIMENTAL

The experimental apparatus used was similar to one previously described,[6] except that a continuous nozzle expansion was used to form the jet. Liquid Cl_2 was

maintained at 233-243 K under He at a total pressure of typically 600 psi. The gaseous mixture of He and Cl_2 vapor was expanded through a 25 μm nozzle mounted on an *xyz* translatable stage into a vacuum chamber maintained at pressures below 10^{-4} Torr.

A Lumonics 861-S pulsed excimer laser operating on XeCl was used to pump a Lambda Physik FL2002E dye laser equipped with a Fabry-Perot air-spaced etalon. This laser produces 1-3 mJ pulses with a linewidth of 0.04 cm^{-1}. The laser beam was focused through brewster angle windows and light baffles to intersect the molecular beam at a right angle. Laser-induced fluorescence was collected perpendicular to the plane of the molecular and laser beams and detected by an S-20 photomultiplier. Scattered laser light was filtered by appropriate Schott glass filters (OG-515,530). Spectra were normalized to laser pulse energy by a Gen-Tec energy meter, which measured the beam energy as it left the apparatus. The total fluorescence signal from the photomultiplier and the signal from the energy meter were recorded by either a homebuilt MCSA or Stanford Research Systmes boxcar integrators. Both the MCSA and the boxcars were interfaced to an IBM-PC microcomputer through a Tecmar Labmaster interface. The microcomputer controlled the scanning of the dye laser and signal acquisition and averaging.

III. RESULTS

The laser-induced fluorescence spectrum of the free jet expansion in the region of the $^{35}Cl_2$ $B^3\Pi(0_u^+) \leftarrow X^1\Sigma_g^+$ (11←0) band is shown in Fig. 1. The feature approximately 3.7 cm^{-1} to the blue of the Cl_2 bandhead disappears at reduced backing pressures. This peak, analogous to those observed for $NeCl_2$, HeI_2, and $HeBr_2$, is attributed to the $HeCl_2$ van der Waals molecule. Similar spectra were recorded for the 7←0 through 12←0 bands of the Cl_2 B←X transition.

Excitation spectra of the corresponding free Cl_2 bands were fit to a rigid rotor model, which included nuclear spin statistics. Literature values[17] were used for the rotational constants of the X and B electronic states, while the rotational temperature and inhomogeneous linewidth were optimized by a least-squares technique. The inhomogeneous linewidth includes contributions from the laser bandwidth and Doppler broadening. Typical rotational temperatures were 1 K and inhomogeneous linewidths were 0.07 cm^{-1}.

Averaged $He^{35}Cl_2$ spectra and computer-generated fits are shown in Figs. 2 and 3 for the 11←0 and 8←0 bands. $HeCl_2$ spectra were fit, assuming a T-shaped structure. The Cl_2 bond length in the van der Waals molecule was assumed to be identical to that reported for the

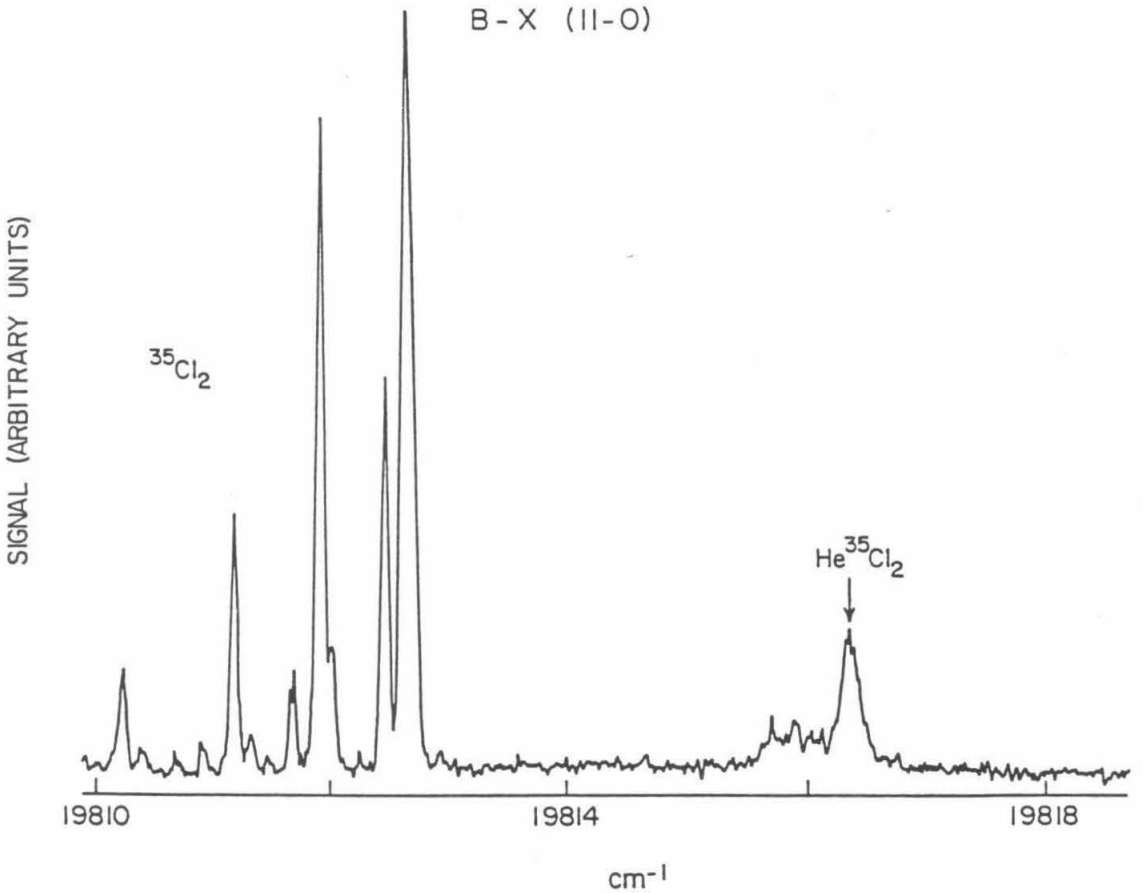

FIG. 1. Excitation spectrum about the $^{35}Cl_2$ 11⟵0 bandhead at 0.04 cm^{-1} laser resolution. The more intense lines of free Cl_2 are not to scale because of saturation of the detection electronics.

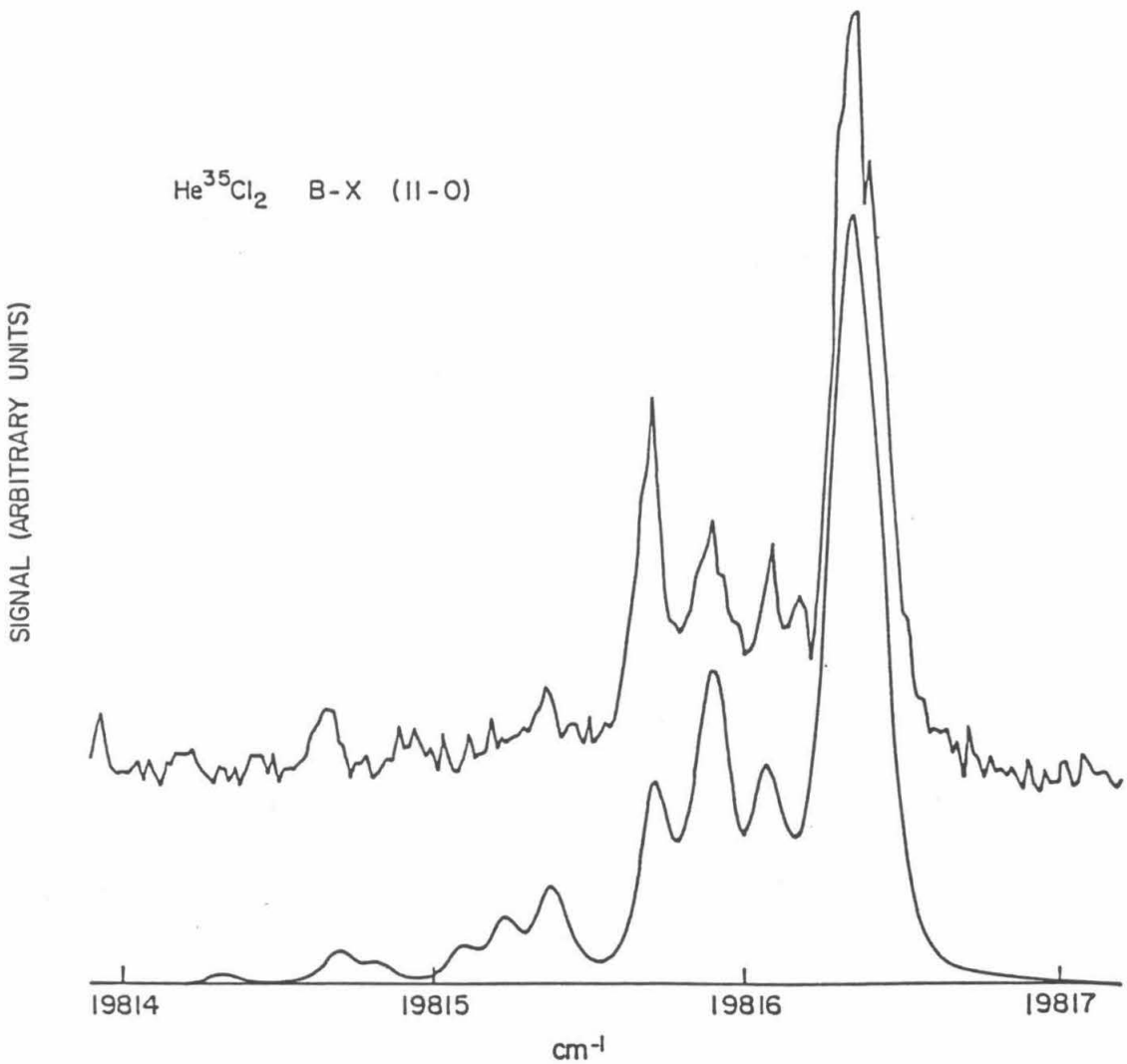

FIG. 2. Excitation spectrum of the He^{35}Cl$_2$ 11←0 band at 0.04 cm^{-1} laser resolution. Upper trace is the experimental spectrum. The lower trace is the computer-generated fit, assuming a T-shaped structure.

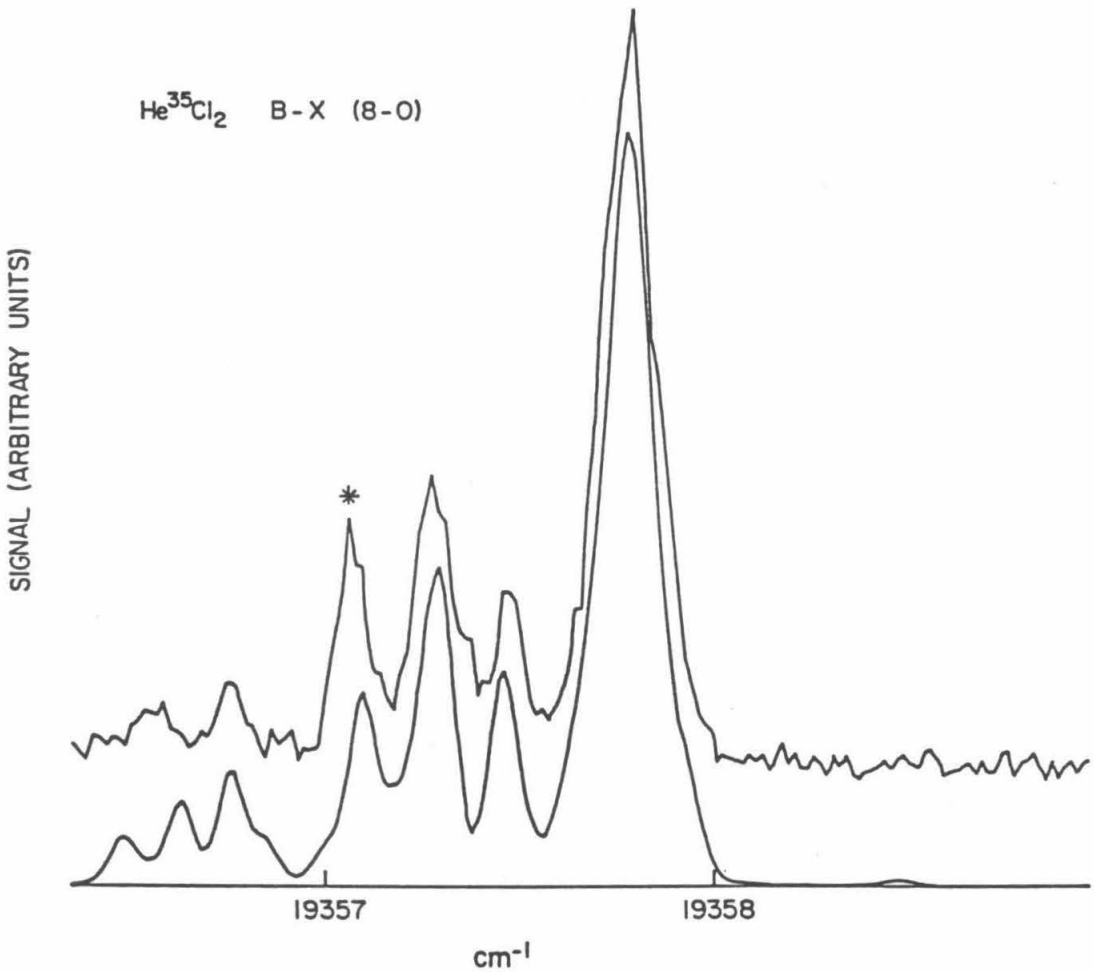

FIG. 3. Excitation spectrum of the $He^{35}Cl_2$ 8←0 band at 0.04 cm^{-1} laser resolution. Upper trace is the experimental spectrum. The lower trace is the computer-generated fit, assuming a T-shaped structure.

uncomplexed molecule.[17] The inhomogeneous linewidth and rotational temperature determined in the Cl_2 fit were used as fixed values in the analysis of the corresponding $He^{35}Cl_2$ bands. The distance from the He atom to the Cl_2 center of mass, R_X and R_B, for the ground and excited electronic states, the band origin, and the homogeneous linewidth was varied in the fit to a rigid, asymmetric top Hamiltonian. Band origins of $HeCl_2$ were computed relative to the band origins of the adjacent $^{35}Cl_2$ peaks, which were set to their literature values.[17] The results of these simulations show that the band contour is quite sensitive to the difference (R_X-R_B) and somewhat less sensitive to the absolute values of R_X and R_B. The 8⟵0 and 9⟵0 bands could be simulated closely and the fits yielded similar values for R_X. The absolute value of R_X did not have a clear effect on the quality of the fit in the simulations of the υ' = 10-12 bands over the range 3.4-4.0 Å. Since the same R_X is common to all measured bands, the average, R_X = 3.8 Å, for the 8⟵0 and 9⟵0 bands was taken as the optimum value. All bands were then fit again with this R_X as a fixed parameter. The results of these calculations are summarized in Table 1. The values of R_B calculated by this procedure did not vary systematically with υ'. The average value of R_B over the measured bands was 3.937 Å The error in (R_B-R_X) is taken as 0.024 Å, the standard deviation of this average.

Table 1 : $He^{35}Cl_2$ spectral shifts and estimated linewidths

Band	$\nu_{00}(Cl_2)$*	$\nu_{00}(HeCl_2)$	shift cm^{-1}	Γ(FWHM) cm^{-1}	τ (ps)
7-0	19179.307	19182.71	3.40	-	-
8-0	19353.976	19357.47	3.49	0.0105±0.0016	506±77
9-0	19517.746	19521.30	3.55	0.0193±0.0032	275±45
10-0	19670.509	19674.16	3.65	0.0296±0.0035	179±21
11-0	19812.366	19816.09	3.72	0.0546±0.0019	97.2±3.4
12-0	19943.386	19947.16	3.77	0.1014±0.0014	52.37±0.72

$R_X = 3.8 \pm 0.4$Å

$R_B - R_X = 0.127 \pm 0.024$Å

* From Reference 17

Assigning error limits to the absolute determination of R_X is not straightforward. The feature indicated by an asterisk in Fig. 3 is attributed to a single, nearly unblended line, assigned to the $0_{00} \leftarrow 1_{01}$ transition. The position of this line with respect to the band origin is a function only of R_X. Since the band origin as determined by the fit was relatively insensitive to the absolute value of R_X over a wide range, the position of this line relative to the band origin allows an absolute determination of R_X. Estimating the error in the determination of this transition to be the laser linewidth, the error in R_X is ± 1 Å. This is probably an overly conservative estimate. Fitting the entire spectrum over a wide range of R_X shows that the fit to the overall contour is more sensitve than these error bars would indicate. Our experience in varying R_X over a wide range indicates that an uncertainty of ± 0.4 Å is more reasonable. Changing R_X by this amount corresponds to an increase in the sum of the squares of the error by 25 to 100 % and a qualitatively poor fit to the data. It should also be noted that centrifugal distortion in this weak bond could be significant and that these spectra contain lines of appreciable intensity with J as high as 4. Quoted errors in the fitted homogeneous linewidths, Γ, are the 95 % confidence limits. The errors in the band shifts are taken to be the laser linewidth. Weak Franck-Condon

factors and narrow homogeneous linewidths prevented reliable determination of predissociation lifetimes and van der Waals radii for $HeCl_2$ bands with $\upsilon' \lesssim 7$.

IV. DISCUSSION

Three quantities have been measured for the $HeCl_2$ molecule, which can be compared to previous studies of other rare gas halogen complexes. These are the band shift, the van der Waals bond length, and the vibrational predissociation lifetime.

The blue shift of the $He^{35}Cl_2$ band origin relative to that of the free $^{35}Cl_2$ increases roughly linearly with respect to the B state vibrational quantum number, υ'. This result is analogous to the smooth increase in the blue shift observed in HeI_2 and $HeBr_2$ but differs significantly from the $NeCl_2$ data,[7] where the band shifts fluctuate with υ'.

A commonly used model for these systems is one in which the rare gas atom feels the "effective potential" of the halogen atoms, which move in a deep potential well. This approach is analogous to the Born-Oppenheimer separation of electronic and nuclear motion. In this model the existence of a blue shift indicates that the effective van der Waals potential in the X state is deeper than that in the B state. Hence an increasing blue shift indicates simply that the B state van der Waals well depth

decreases with increasing υ'. The physical basis of such an increasing shift would be the change in the van der Waals potential surface because of an increase in the expectation value of the Cl_2 bond length with υ'. An alternative model that suggests an explanation for this increase is to consider the perturbation of the Cl-Cl potential because of the presence of the He atom. Using a simple atom-atom pairwise potential model (described more fully below), the Cl-Cl bond is stiffened in $HeCl_2$. This effect would lead to an increase in the Cl_2 vibrational spacing. Simple calculations based on such a model qualitatively reproduce the trend of an increase in the blue shift with υ'. These increases are superimposed on an initial blue shift at $\upsilon' = 0$ because of a more shallow van der Waals potential surface for the B state electronic distribution. Both mechanisms probably take part in producing the observed blue shift.

Vibrational predissociation lifetimes for $HeCl_2$ follow the trends predicted by the theories of Ewing[15] and Beswick and Jortner. Beswick and Jortner[12] have proposed the expression

$$\Gamma \; \alpha \; \upsilon' \; \exp\left[\frac{-C\omega^{1/2}\mu^{1/2}}{\alpha}\right]$$

to describe the variation of the predissociation lifetime with υ'. In this equation ω is the diatomic vibrational

energy spacing, μ is the van der Waals reduced mass, α is the Morse range parameter, and C is a constant. Figure 4 shows that $\ln(\Gamma/\upsilon')$ is linear with respect to $(\omega\mu)^{1/2}$ within our experimental error.

Comparison of these data to $HeBr_2$ and HeI_2 gives more insight into the dissociation dynamics. The dissociation of HeI_2 is thought to be a nearly pure V-T type process. The existence of other channels to accept energy and hence reduce the V-T energy gap serves to increase the rate. Since no lower frequency vibrational modes exist in the products, the V-V channel is closed. Ewing[15] shows that the V-R channel in HeI_2 is nearly closed because of the large rotational inertia of the I_2 fragment. Dissociation fragments with large moments of inertia can accept only small amounts of energy without inducing a large change in angular momentum. This results in a rapidly angularly oscillating rotational wavefunction that has small coupling matrix elements with the prepared state. This corresponds classically to unreasonably large impact parameters for the dissociation half-collision. Br_2 and Cl_2 have successively larger rotational constants, so the V-R channel should become more available for accepting energy. Comparison of bands for the He complexes with similar energy spacings show evidence of the opening of this channel. The HeI_2 $12 \longleftarrow 0$ band (ω = 107 cm^{-1}), $16 \longleftarrow 0$ $He^{79}Br^{81}Br$ band (ω = 108 cm^{-1}), and

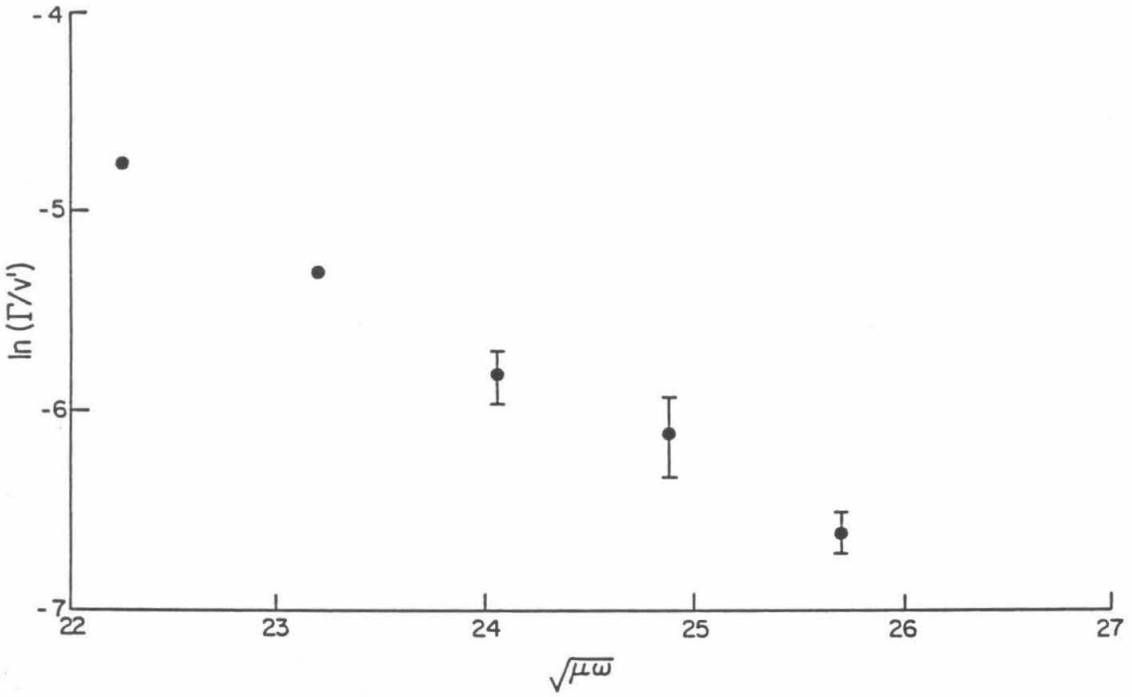

FIG. 4. Plot of $\ln(\Gamma/v')$ vs $(\mu\omega)^{1/2}$ as a test of the energy gap law for the $HeCl_2$ van der Waals molecule. 95 % confidence limits are shown.

the 14←0 $He^{35}Cl_2$ band (ω = 110 cm^{-1}) have lifetimes of 221.2, 53, and 17 ps, respectively. (The $HeCl_2$ lifetime was extrapolated from a linear least-squares fit to the plot in Fig. 4.) He-rare gas van der Waals potentials vary weakly with the atomic number of the rare gas.[18] Approximating the HeX_2 potential as described below, ΔE_{V-T} is probably nearly constant in this series. Thus, the dramatic change in lifetimes cannot be attributed simply to a vibration to translation energy gap problem, and implies that there is some rotational excitation of the lighter diatomic.

The $HeCl_2$ lifetimes are surprisingly close to those measured for $NeCl_2$.[7] The dissociation dynamics are closely related to the shape of the van der Waals B state potential surface. A crude model for the potential surfaces of He- and Ne- Cl_2 may be constructed by using a pairwise atom-atom potential. The Cl-Ne and Cl-He potentials may be estimated by the Ar-Ne and Ar-He scattering data of Lee *et al.*[18,19] The Cl-Cl bond length is fixed at its vibrationally averaged value in the B(υ') state and the rare gas atom is constrained to move along the perpendicular bisector of the Cl_2 bond axis. The well depths of such a potential for $NeCl_2$ and $HeCl_2$ are 100 and 34 cm^{-1}, respectively. As has been discussed previously,[6] this method is likely to overestimate these van der Waals molecule well depths. Integration of the

Schrödinger equation for these one-dimensional potentials gives a zero point energy of 18 and 15 cm^{-1} for Ne- and He-Cl_2. Making the simplification that the dissociation is a pure V-T process, the relative translational energy for the fragments of the prepared state in $\upsilon' = 12$ is 48 cm^{-1} for $NeCl_2$ and 112 cm^{-1} for $HeCl_2$. Based on this simple energy gap argument, one might expect $\upsilon' = 12$ $HeCl_2$ to have a significantly longer lifetime than $\upsilon' = 12$ $NeCl_2$. The energy gap is somewhat compensated for by the lower reduced mass of $HeCl_2$. Also, the model atom-atom potentials lead to a $HeCl_2$ wave function that is significantly more diffuse than that for $NeCl_2$. This effect is illustrated in Fig. 5. Note that the prepared vibrational wave function has nearly the same overlap with the final state plane wave for both $HeCl_2$ and $NeCl_2$.

In conclusion, we report here the observation of the $HeCl_2$ van der Waals molecule using laser induced fluorescence. The spectra can be simulated well by a rigid, asymmetric top model, assuming a triangular structure. Homogeneous linewidths, band shifts, and the van der Waals bond lengths are calculated. Broad homogeneous linewidths indicate rapid vibrational predissociation that is dependent on the vibrational quantum number of Cl_2 in the $HeCl_2$ excited electronic state. Comparison of these results to previous studies of related molecules gives evidence of rotational excitation

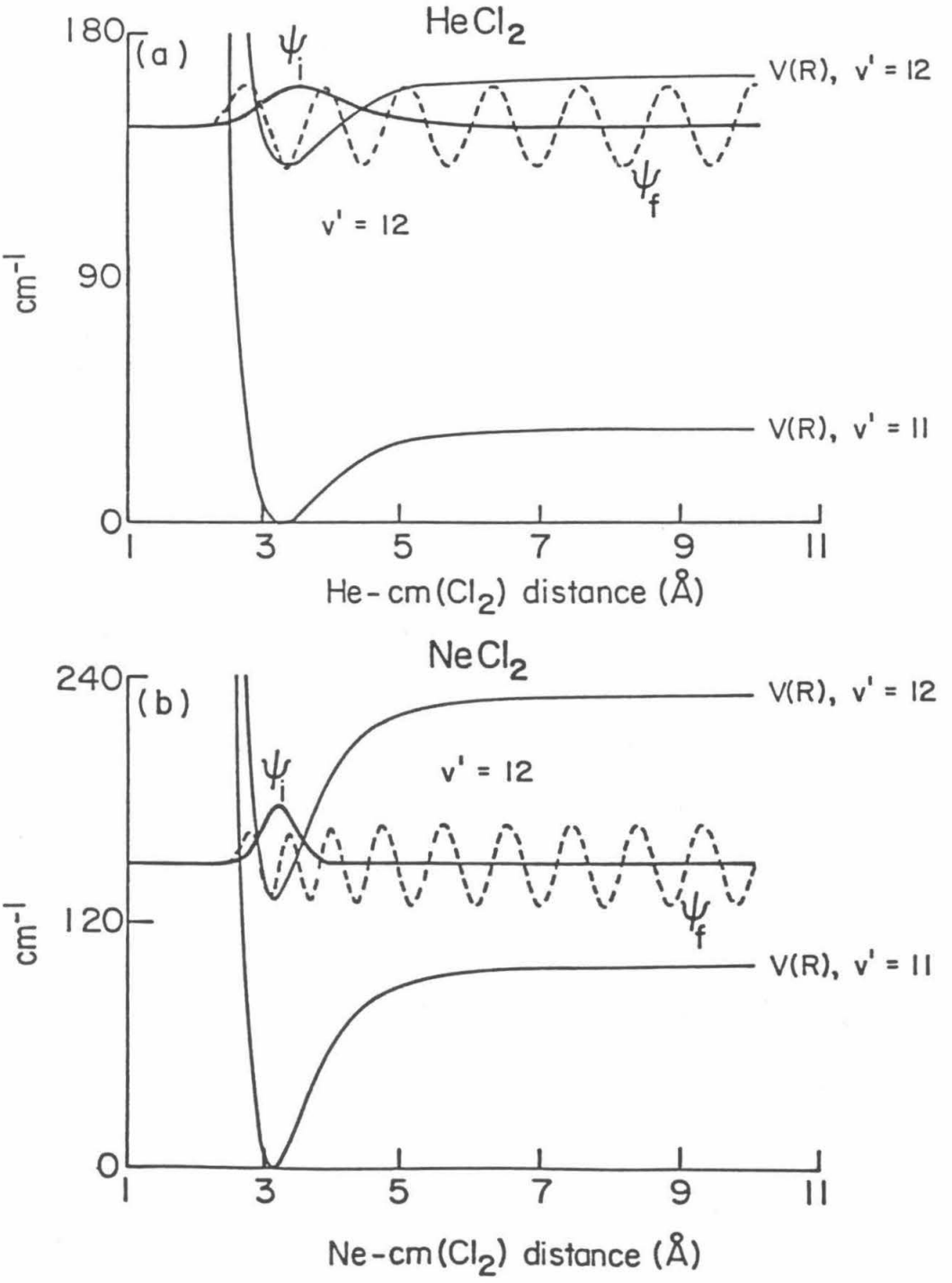

FIG. 5. Momentum gap model for He- and Ne-Cl_2 photodissociation constrained to perpendicular dynamics. ψ_i is the wave function of the spectroscopically prepared state. ψ_f is the final state wave function.

of the Cl_2 dissociation fragment.

V. ACKNOWLEDGEMENTS

This work was supported by the National Science Foundation. Acknowledgement is made to the donors of the Petroleum Research Fund administered by the American Chemical Society and the W.M. Keck Foundation for partial support of this research.

REFERENCES

[1]R.E. Smalley, D.H. Levy, and L.Wharton, J. Chem. Phys. **64**, 3266 (1976).

[2]K.E. Johnson, L. Wharton, and D.H. Levy, J. Chem. Phys. **69**, 2719 (1978).

[3]W. Sharfin, K.E. Johnson, L. Wharton, and D.H. Levy, J. Chem. Phys. **71**,1292 (1979).

[4]J.A. Blazy, B.M. DeKoven, T.D. Russell, and D.H. Levy, J. Chem. Phys. **72**, 2439 (1980).

[5]K.E. Johnson, W. Sharfin, and D.H. Levy, J. Chem. Phys. **74**, 163 (1981).

[6]D.E. Brinza, C.M. Western, D.D. Evard, F. Thommen, B.A. Swartz, and K.C. Janda, J. Phys. Chem. **88**, 2004 (1984).

[7]D.D. Evard, F. Thommen, J.I. Cline, and K.C. Janda, J. Phys. Chem. **91**, 2508 (1987).

[8]B.A. Swartz, D.E. Brinza, C.M. Western, and K.C. Janda, J. Phys. Chem. **88**, 6272 (1984).

[9]F. Thommen, D.D. Evard, and K.C. Janda, J. Chem. Phys. **82**, 5295 (1985).

[10]J.I. Cline, D.D. Evard, B.P. Reid, N. Sivakumar, F. Thommen, and K.C. Janda, in *Structure and Dynamics of Weakly Bound Molecular Complexes*, A. Weber, ed. (D. Reidel Publishing Co., Dordrecht, 1987), p. 533; Chap. 5 of this thesis.

[11]L.J. van de Burgt, J.-P. Nicolai, and M.C. Heaven, J. Chem. Phys. **81**, 5514 (1984).

[12]J.A. Beswick and J. Jortner, J. Chem. Phys. **68**, 2277 (1978).

[13]J.A. Beswick and J. Jortner, J. Chem. Phys. **69**, 512 (1978).

[14]S.B. Woodruff and D.L. Thompson, J. Chem. Phys. **71**, 376 (1979).

[15]G.E. Ewing, Faraday Discuss. Chem. Soc. **73**, 325 (1982).

[16]E. Segev and M. Shapiro, J. Chem. Phys. **78**, 4969 (1983).

[17]J.A. Coxon, J. Mol. Spectrosc. **82**, 264 (1980).

[18]C.H. Chen, P.E. Siska, and Y.T. Lee, J. Chem. Phys. **59**, 601 (1973).

[19]C.Y. Ng, Y.T. Lee, and J.A. Barker, J. Chem. Phys. **61**, 1996 (1974).

Chapter 3

State-to-State Vibrational Predissociation Dynamics and Spectroscopy of He•••Cl_2: Experiment and Theory[†]

[†]Part of this work has been published as a brief report in Phys. Rev. A 36, 1944 (1987).

State-to-State Vibrational Predissociation Dynamics and Spectroscopy of He•••Cl_2: Experiment and Theory

Joseph I. Cline,[a] Brian P. Reid,[b] Dwight D. Evard,[c]
N. Sivakumar, Nadine Halberstadt,[d] and Kenneth C. Janda

Department of Chemistry
University of Pittsburgh
Pittsburgh, PA 15260

ABSTRACT

State-to-state measurements are reported for the vibrational predissociation of $HeCl_2$. Single rovibronic quasibound levels are prepared so that dynamical effects not previously observed in photodissociation experiments are measured. Because of the symmetry of the He•••Cl_2 potential, specific initial rotational levels of the quasibound state decay to either even or odd j fragment rotational levels. The Cl_2 fragment appears predominantly with the loss of one Cl-Cl vibrational quantum and with rotational quantum numbers $j \leq 16$. Fragment rotational distributions show two distinct peaks.

Three-dimensional quantum calculations are performed using an atom-atom potential energy surface, which is adjusted to bring both the calculated spectroscopy and dynamics into good agreement with the experimental data. The bimodal rotational distributions are not consistent with any simple physical picture for the dynamics.

[a] Present address: Joint Institute for Laboratory Astrophysics, National Bureau of Standards and University of Colorado, Boulder, CO 80309-0440.

[b] Present address: Department of Chemistry, Marietta College, Marietta, OH 45750.

[c] Present address: Physikalisch Chemisches Institut der Universität Basel, Klingelbergstrasse 80, CH-4056 Basel, Switzerland.

[d] Present address: Laboratoire de Photophysique Moléculaire, Université de Paris Sud, 91405 Orsay, France.

I. INTRODUCTION

The photo-fragmentation dynamics of small molecules has been the subject of intense experimental and theoretical study. In favorable cases, it is possible to obtain a nearly complete experimental description of the quantum state distribution of the decomposition fragments that results from excitation at a specific energy above the dissociation threshold.[1,2] One difficulty in the analysis of these data has been the inability to construct quantitatively accurate excited state potential energy surfaces. Often, a molecule is excited to a repulsive surface, which involves one or more excited electronic states for which the detailed potential is unknown. In these cases it is difficult to describe precisely the optically prepared state of the system even when the molecules are cooled in a supersonic expansion. However, in the photodissociation of $HeCl_2$, reported in this paper, the initial state can be described in remarkable detail; there is no averaging over the electronic, vibrational, or even rotational quantum numbers of the molecule. True state-to-state dynamics is measured that can be compared directly to quantum mechanical calculations.

The vibrational predissociation of a van der Waals molecule is a process dynamically analogous to the indirect dissociation of a covalently bound molecule on an electronically adiabatic potential energy surface.[3] An

initial state that is quasibound (*i.e.*, long lived enough for vibrational and rotational quantum numbers to be well defined) is produced by optical excitation and decays via coupling among the vibrational modes of the molecule. In this study, for example, energy in excess of the van der Waals binding energy of $HeCl_2$ is optically deposited into the Cl-Cl stretching mode of the complex. The van der Waals molecule undergoes vibrational predissociation when this excess vibrational energy is coupled into low frequency vibrational modes that involve relative motion of the He and the Cl_2 constituents. The process discussed here is quite distinct from many other pump-probe photodissociation experiments that measure the dynamics of the direct dissociation of electronically excited, covalently bound molecules on purely repulsive potential energy surfaces.

van der Waals molecules have characteristics that make them particularly attractive systems for the detailed study of fragmentation dynamics and intramolecular vibrational energy flow.[4] The principal advantage of these systems is the simplicity of the potential energy surfaces involved. The dynamics occurs on a single, often very well-defined electronic potential surface of the covalently bonded fragments. It is relatively easy to construct a realistic overall potential that accounts for weak van der Waals forces between the constituents of the

complex. Theoretical treatment of this problem leads naturally to a zero-order decoupling of the van der Waals motions from the vibration of covalent bonds in a manner analogous to the Born-Oppenheimer separation of nuclear and electronic motion. Zero-order vibrational states are formed as products of wave functions that describe the vibration of covalent bonds and vibrational wavefunctions for the van der Waals stretches and bends. The dynamics is then described by evaluating higher-order couplings among these zero-order states. Theoretical models have been developed that can quantitatively reproduce detailed experimental results. Still, there are few systems for which potential energy surfaces have been constructed that have been rigorously tested experimentally.

The rare gas-halogen[5-17] and interhalogen[18-21] van der Waals molecules have been intensively studied because they appear to provide the best hope for a complete description of state-to-state dynamics by both experiment and theory. Fragmentation rates and in some cases fragment state distributions are known for these systems (with the notable exception of ClF). Despite the relative simplicity of these molecules, they provide examples of a variety of fundamentally important dynamical phemomena such as inelastic half-collisions, intramolecular vibrational energy redistribution, rotational rainbows, and quantum interferences. A second important aspect of

this research is aimed at using the rotational structure of the vibronic transitions to aid the complete determination of the potential energy surface. In the past the spectroscopy has been analyzed in terms of simple rigid-top models to give effective molecular geometries. In these highly non-rigid molecules, this simple treatment of the molecular geometry is surprisingly effective. Precise agreement with measured spectra, however, can be obtained only by considering the true potential energy surface for the molecule; deviations from rigidity are measurable even at the relatively low rotational resolution of these experiments.

In a recent brief report,[5] we presented laser pump-probe experiments on $HeCl_2$, which represent the most completely state-resolved work yet performed for this class of molecules. $HeCl_2$ is a particularly favorable candidate for state-resolved experiments for the following reasons. First, the molecule has a relatively uncongested excitation spectrum (large, rotational constants and a sufficiently long lifetime, thus small homogeneous broadening), so that it is possible to optically prepare individual quasibound states with precisely known rotational and vibrational quantum numbers. Second, the potential energy surface between He and Cl_2 is almost certainly determined by simple van der Waals forces. Third, because the relatively light He can impart limited

angular momentum to the Cl_2, the number of final channels is easily incorporated into a calculation. Fourth, the final momentum of the products results in a He wavelength commensurate with molecular dimensions so that quantum effects are enhanced. Finally, the spectroscopy of Cl_2 is well known so that the quantum state of the Cl_2 fragment can be measured following decay of the prepared quasibound state.

This paper presents a rather complete experimental and theoretical description of the decomposition dynamics of $HeCl_2$. The energies of the bound and quasibound levels of this molecule are extracted from resolved structure in the excitation spectrum and the dynamics of several different levels is measured by the pump-probe technique. These results are used in combination with data from other sources to construct a potential energy surface for $HeCl_2$. Three-dimensional quantum mechanical calculations are presented for this surface, which are in agreement with both the spectroscopic and dynamical experimental results. $HeCl_2$ can thus be regarded as a "solved" model system in the study of molecular fragmentation dynamics. It is demonstrated how the dynamics depends on the initially prepared state of the molecule, on the coupling among the vibrational modes of the molecule, and upon the the interactions between the recoiling fragments. The truly state-to-state character of these data permits the

measurement of effects typically observed only in scattering experiments, in particular, dynamical symmetry constraints and possibly interference phenomena.

II. EXPERIMENTAL DESCRIPTION

A. Pump-Probe Scheme

The scheme for preparing the vibronically excited, quasibound $HeCl_2$ and probing the Cl_2 fragment is shown schematically in Figure 1. The pump laser frequency, ω_1, is tuned to prepare a vibronically excited, quasibound state of $HeCl_2$ with υ quanta of vibration in the Cl-Cl stretching mode and no initial excitation of the van der Waals vibrational modes. This electronic state of $HeCl_2$ correlates to the long-lived Cl_2 $B^3\Pi(0_u^+)$ state.[22] (The radiative lifetime of $Cl_2(B,\upsilon' \lesssim 12)$ is ~305 μs.[23]) Vibrational bands of the $HeCl_2$ B⟵X transition have been previously identified in a laser-excited fluorescence study[6] as features shifted 3-4 cm^{-1} to the blue of each Cl_2 $B^3\Pi(0_u^+) \longleftarrow X^1\Sigma_g^+$ ($\upsilon' \longleftarrow 0$) band origin.[22] By scanning the laser through the rotational structure of these bands, specific rotational levels of $HeCl_2(B,\upsilon')$ are prepared. The He•••Cl_2 bond is so weak that one quantum of the Cl-Cl vibrational stretch has sufficient energy to cause decomposition. Intramolecular vibrational energy redistribution results in decay of the prepared state with a lifetime, τ, which depends upon the initially prepared

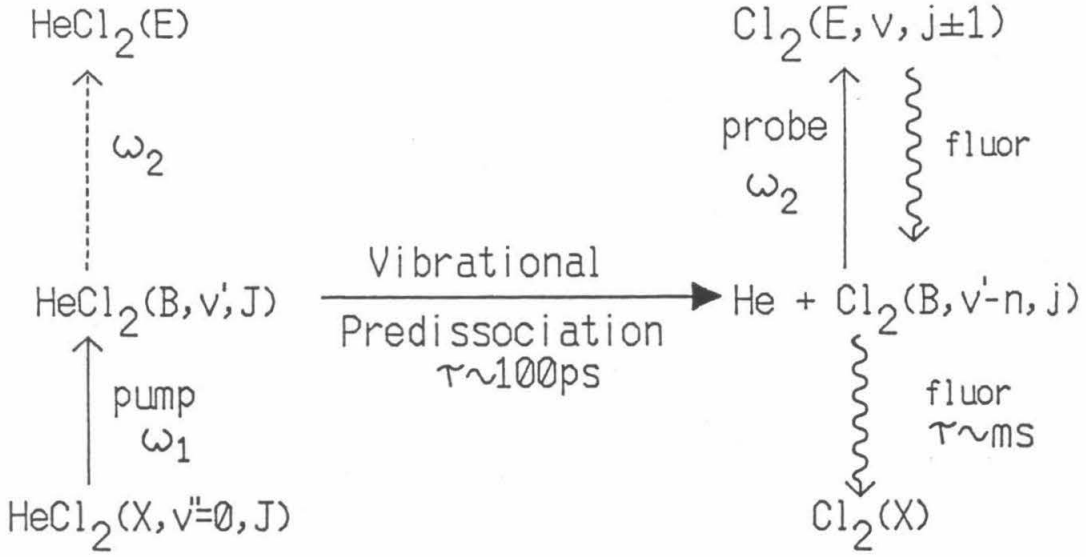

FIG. 1. Laser pump-probe scheme for preparation of quasibound levels of $HeCl_2(B,v',J)$ and measurement of the vibrational and rotational state distributions of the $Cl_2(B,v,j)$ fragment.

vibrational state ($\tau \sim 10^0$-10^3 ps). The quantum state of the $Cl_2(B)$ fragment is determined by tuning ω_2 through the Cl_2 $E(0_g^+) \leftarrow B^3\Pi(0_u^+)$ transition.[24] For both excitation spectra and product distribution measurements, undispersed fluorescence from the Cl_2 E state is detected as a function of ω_1 and ω_2.

B. Apparatus

A schematic diagram of the experimental apparatus is shown in Fig. 2. The vacuum apparatus has been previously described.[8] $HeCl_2$ was prepared in a pulsed, free jet expansion (150 μm diameter nozzle) of a mixture of 0.6% Cl_2 in He at a total pressure of 350 psi. The mixture was obtained by passing He over a vessel containing liquid Cl_2 at -77°C. The rotational temperature of van der Waals molecules formed in the jet was approximately 0.6 K.

Two dye lasers, pumped by an XeCl excimer laser, provided tunable pump (ω_1) and probe (ω_2) laser pulses, which traveled colinearly through the vacuum apparatus, perpendicular to the free jet expansion. The dye laser providing the ω_1 pulse was operated with an angle-tuned, intracavity etalon to produce ~20 ns pulses with a 0.05 cm^{-1} band width. The output of the probe dye laser was frequency-doubled to produce ~20 ns pulses with a ~0.2 cm^{-1} bandwidth, and a cutoff filter was used to attenuate the fundamental. The ω_2 pulse was delayed ~10 ns from the ω_1 pulse. Laser power was maintained such

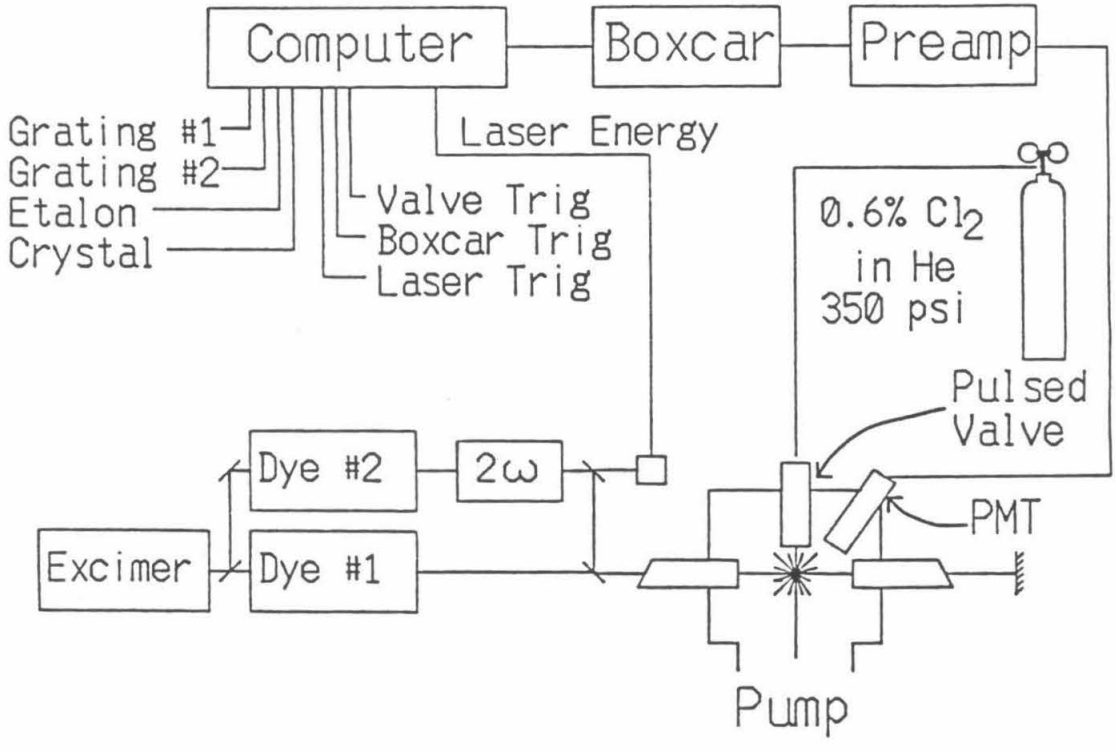

FIG. 2. Schematic diagram of experimental apparatus. Two dye lasers are pumped by a XeCl excimer laser. Dye laser #2 receives 60 % of the excimer pulse energy; dye laser #1 receives the remaining 40 %. The probe beam (ω_2) is generated as the second harmonic of dye #2, while the pump beam (ω_1) is the fundamental of dye #1. The pump and probe beams are combined by a dichroic optic and travel collinearly through light baffles to intersect the pulsed jet. Fluorescence is collected by a lens (not shown) and imaged through defining slits onto a photomultiplier. See text for more details.

that the experimental signals scaled linearly with pulse energies.

UV fluorescence was imaged onto a UV sensitive photomultiplier, and a UV pass filter was used to reject visible laser scatter. The ω_2 pulse energy was monitored by reflecting a portion of the UV beam into a dye cell where fluorescence was detected by a photodiode. Gated integrators averaged the photodiode and photomultiplier signals. A microcomputer controlled the synchronization of the pulsed valve, laser trigger, and detection electronics, scanned the dye laser gratings, etalon, and doubling crystal, and recorded the data.

III. EXPERIMENTAL RESULTS

A. Excitation spectra: dynamical selection rule

In a previous paper[6] we studied the $He^{35}Cl_2$ molecule by laser-induced fluorescence (LIF). In that experiment, visible fluorescence from the $^{35}Cl_2(B)$ dissociation fragment was recorded as the ω_1 frequency was tuned through the $He^{35}Cl_2$ absorption; no probe laser was used (see Fig. 1). Although individual lines in the $He^{35}Cl_2$ excitation spectrum could not be completely resolved in the simple LIF experiment, the band contours displayed distinct rotational structure, which was modeled assuming a rigid, T-shaped geometry for the molecule, as shown in Fig. 3. The rotational structure of the vibronic bands

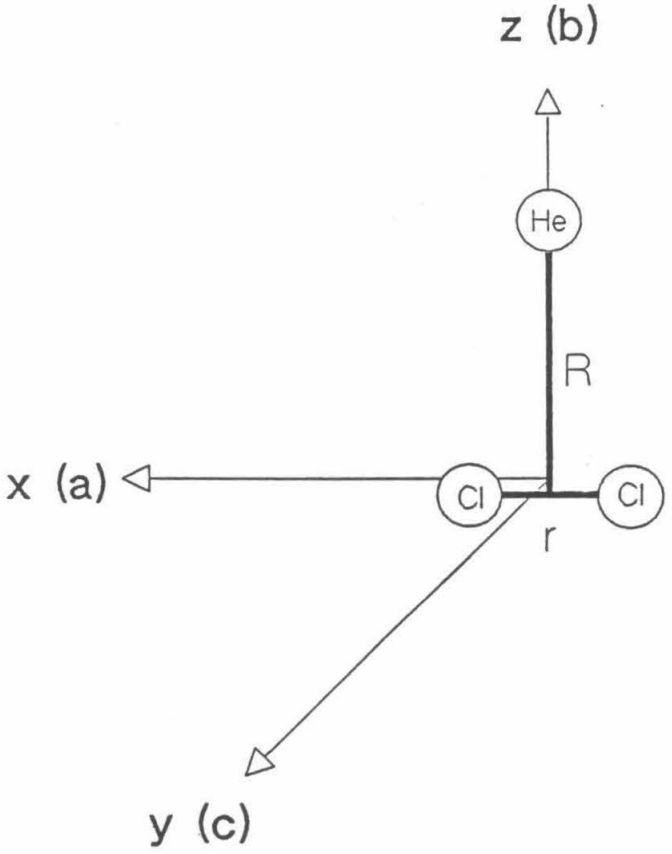

FIG. 3. Rigid, T-shaped model for $HeCl_2$. *R* and *r* are vibrationally averaged bond lengths. a, b, and c indicate the inertial axes for the asymmetric top analysis of the $HeCl_2$ excitation spectra.

was best fit using a He to Cl_2 center-of-mass distance of R_X = 3.8±0.4 Å in the ground (X) electronic state, and when the difference in R between the ground and excited electronic states, R_B-R_X, was 0.127±0.024 Å. The spectra exhibited measurable homogeneous broadening that was a function of the number of vibrational quanta deposited in the Cl-Cl stretch. There was no evidence of any progressions in the excited van der Waals vibrational modes: all B⟵X transitions occur between ground van der Waals vibrational levels.

The pump-probe technique utilized in the present work offers significant advantages over the LIF method of recording excitation spectra. The signal-to-noise ratio is significantly improved. In a one laser LIF experiment, the exceedingly long lifetime of the B electronic state of Cl_2 severely limits signal collection efficiency because most of the Cl_2(B) fragments in the jet fluoresce after they have moved out of the detection region. This problem is eliminated in the present experiment because the E⟵B transition used in the pump-probe detection scheme is fully allowed. Efficient collection of the prompt E state fluorescence outweighs the fact that two photons must be absorbed to reach the E state. However, the principal advantage of the present technique is the ability to measure how the excitation spectrum of $HeCl_2$ depends on what fragment state is being monitored by the ω_2 pulse.

Typical pump-probe excitation spectra are shown in Fig. 4. In Fig. 4a the probe frequency, ω_2, is positioned on the bandhead of the $^{35}Cl_2$ E⟵B 0⟵7 band and the pump frequency, ω_1, is tuned across the $He^{35}Cl_2$ B⟵X 8⟵0 band. The bandhead region of the probe transition contains a superposition of the R(0)-R(10) rotational lines. Since in this case no particular fragment state is selected by the probe laser, the spectrum is similar to the excitation spectra observed in the LIF experiments of Ref. 6. Fig. 4b shows the excitation spectrum obtained by again tuning ω_1, but in this case ω_2 is positioned on the P(10) line of the $^{35}Cl_2$ E⟵B 0⟵7 transition so that only transitions to $He^{35}Cl_2(B,\upsilon'=8)$ levels that decay to give the fragment $^{35}Cl_2(B,\upsilon=7,j=10)$ state are observed. The excitation spectrum obtained when the probe laser is positioned on the P(9) line is shown in Fig. 4c. The spectra of Figs. 4b and 4c result from two different sets of transitions, which, when added together, account for all the transitions observed in Fig. 4a. This separation, which we first reported in Ref. 5, is the result of a symmetry selection rule in the fragmentation dynamics due to the symmetry of the $He-Cl_2$ van der Waals potential.

By applying a rigid, asymmetric top analysis to these spectra, the critical symmetry becomes evident. This symmetry, parity, is given by the behavior of the initial $HeCl_2$ asymmetric top rotational wavefunction and

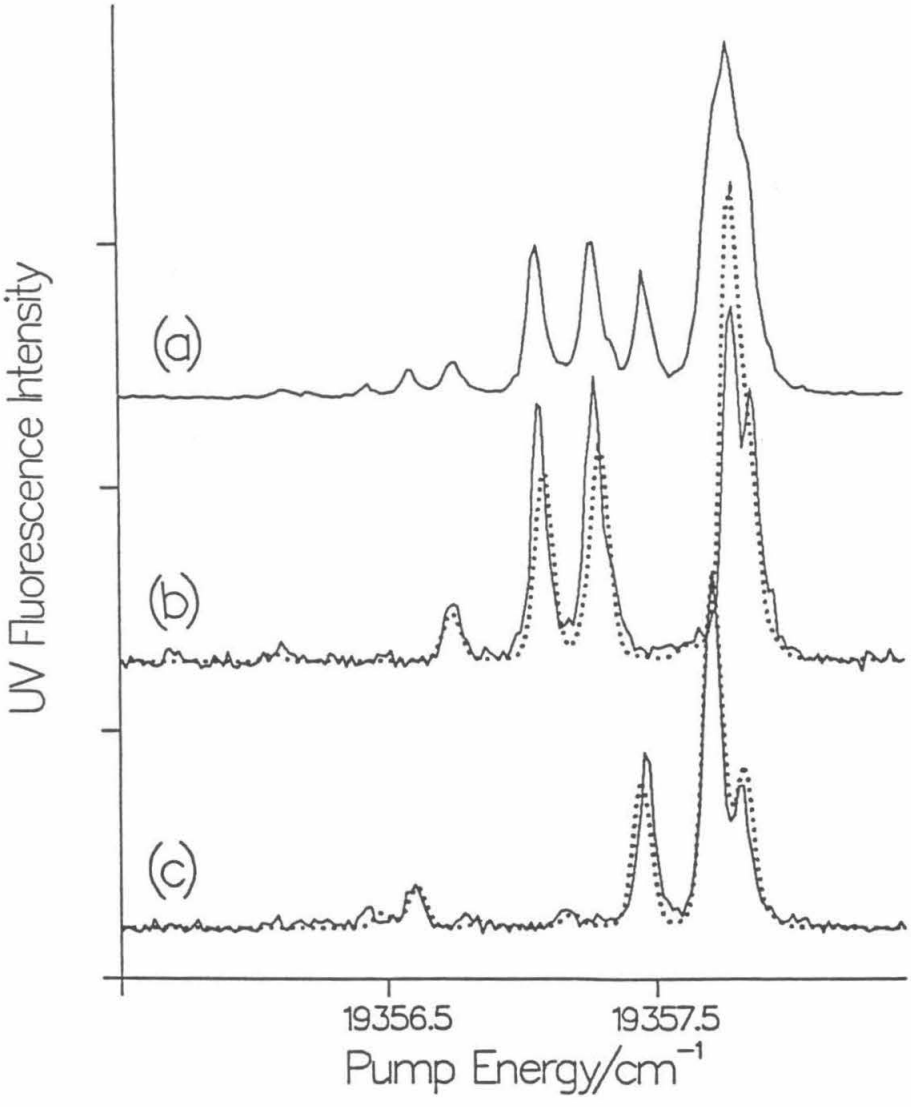

FIG. 4. Solid curves are spectra of $He^{35}Cl_2$ obtained by scanning ω_1 through the $He^{35}Cl_2$ B←X (8←0) band and (a) positioning ω_2 on the bandhead of the $^{35}Cl_2$ E←B (0←7) transition, (b) positioning ω_2 on the P(10) line of the $^{35}Cl_2$ E←B (0←7) band, and (c) positioning ω_2 on the P(9) line. Dotted curves are calculated asymmetric top spectra for transitions to only (b) even- or (c) odd-parity rotational states of $He^{35}Cl_2(B,\upsilon'=8)$. The rigid, T-shaped model has He to Cl_2 center-of-mass distances of 3.67 and 3.79 Å and Cl-Cl distances of 1.99 and 2.64 Å in the X and B electronic states, respectively. The linewidth is set to that of Ref. 6 and the Boltzmann rotational temperature is 0.6 K.

the final Cl_2 fragment rotational wavefunction upon exchange of the Cl atoms. First, consider the initial $HeCl_2$ asymmetric top wavefunction (prepared by the ω_1 pulse). The asymmetric top rotational states, $J_{k_a k_c}$, of $HeCl_2$ can be assigned as having either even or odd parity, depending upon whether they are symmetric or antisymmetric upon operation of the C_2^b operator that exchanges the Cl atoms[25,26] as seen in Fig. 3. The parity of the $Cl_2(B)$ fragment rotational wavefunction is given simply by whether j is even or odd. The observed selection rule is that initially prepared rotational states of one parity decay only to fragment rotational states of the same parity.

The transition dipole for the $HeCl_2$ B⟵X transition lies parallel to the a inertial axis (see Fig. 3), so that "a-type" asymmetric top rotational transitions[27] are expected in the excitation spectrum. The calculated spectra in Fig. 4 are for asymmetric top rotational transitions to either even- (Fig. 4b) or odd- (Fig. 4c) parity levels of $He^{35}Cl_2$ (B,υ=8). He to Cl_2 center-of-mass distances, R_X and R_B, similar to those of Ref. 6 were used. Considering the fact that $HeCl_2$ is a very non-rigid molecule, the agreement with the observed line positions is remarkable.

For practical reasons most of the experiments reported in this paper were performed using the $He^{35}Cl_2$

isotopic species. The homonuclear $He^{35}Cl_2$ species has a higher natural abundance than the heteronuclear species, and the spectroscopy of $^{35}Cl_2$ is known in much more detail than that of $^{35}Cl^{37}Cl$. However, it should be noted that, for the homonuclear species, nuclear exchange symmetry plays a potentially important role. The ^{35}Cl nucleus is a fermion ($I_{nuclear}$ = 3/2) and $^{35}Cl^{35}Cl$ exists in *ortho*- and *para*-forms. The nuclear spin state of the $^{35}Cl_2$ component of $He^{35}Cl_2$ would be expected to be conserved throughout the decomposition. However, as shown in Fig. 5, parity is also conserved in the decomposition of $He^{35}Cl^{37}Cl$ in which nuclear exchange symmetry cannot affect the dynamics. The observed parity selection rule not only conserves nuclear spin; rather, it results from the symmetry of the van der Waals potential (or near symmetry in the case of $He^{35}Cl^{37}Cl$) with respect to interchange of Cl atoms.

Quantitative fits to these "parity-selected" excitation spectra of the type in Fig. 4 were generated using the rigid, asymmetric top model described above. The line positions and line strengths for rovibronic transitions to $HeCl_2(B,v')$ asymmetric top rotational states of a particular parity were calculated. Each line was then convoluted with a Voigt profile[28] which includes a homogeneous linewidth due to the decay rate of the prepared state and an inhomogeneous linewidth that takes into account the laser and doppler linewidths. Typical

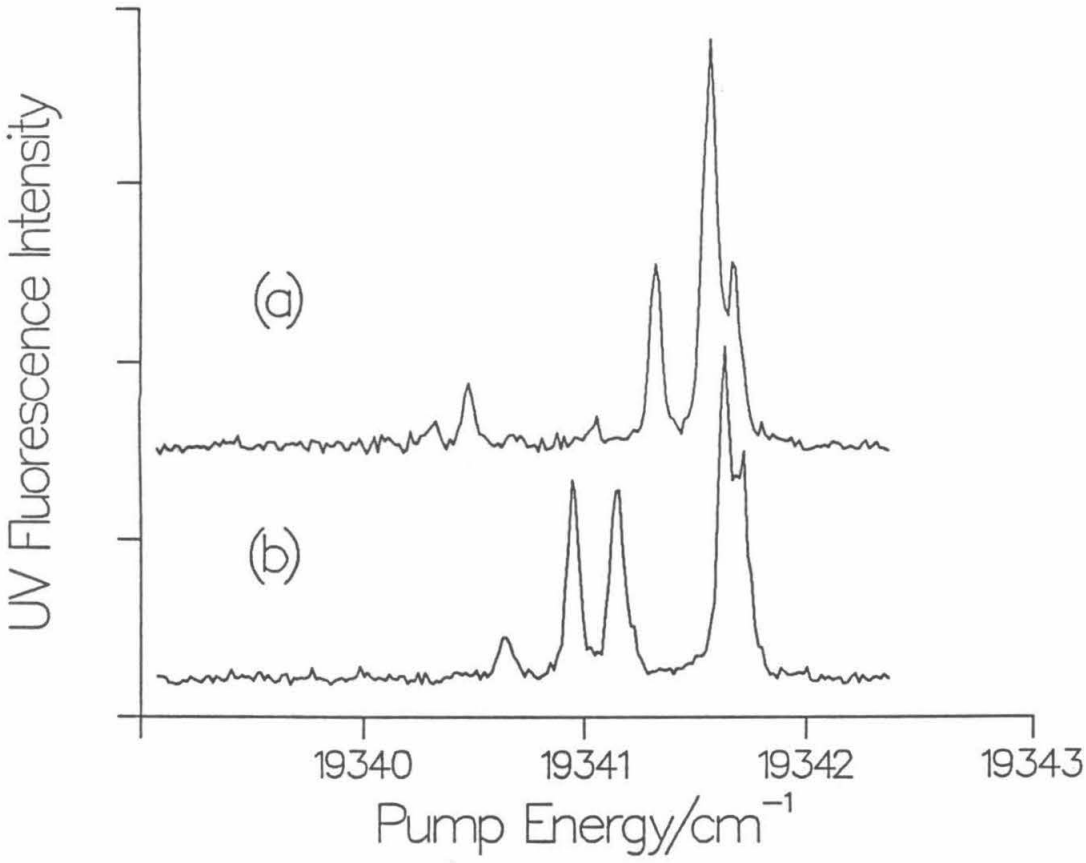

FIG. 5. Parity-selected excitation spectra of the $He^{35}Cl^{37}Cl$ B←X (8←0) band exactly analogous to that shown in Fig. 4 for the $He^{35}Cl_2$ isotopic species. Spectrum (a) shows transitions to odd parity levels; (b) shows transitions to even parity levels. Note that there is no measurable breakdown of the parity selection rule.

linewidths of the Gaussian inhomogeneous profiles were 0.07 cm^{-1} (FWHM) from the measurement of uncomplexed Cl_2 B←X transitions. In fits to the rigid, asymmetric top model the frequency of the band origin, the He to Cl_2 center-of-mass distances R_X and R_B, the rotational temperature, and the homogeneous linewidths were optimized by a least-squares method. The inhomogeneous linewidth was fixed to the value measured as described above. Cl-Cl distances were assumed to be unperturbed by the presence of the He atom and were set to their average values for the particular vibrational state.[22] The bond lengths extracted from the fits of the present "parity-selected" spectra of the $HeCl_2$ 6←0 and 8←0 bands agree within experimental error with those previously determined by the asymmetric top analysis of the total fluorescence spectra of Ref. 6. The rigid, asymmetric top model of $HeCl_2$ cannot perfectly simulate the excitation spectra; the fits to the spectra of Fig. 4 show experimentally significant deviations. A more sophisticated treatment of the spectroscopy of $HeCl_2$ will be presented in Sec. IV(C).

B. Homogeneous Broadening of High Vibrational Bands

There is no detectable homogeneous broadening of the $He^{35}Cl_2$ (B,υ=6) level within our experimental resolution, but higher υ' bands do show measurable homogeneous broadening. This effect is illustrated in Fig. 6.

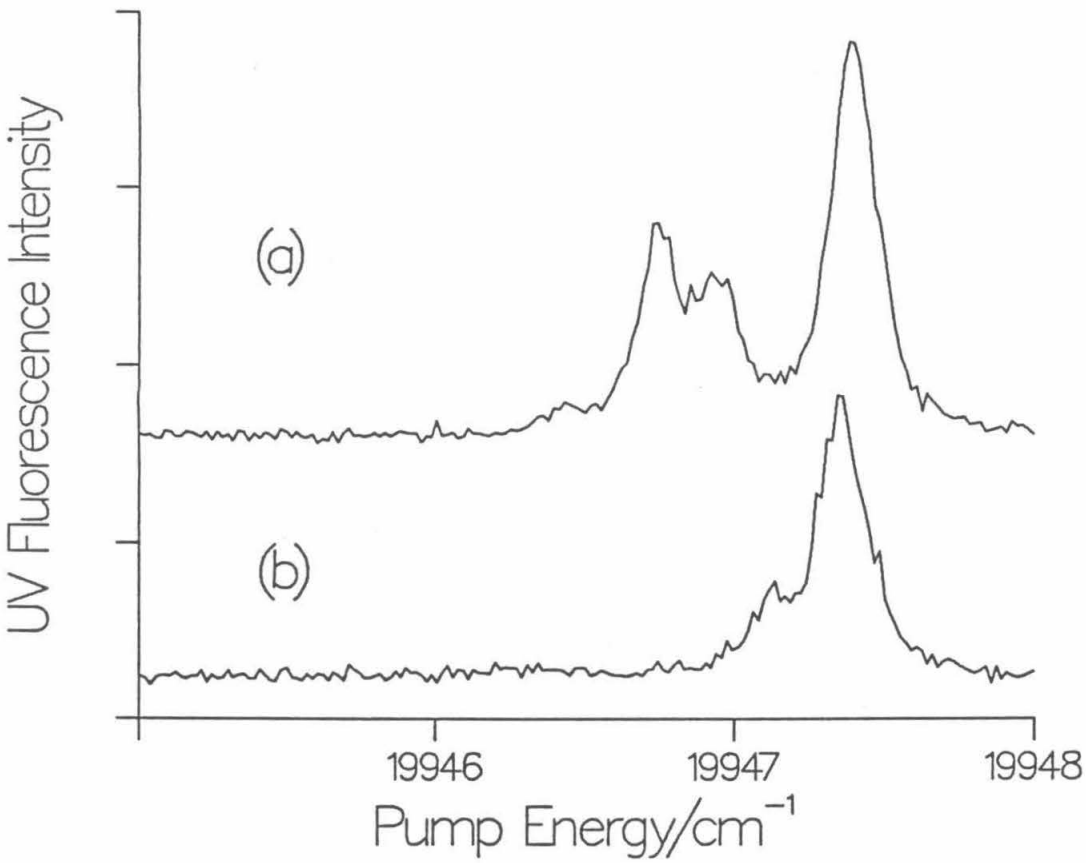

FIG. 6. Homogeneously broadened parity-selected excitation spectra of the $He^{35}Cl_2$ B←X (12←0) band. Spectrum (a) shows transitions to even parity levels; (b) shows transitions to odd parity levels.

Homogeneous linewidths for the bands with $8 \leq \upsilon' \leq 12$ were reported in the previous LIF study.[6] The homogeneous linewidths (FWHM) of the $\upsilon' = 20$ and 24 levels were measured in this study to be 1.0 and 2.0 cm^{-1}, respectively, corresponding to lifetimes of 5.4 and 2.5 ps.

Interpretation of the homogeneous widths of the $\upsilon' = 20$ and 24 bands of $HeCl_2$ is complicated by the possibility of electronic predissociation. $^{35}Cl_2(B)$ $\upsilon' = 12$, $j' > 21$ and all $\upsilon' > 12$ levels undergo electronic predissociation to ground-state Cl $^2P_{3/2}$ atoms and the average lifetime of the $13 \leq \upsilon' \leq 25$ levels is 671 ns[29,30] (compared to ~305 μs for $\upsilon' \leq 12$[23]). Although the electronic predissociation of free $Cl_2(B,\upsilon'>13)$ is still much slower that the vibrational predissociaton rate of $HeCl_2$, evidence is presented in Sec. III(D) that suggests that very high vibrational levels of $HeCl_2$ may undergo electronic predissociation with a rate comparable to the rate of vibrational predissociation. It is then no longer possible to identify our experimental lifetime as a purely vibrational predissocition lifetime. The lifetimes of the $\upsilon' = 20$ and 24 levels of $HeCl_2$ are *longer* than what would have been expected based on an extrapolation of the energy gap analysis of Ref. 6 applied to the $\upsilon' \leq 12$ levels; it is clear that more work is required to understand the decomposition dynamics of the high υ' levels of $HeCl_2(B)$.

C. Fragment vibrational and rotational population distributions

Having considered the spectroscopy of the B←X transitions of $HeCl_2$, it is clear how to prepare individual rotational levels of the $HeCl_2$ B state when there is little homogeneous broadening. For the lowest vibrational levels ($\upsilon' \leq 8$) of $HeCl_2$(B) the pump laser can be positioned on an isolated rotational line within a vibrational band to prepare a specific rotational-vibrational level. The probe laser can then be used to measure the rotational and vibrational populations of the Cl_2 fragment resulting from the decomposition of this specific state.

An example of such an experiment is presented in Fig. 7, which shows probe laser spectra of the $^{35}Cl_2$ (B,υ=5) fragment resulting from decomposition of different rotational levels of $He^{35}Cl_2$ (B,υ=6). The spectrum in Fig. 7a was obtained by positioning ω_1 on the $He^{35}Cl_2$ B←X, 6←0, 0_{00}←1_{01} transition and tuning ω_2 through the $^{35}Cl_2$ E←B, 0←5 transition. The spectrum of Fig. 7b was obtained when ω_1 was positioned on the $He^{35}Cl_2$ B←X, 6←0, 1_{10}←1_{11} transition. The $^{35}Cl_2$ E←B, 0←5 spectra appear as simple $^1\Sigma$-$^1\Sigma$ type rigid rotor spectra consisting of an R-branch head and a well-resolved P-branch, which extends to the red of the bandhead. There are two unique aspects of the spectra in Fig. 7. First, because of the symmetry

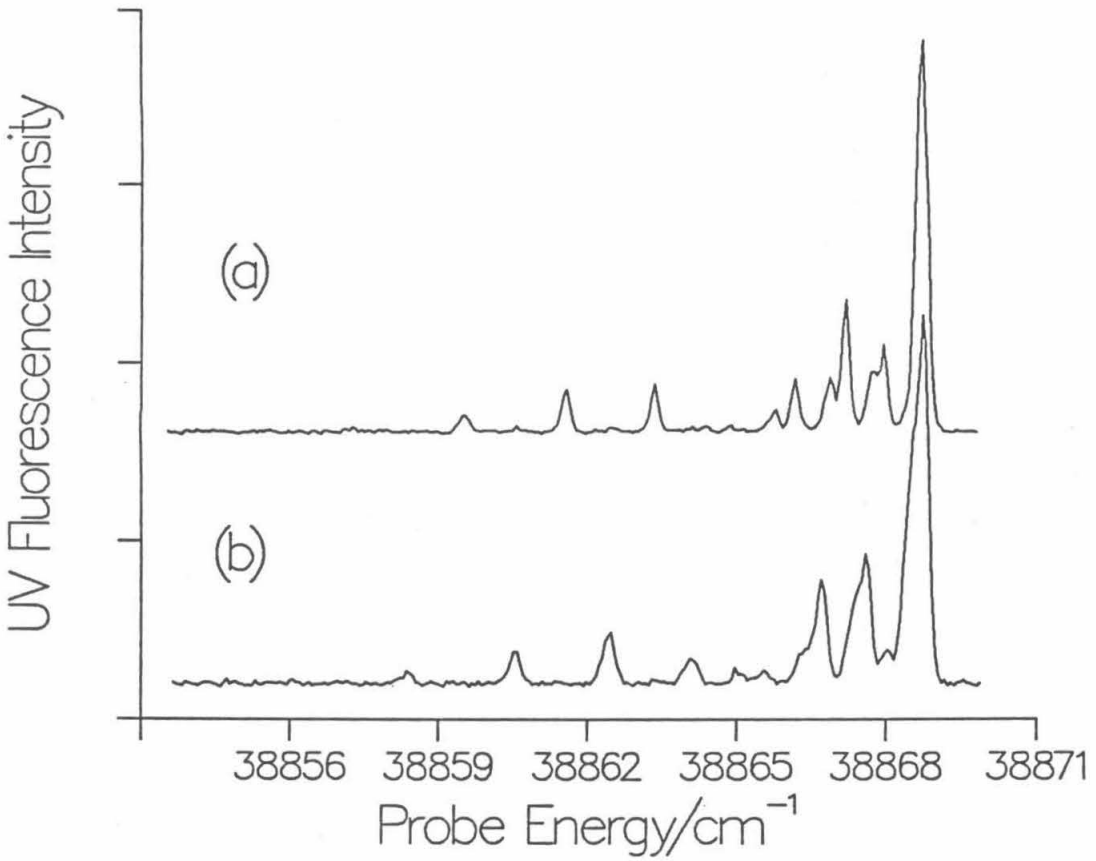

FIG. 7. Pump-probe spectra obtained by scanning ω_2 through the fragment $^{35}Cl_2$ E←B (0←5) band and (a) positioning ω_1 on the $He^{35}Cl_2$ B←X (6←0, 1_{10}←1_{11}) transition and (b) positioning ω_1 on the B←X (6←0, 0_{00}←1_{01}) transition. These spectra reveal the rotational state distribution of the (a) 1_{10} and (b) 0_{00} rotational levels of $He^{35}Cl_2(B,\upsilon'=6)$.

selection rule discussed in Sec. III(A), the even-parity $He^{35}Cl_2$ $(B, \upsilon'=6, J_{k_a k_c}=0_{00})$ state decays only to even j rotational states of the $^{35}Cl_2$ product. The odd parity 1_{10} initial rotational level decays to only odd j fragment states. The other unusual feature of the fragment Cl_2 spectra is the distinctly bimodal intensity distribution in the P-branch rotational lines, which are resolved in this spectrum. The intensity distribution has local maxima at $j = 2$ to 3 and 9 to 10 and decays to unobservable levels for $j > 14$. There is no measurable population of fragment $^{35}Cl_2$ vibrational levels other than $\upsilon = 5$; the only observed channel for vibrational predissociation of $HeCl_2$ $(B, \upsilon'=6)$ is the transfer of one Cl_2 vibrational quantum to the van der Waals modes.

Fragment rotational state populations were extracted from the line intensities in the Cl_2 E⟵B spectra by fitting the intensity, $I(\omega)$, of the observed spectra to an equation of the form

$$I(\omega) = \sum_j \Big[I_{j-1,j}\, L[\omega-\omega_P(j),\Gamma] + I_{j+1,j}\, L[\omega-\omega_R(j),\Gamma] \Big] + C \,, \qquad (1)$$

where the summation is over all observed fragment rotational quantum states, j, and C is the background level. A Gaussian instrumental lineshape function, L, was

used with a linewidth, Γ, of typically 0.2-0.3 cm^{-1}(FWHM). The frequencies of individual R- and P-branch lines, $\omega_R(j)$ and $\omega_P(j)$, were calculated using the band origins and spectroscopic constants of Refs. 22 and 24. The relative line intensities are given by[31]

$$I_{j',j} = N(j)\ S_{j',j}/(2j+1)\ , \qquad (2)$$

where the $S_{j',j}$ are the Hönl-London factors,[32] and $N(j)$ is the relative population of the fragment state that appears with rotational quantum number j. The frequency dependence of the Einstein coefficients over the small spectral range spanned by the band is negligible. The parameters optimized in the fits were Γ, C, and the $N(j)$. In general, one of the two rotational branches of the fragment Cl_2 E⟵B bands is extended so that the intensities of individual, completely resolved rotational lines can be measured, while the other branch forms a bandhead. (Because of the change in the rotational constant with υ', the P-branch is extended for the lower υ' bands, the R-branch for the higher υ' bands.) However, in most cases a few of the lowest j rotational lines of the extended branch fall within the congestion of the bandhead of the other branch so that care needs to be taken in obtaining the correct populations of the lowest two or three rotational levels. The $N(j)$ were obtained by

fitting, one at a time, the intensities of the lines in the extended branch, beginning with the highest j line and working successively towards the lowest j line. Once $N(j)$ is known, the intensities of lines in the other branch are fixed by Eq. (2). Thus, when fitting the lowest j lines of the extended branch that are not completely resolved, their populations can still be extracted since the intensities of lines in the bandhead are accounted for. Excellent fits were obtained by this method to the Cl_2 fragment spectra.

Cl_2 (B) fragment rotational state population distributions were extracted from the fragment spectra for the $\upsilon' = 6$, 8, 12, 20, and 24 bands of the $He^{35}Cl_2$ B$\leftarrow$X, $\upsilon'\leftarrow 0$ transition. In all cases the dominant vibrational predissociation product vibrational channel is the one in which one quantum of the Cl-Cl stretch is transferred to decompose the molecule (termed the "$\Delta\upsilon = -1$ channel").

Tables 1 and 2 tabulate the fragment $^{35}Cl_2$ (B,υ'-1) rotational state population distributions of the $J = 0$ and 1 rotational levels of $He^{35}Cl_2$ (B,υ'=6,8,12). For decomposition of the υ'=6 and 8 states, the $\Delta\upsilon = -1$ channel accounts for all of the observable product vibrational state population, the fragment rotational population decays to unobservable levels for $j > 15$, the rotational distributions are bimodal with a distinct minimum at $j = 6$ and 7, and parity is strictly conserved

Table 1:
Rotational quantum state fractional population distributions, $P(j)$, of $^{35}Cl_2$ (B,υ'=7) following dissociation of the J=0 and 1 levels of $He^{35}Cl_2$ (B,υ'=8)

	Prepared $He^{35}Cl_2$ (B,υ'=8) rotational state, $J'_{k'_a k'_c}$			
	0_{00}	1_{01}	1_{11}	1_{10}
j=0	0.17		0.15	
1		0.32		0.31
2	0.35		0.34	
3		0.34		0.34
4	0.20		0.21	
5		0.11		0.11
6	0.02		0.03	
7		0.03		0.00
8	0.07		0.07	
9		0.08		0.11
10	0.11		0.11	
11		0.09		0.08
12	0.06		0.06	
13		0.03		0.04
14	0.02		0.02	
$\langle E_{rot} \rangle / cm^{-1}$	5.3	4.8	5.5	5.1

E_{avail} =165.3 cm^{-1}

$E_{rot}(j_{max}= 14)$ = 29.7 cm^{-1}

Table 2:
Rotational quantum state fractional population distributions, $N(j)$, of $^{35}Cl_2$ (B,v'-1) following dissociation of $He^{35}Cl_2$ (B,v',$J'_{k'_a k'_c}$)

	Prepared $He^{35}Cl_2$ (B) state: v', $J'_{k'_a k'_c}$		
	$6,0_{00}$	$6,1_{10}$	$12,0_{00}$
j=0	0.19		0.23
1		0.26	
2	0.31		0.32
3		0.33	
4	0.22		0.18
5		0.12	
6	0.02		0.04
7		0.01	
8	0.06		0.08
9		0.11	
10	0.11		0.09
11		0.10	
12	0.06		0.05
13		0.04	
14	0.02		0.01
15		0.01	
$\langle E_{rot} \rangle / cm^{-1}$	5.5	6.3	4.1
E_{avail} / cm^{-1}	186.7	187.1	121.8
$E(j_{max}) / cm^{-1}$	31.1	35.5	26.5

in the decomposition dynamics. The distributions for decomposition of the $J = 0$ and 1 levels of the $\upsilon' = 6,7$ states are identical to each other within the experimental error.

The vibrational predissociation of $HeCl_2$ is primarily a V⟶T type process. The energy available for fragment rotational and translational kinetic energy, E_{avail}, is given by the energy of the Cl-Cl vibrational quantum, E_υ, less the B state dissociation energy of the complex, D_0. For example, the decomposition of the $He^{35}Cl_2(B,\upsilon'=8,J_{k_a k_c}=0_{00})$ releases $E_{avail} = 165.3\ cm^{-1}$. The average energy in rotation of the $^{35}Cl_2(B,\upsilon=7)$ fragment is $\langle E_{rot}\rangle = 5.3\ cm^{-1}$, which is only 3 % of E_{avail} [the value of $D_0(B)$ is calculated in Sec. IV(B)]. The highest measurable fragment rotational level, $j_{max} = 14$, accounts for only 18 % of the available energy.

For the higher vibrational levels ($\upsilon' > 8$) of the $HeCl_2$ B state, homogeneous broadening precludes exciting a single rotational level. In these cases ω_1 was tuned to the maximum intensity position on the vibrational band contour. Thus, the measured probe laser spectra represent the fragment state distribution averaged over the contributions of the initial set of rotational states prepared by the pump laser. In order to compare the fragment population distributions for decomposition of the high vibrational states to those of the lower vibrational

states, Cl_2 fragment spectra for the lower $HeCl_2$ (B) vibrational levels were also recorded with ω_1 tuned to the maximum intensity position on the $HeCl_2$ bandhead so that a distribution of both even- and odd-parity states with substantial contributions from $HeCl_2$ rotational levels with $J = 1,2,$ and 3 were prepared. Population distributions extracted from these spectra are shown in Fig. 8. A summary of the results is tabulated in Table 3. Since the even- and odd-parity states undergo independent dynamics, the even and odd j distributions are normalized and tabulated independently in Fig. 8 and Table 3.

The "initial rotational-state averaged" results of Fig. 8 and Table 3 differ from the rotationally state-selected distributions in Tables 1 and 2 in that the distinct population minimum at $j = 6,7$ is no longer clearly apparent and that j_{max} is one or two quanta higher. The slightly increased j_{max} probably results from the contributions of higher total angular momentum $J = 2,3$ states of $HeCl_2$. The disappearence of the node in the distribution clearly results from averaging over initially prepared rotational states. Nodes in the fragment rotational state population distributions for the $J = 2,3$ rotational levels may appear at different positions or may disappear altogether so that averaging over these levels obscures nodes in the measured rotational distributions. The anharmonicity of the Cl-Cl potential causes E_{avail} to

Table 3:

Summary of the fragment rotational state population distributions for dissociation of $HeCl_2$ (B,υ') for averaged initial rotational state given in Fig. 8.

Prepared $He^{35}Cl_2$ (B) state: υ'

	υ									
	parity									
	6		8		12		20		24	
	+	−	+	−	+	−	+	−	+	−
$\langle E_{rot} \rangle$/cm^{-1}	6.2	6.3	5.9	5.8	4.5	5.1	2.2	2.1	1.9	2.4
$E(j_{max})$/cm^{-1}	40.3	35.5	38.5	34.0	34.3	30.3	18.4	16.0	10.4	12.1
E_{avail}/cm^{-1}	186.7		165.3		121.8		~46.0		~19.5	
Probe Trans. $\upsilon(E) \leftarrow \upsilon(B)$	0←5		0←7		4←11		18←19		13←23	

FIG. 8. $^{35}Cl_2$ fragment rotational state population distributions for the $\Delta\upsilon=-1$ vibrational channel. These values were extracted from the fragment probe laser spectra when the pump laser was tuned to the maximum of the $He^{35}Cl_2$ $B \longleftarrow X$ ($\upsilon' \longleftarrow 0$) bands (a superposition of initial rotational levels is prepared). (a), (b), (c), (d), and (e) show the distributions for υ' = 6, 8, 12, 20, and 24, respectively. The even j distributions (filled circles) and odd j distributions (open circles) are independently normalized to 100 %.

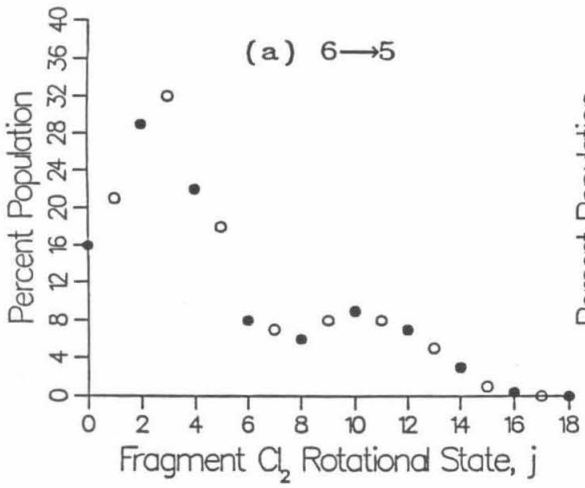
(a) 6⟶5
Percent Population
0 4 8 12 16 20 24 28 32 36 40
0 2 4 6 8 10 12 14 16 18
Fragment Cl_2 Rotational State, j

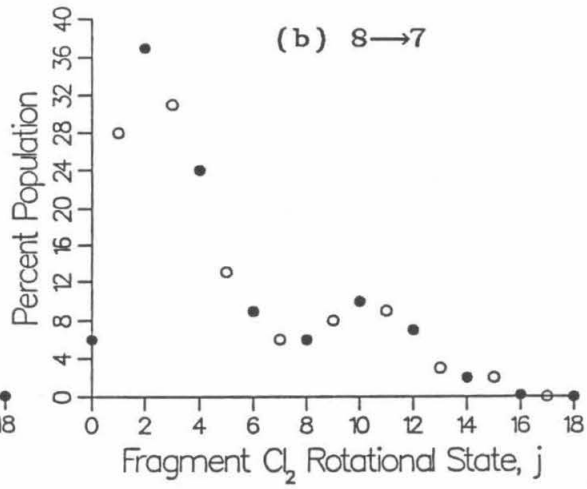
(b) 8⟶7
Percent Population
0 4 8 12 16 20 24 28 32 36 40
0 2 4 6 8 10 12 14 16 18
Fragment Cl_2 Rotational State, j

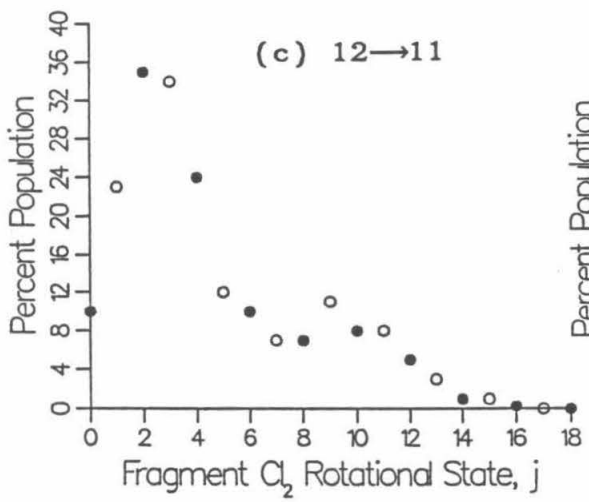
(c) 12⟶11
Percent Population
0 4 8 12 16 20 24 28 32 36 40
0 2 4 6 8 10 12 14 16 18
Fragment Cl_2 Rotational State, j

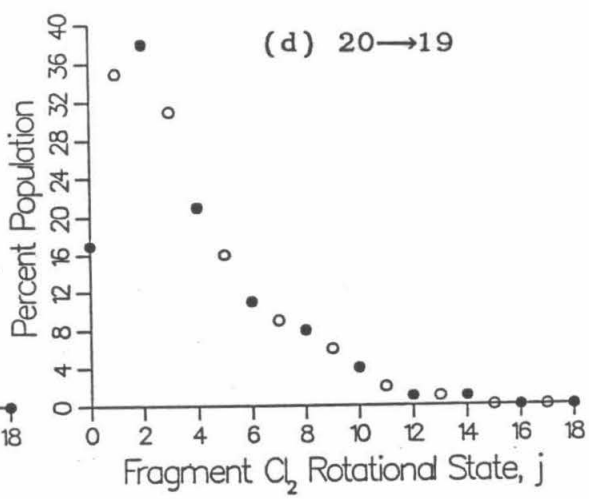
(d) 20⟶19
Percent Population
0 4 8 12 16 20 24 28 32 36 40
0 2 4 6 8 10 12 14 16 18
Fragment Cl_2 Rotational State, j

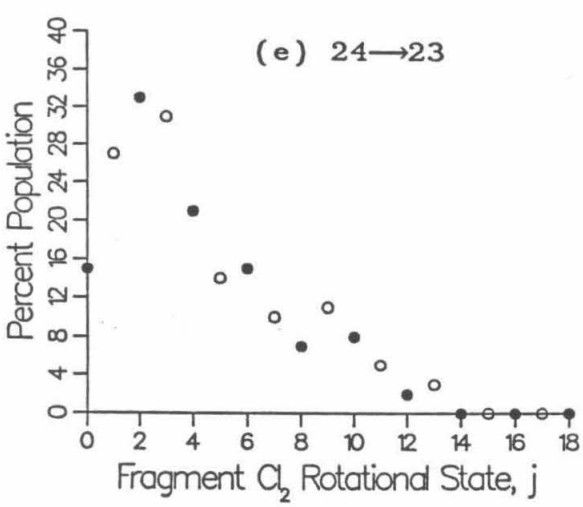
(e) 24⟶23
Percent Population
0 4 8 12 16 20 24 28 32 36 40
0 2 4 6 8 10 12 14 16 18
Fragment Cl_2 Rotational State, j

change by more than a factor of six over the range of vibrational states in Fig. 8 and Table 3. The loss of population in the high-j peak of the rotational distribution for dissociation of the υ' =20 and 24 levels is probably due to kinematic constraints associated with the small value of E_{avail}. For example, observation of j = 14 in the dissociation of the υ' = 8 level corresponds to a classical impact parameter of 2.6 Å, whereas j = 10 for dissociation of the υ' = 20 level corresponds to a classical impact parameter of 3.6 Å. The large increase in the impact parameter results from the much lower relative velocity of the fragments in the dissociation of the high υ' levels. Note that, because of the υ' dependence of the Cl_2 rotational constant, the average rotational energy of the fragments, $\langle E_{rot} \rangle$, decreases with increasing υ' so that rotation still accounts for a relatively small fraction of E_{avail} even for the high υ' levels.

Although only the $\Delta\upsilon$ = -1 channel was observed in the decomposition of the υ' = 6 and 8 states of $HeCl_2(B)$, in the decomposition of the υ' = 12 state approximately 5% and <1% of the fragment population appear in the $\Delta\upsilon$ = -2 and $\Delta\upsilon$ = -3 channels, respectively. Despite the large homogeneous broadening of the υ' = 12, it is possible to position ω_1 so that only the $0_{00} \leftarrow 1_{01}$ transition is significantly excited. Rotational distributions for

decomposition of the $J = 0_{00}$ level of $HeCl_2$ (B,υ=12) are shown in Fig. 9. It is apparent that although the available energy increases by more than a factor of three from the $\Delta\upsilon = -1$ to the $\Delta\upsilon = -3$ channels, j_{max} remains constant within our experimental error. The position of the minimum at j=6 also remains unchanged, while the relative population in the high j peak of the distribution increases.

D. Attempts to observe the closing of the $\Delta\upsilon = -1$ channel

As υ' is increased, a point is reached at which the energy in a single vibrational quantum of Cl_2 is no longer sufficient to dissociate the complex (*i.e.* $E_\upsilon < D_0$) so that only the $\Delta\upsilon = -2, -3, \ldots$ channels are energetically allowed. Levy and coworkers[16] first used this effect to measure D_0's for rare-gas I_2 van der Waals molecules. Attempts to measure such a threshold and thereby obtain a direct experimental measurement of D_0 for $HeCl_2$ were prevented by the apparent onset of electronically nonadiabatic relaxation. The observation of the $\Delta\upsilon = -1$ relaxation channel in the decomposition of $HeCl_2$ (B,υ=26) fixes an upper limit of $D_0 < E(\upsilon=26) = 19\ cm^{-1}$. Even though this is likely to be near the threshold for closure of $\Delta\upsilon = -1$, the $\Delta\upsilon = -1$ channel is still dominant. Because of low signal levels for $\upsilon' \geq 20$, a quantitative estimate of the partitioning among the vibrational

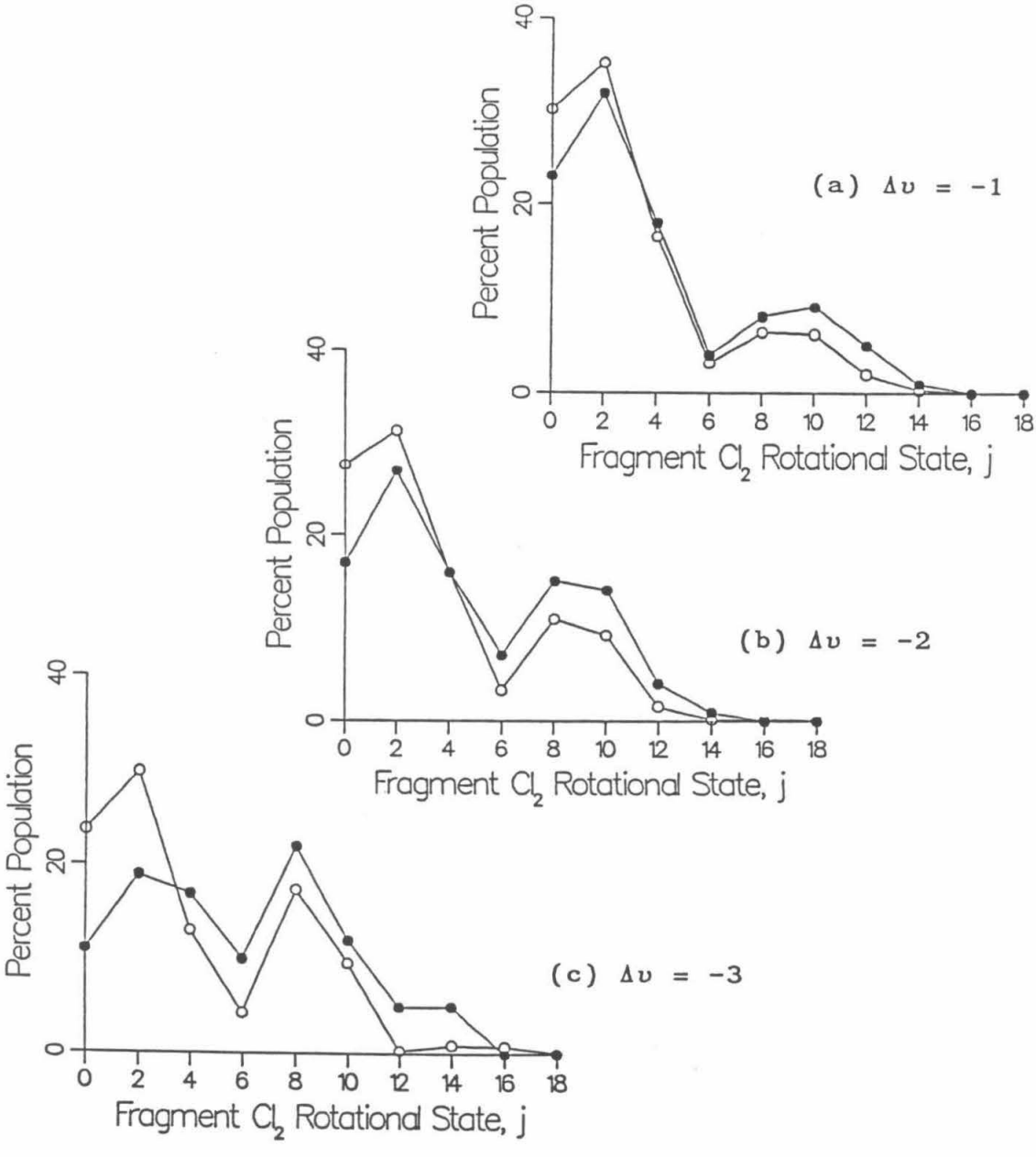

FIG. 9. Rotational state population distributions for dissociation of the J = 0 level of $He^{35}Cl_2(B,\upsilon'=12)$. The $\Delta\upsilon$ = -1 vibrational channel (a) accounts for most of the fragment population. The $\Delta\upsilon$ = -2 channel (b) accounts for ~5 % and the $\Delta\upsilon$ = 3 channel (c) for less than 1 % of the total fragment population. Experimental data are the filled circles, while open circles are calculated distributions.

channels is not possible. The experimental signal became increasingly weaker at higher υ' and no signal for $HeCl_2$ (B,υ'>26) could be observed. However, the $\Delta\upsilon = -1$ channel remained the dominant channel for all the vibrational bands studied.

A possible explanation for the degradation in the intensity of successively higher vibrational levels is that the perturbation of Cl_2 caused by the He atom enhances the electronic predissociation rate of Cl_2 (B) [see Sec. III(B)] to a level competitive with the vibrational predissociation. These vibrational levels lie just below the dissociation threshold of the Cl_2 B electronic state (the classical outer turning point for Cl_2 (B,υ=27) is 6 Å![22]). This effect would prevent fragment detection in the experiment. Strong double resonance signals were obtained for Cl_2(B,υ'=27); the electronic predissociation rate of this vibrational level of free Cl_2(B) is still slow relative to the ~10 ns time scale of the pump-probe experiment. Our result does not prove conclusively that electronic predissociation is responsible for this effect; however, we can offer no other simple explanation for these observations.

IV. CALCULATIONS

A. Potential Energy Function

One of the primary goals of this work is the

construction of a quantitatively accurate potential energy surface for $HeCl_2$. Modeling the dynamical and spectroscopic data reported above demands a flexible functional form for the potential surface. On the other hand, the time-consuming nature of the calculations described below places practical constraints on the number of parameters that can be adjusted. It is desirable to have the potential surface described by a function containing a small number of adjustable parameters that alter the potential in a physically obvious way.

Reid, *et al.*[33] calculated bound levels of rare-gas Cl_2 van der Waals molecules for model potential energy surfaces. That study used a highly flexible (Legendre parameter expansion) potential form. We found that our initial attempts at modeling the experimentally observed dynamics of $HeCl_2$ were quite successful using the simpler atom-atom potential form described below and that further refinement gave good agreement with the spectroscopy as well.

In this paper we use the notation of Ref. 33 to describe the degrees of freedom of $HeCl_2$. This coordinate scheme is depicted in Fig. 10. The internal coordinates of $HeCl_2$ are the He to Cl_2 center-of-mass distance, R, the Cl-Cl bond length, r, and γ, which is the angle between the vectors $\hat{R}$ and $\hat{r}$ along which R and r are measured. We use a modified form of the potential energy function of

FIG. 10. (a) shows the relationship of the molecule-fixed frame (x,y,z) to the space-fixed frame (X,Y,Z) for a generalized atom-diatom system A-BC. The molecule-fixed frame is rotated from the space-fixed frame by the Euler angles $(\phi,\theta,0)$. (b) shows the internal coordinates in the molecule fixed frame. R is the distance from the atom, A, to the center-of-mass of the diatom, BC. r is the B to C distance and γ is the angle between the lines along which R and r are measured. χ is the angle between the xz plane and the plane of the molecule. For clarity, γ has been chosen as $\pi/2$. Both coordinate frames have their origins at the center-of-mass of the A-BC system.

This figure and caption are courtesy of Brian Reid.

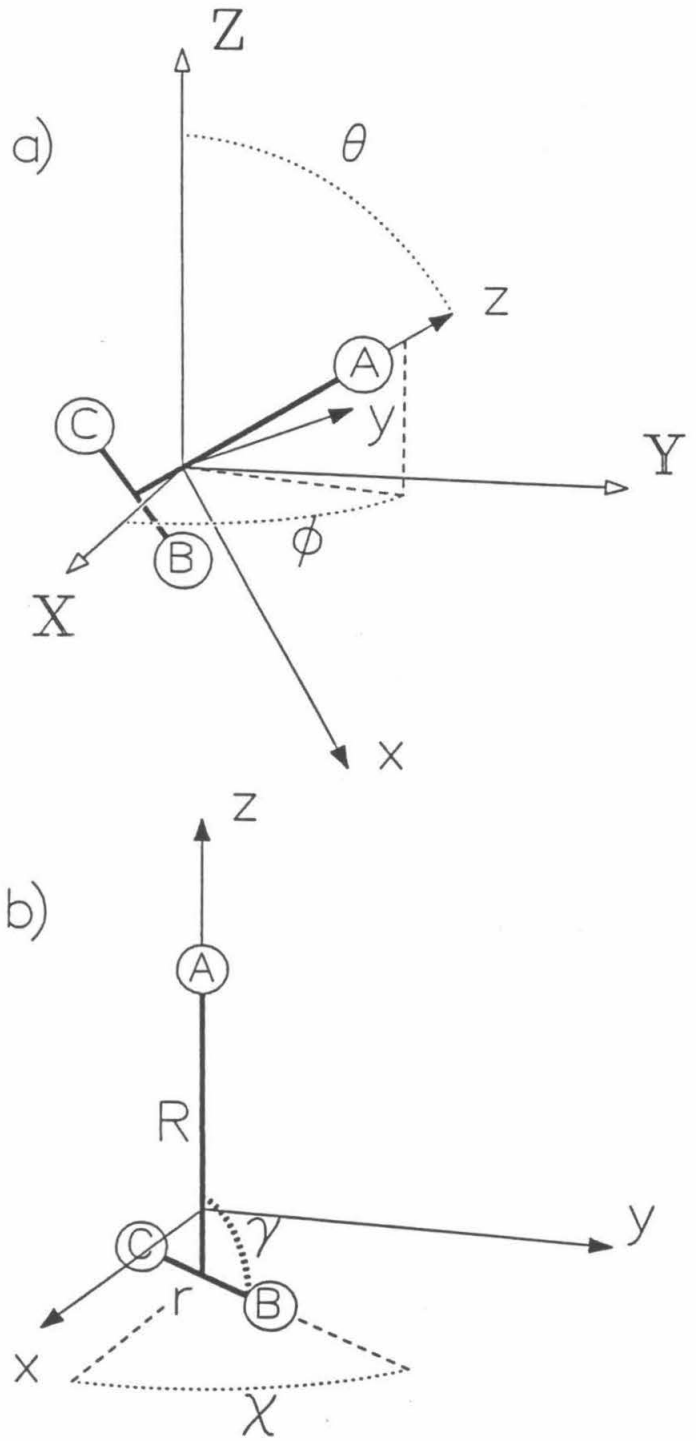
a)
Z
θ
z
A
y
C
Y
B
φ
X
x
b)
z
A
R
y
C
γ
r
B
x
χ

Halberstadt, *et al.*,[34] given by

$$V(r,R,\gamma) = V_M(r,R,\gamma) \qquad \text{if } \min(x_1,x_2) \le x^* \tag{3a}$$

$$V(r,R,\gamma) = [V_M - V_{vdW}]\cdot\exp\left[-\rho\left[\frac{\min(x_1,x_2)-x^*}{x_m}\right]^2\right] \qquad \text{if } \min(x_1,x_2) > x^* \tag{3b}$$

where

$$V_M(r,R,\gamma) = \epsilon_{Cl}\sum_{i=1}^{2}\left[\{1-\exp[-\alpha(x_i-x_m)]\}^2-1\right] \tag{4}$$

and

$$V_{vdW}(R,\gamma) = -\frac{C_6(\gamma)}{R^6} - \frac{C_8(\gamma)}{R^8} . \tag{5}$$

This functional form is used for both the ground (X) and excited (B) electronic states of $HeCl_2$. V_M is a sum of two Morse potentials between the He atom and each Cl atom, and describes the well and hard wall regions of the $He\cdots Cl_2$ potential. The x_i are the He to Cl atom distances given by

$$x_{1,2} = R^2 + \frac{r^2}{4} \pm rR\cos\gamma , \tag{6}$$

and x_m is the position of the minimum of the Morse potentials. V_M is smoothed into the long-range anisotropic van der Waals potential, V_{vdW}, appropriate for $HeCl_2$. The smoothing is initiated at the inflection point of the atom-atom Morse potentials, $x^*=x_m+\ln(2)/\alpha$. The

parameter ρ controls the strength of the smoothing function. The anisotropic van der Waals coefficients[35] are expressed as two term Legendre expansions; *e.g.*, $C_6(\gamma) = C_{6,0} + \frac{1}{2}C_{6,2}(3\cos^2\gamma-1)$.

This functional form places rather rigid constraints on the shape of the potential but has the advantage of relatively few adjustable parameters. Only $\epsilon_{Cl}(X)$, $\epsilon_{Cl}(B)$, $x_m(X)$, $x_m(B)$, and α were varied systematically in fitting the spectroscopic and dynamic data. (The same value for α was used for both electronic states.) The set of potential paramters that provided the optimal simultaneous agreement with all the available experimental data are given in Table 4. The sensitivity of the spectroscopy and dynamics calculations to these parameters is discussed in more detail in the following sections. Of course, the optimum choice of a value for one parameter is determined by the values of the other parameters. With the exception of ϵ_{Cl}, the parameters were optimized to fit experimental results for $HeCl_2$. As discussed in Sec. III(B), we were unable to measure directly the binding energy, D_0, of $HeCl_2$. The value of D_0 for $HeCl_2$ in the B electronic state can be estimated to be ~11 cm^{-1} by scaling the experimentally measured D_0's for the related systems HeI_2, NeI_2,[16] and $NeCl_2$.[36] The values of α and ϵ_{Cl} were adjusted to give good agreement with the calculation of the vibrational predissociation dynamics

Table 4: Potential Parameters for $HeCl_2$

$\epsilon_{Cl}(X) = 16.5\ cm^{-1}$

$x_m(X) = 3.55$ Å

$\rho = 4$

$\alpha = 1.6$ Å^{-1}

$C_{6,0} = 13.3 \times 10^3\ cm^{-1}$ Å^6

$C_{8,0} = 10.95 \times 10^5\ cm^{-1}$ Å^8

$C_{6,2} = 1.88 \times 10^3\ cm^{-1}$ Å^6

$C_{8,2} = 3.2 \times 10^5\ cm^{-1}$ Å^8

$\epsilon_{Cl}(B) = 14.0\ cm^{-1}$

$x_m(B) = 3.60$ Å

while simultaneously giving a calculated value of D_0 close to the estimated value. A contour plot of $V(r_0,R,\tau)$ for the $X,v''=0$ state of $HeCl_2$ is shown in Fig. 11.

B. Calculation of Bound and Quasibound States

The secular equation method used in this paper for the quantum mechanical calculation of the bound, quasibound, and continuum levels of atom-diatom systems has been fully described by Halberstadt, *et al.*,[34] and Reid, *et al.*;[33] therefore, only a rough outline of the calculations is given here. Using the coordinate scheme of Fig. 10, the vibrational and rotational Hamiltonian for $HeCl_2$ is[34]

$$\mathcal{H} = -\frac{\hbar^2}{2mR^2}\frac{\partial^2}{\partial R^2}R + \frac{l^2}{2mR^2} + \frac{j^2}{2\mu r^2} + V(r,R,\tau) + \mathcal{H}_{Cl_2} . \qquad (7)$$

$\mathcal{H}_{Cl_2}$ is the vibrational Hamiltonian for free Cl_2,

$$\mathcal{H}_{Cl_2} = -\frac{\hbar^2}{2\mu r^2}\frac{\partial^2}{\partial r^2}r + V_{Cl_2}(r) . \qquad (8)$$

The eigenfunctions and eigenvalues of Eq. (8) are $\chi_v(r)$ and $E_{Cl_2}(v)$. In Eqs. (7) and (8) $\mu = \frac{1}{2}m_{Cl_2}$, $m = (m_{He}m_{Cl_2})/(m_{He}+m_{Cl_2})$, j is the rotational angular momentum associated with the rotation of r, and l is the

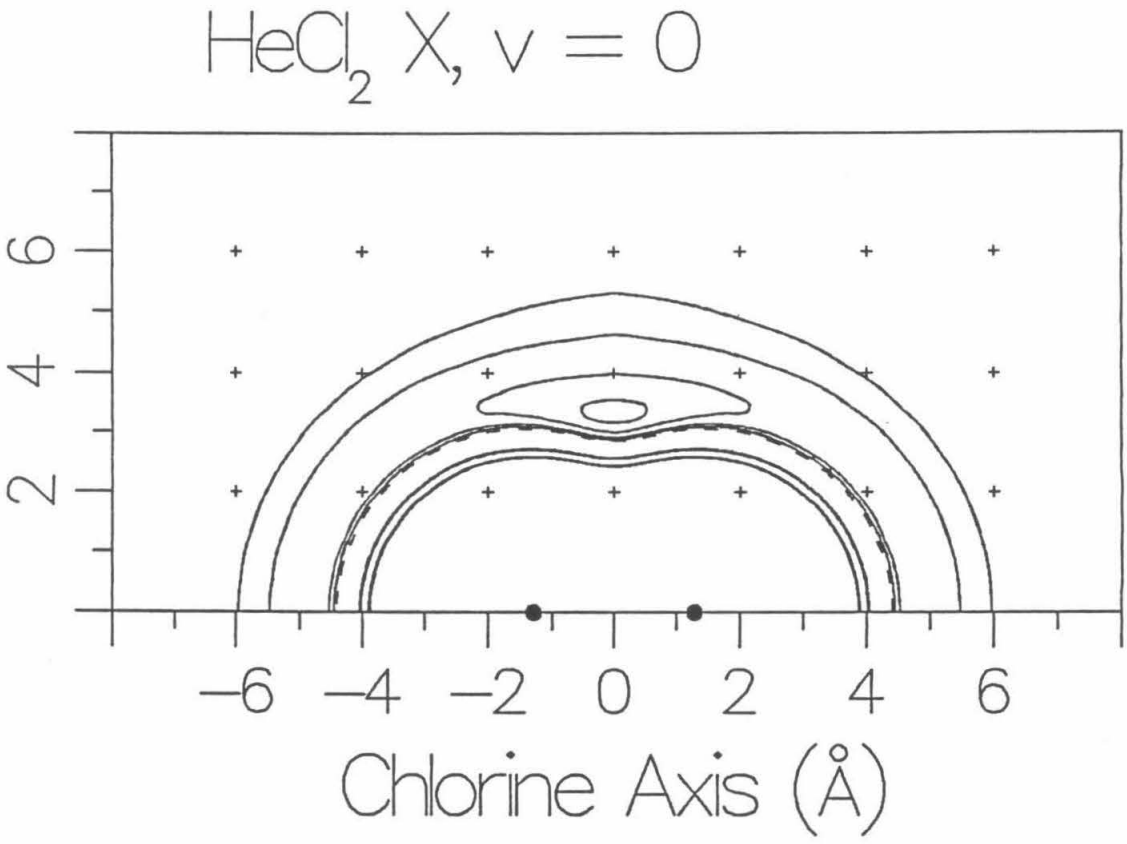

FIG. 11. Equipotential contour plot of the He···Cl_2 potential for the ground electronic state, using the potential parameters in Table 4. The Cl-Cl bond length is set to its vibrationally averaged value of 1.998 Å for $\upsilon = 0$. Contours are drawn at -30, -20, -10, -5, 0 (dashed contour), +100, and +200 cm^{-1}.

orbital angular momentum associated with the rotation of R. The total angular momentum J is thus given by $j+l$. $V(r,R,\gamma)$ is the intermolecular van der Waals potential of Sec. IV(A), and $V_{Cl_2}(r)$ is the intramolecular Cl-Cl vibrational potential from the RKR calculations of Coxon.[22] Both $V_{Cl_2}(r)$ and $V(r,R,\gamma)$ depend upon the electronic state of the complex.

The Hamiltonian of Eq. (7) is partitioned to decouple the He•••Cl_2 motion from the Cl-Cl vibration[37] so that the van der Waals levels are calculated for an effective He•••Cl_2 potential, averaged over the Cl-Cl vibrational motion. Following Ref. 34, we define the zero-order Hamiltonian

$$\mathcal{H}_{\upsilon,\upsilon} = -\frac{\hbar^2}{2mR^2}\frac{\partial^2}{\partial R^2}R + \frac{l^2}{2mR^2} + V_{\upsilon,\upsilon}(R,\gamma) + E_{Cl_2}(\upsilon) + \frac{B_\upsilon}{\hbar^2}j^2 \quad , \tag{9}$$

where $V_{\upsilon,\upsilon}(R,\gamma) = \langle\chi_\upsilon|V(r,R,\gamma)|\chi_\upsilon\rangle$ is the average of the intermolecular potential [Eq. (3)] over the Cl_2 vibrational wavefunctions, and B_υ is the rotational constant of Cl_2 in vibrational state υ. The zero-order wavefunctions are given by

$$\Psi^{o}_{\upsilon k}(r,R) = \chi_\upsilon(r)\ \psi_{\upsilon k}(R,\hat{r}) \quad , \tag{10}$$

where $\psi_{\upsilon k}$ is an eigenfunction of $\mathcal{H}_{\upsilon,\upsilon}$. The $\psi_{\upsilon k}(R,\hat{r})$ are calculated by diagonalization of the zero-order Hamiltonian matrix for a set of basis functions constructed as products of harmonic oscillator functions, $\Phi_n(R)$, which describe the radial motion of the van der Waals bond and angular basis functions, $\theta_{j\Omega}^{JMp_i}(\hat{R},\hat{r})$ (see Appendix 1), which describe the internal bending and overall rotation of the complex. In the $\theta_{j\Omega}^{JMp_i}(\hat{R},\hat{r})$, M is the quantum number associated with the projection of the total angular momentum, J, on the spaced fixed Z-axis; Ω is the projection of J on the body fixed z-axis; and $p_i = \pm 1$ is the inversion parity of the angular basis function. It is shown in Ref. 33 that $\mathcal{H}_{\upsilon,\upsilon}$ does not couple angular basis functions having different values of J, M, and p_i. Furthermore, $\mathcal{H}_{\upsilon,\upsilon}$ will not couple angular basis functions with j even (odd) to those with j odd (even). The eigenfunctions of $\mathcal{H}_{\upsilon,\upsilon}$ can thus be labeled as $\psi_{p_j}^{JMp_i}$, where $p_j = +1$ (even) or -1 (odd) indicates the parity of the state. The p_j parity is the same Cl exchange parity discussed in Sec. III(A).

The results of the bound state calculation for the rotationless J=0 levels of the X,υ'' = 0 and B,υ' = 8 state are given in Table 5 for the potential determined by the parameters of Table 4. The energy of the lowest bound state of $HeCl_2$(B,υ'=8) gives the binding energy,

Table 5:
Bound state energy levels of the X, $\upsilon' = 0$, $J = 0$ and the B, $\upsilon' = 8$, $J = 0$ states of $HeCl_2$. b indicates the number of quanta in the van der Waals bending mode along the coordinate γ.

Bending State b	Energy/cm^{-1} relative to dissociation threshold	
	X, $\upsilon'' = 0$	B, $v' = 8$
0	-12.82	-9.39
1	-7.43	-4.65
2	-5.74	-3.61
3	-3.42	-0.31

$D_0 = -9.39\ cm^{-1}$. The three higher van der Waals vibrational bound states involve excitation of the bending mode about the angle γ. There are no bound levels involving the van der Waals stretch along the R coordinate in either the X or B electronic states.

The blue shift of the $HeCl_2$ B←X, υ'←0 band origins from the corresponding Cl_2 B←X, υ'←0 band origins is a measure of the difference $D_0(X)-D_0(B)$. From Table 5 the calculated blue-shift of the $HeCl_2$ B←X 8←0 band is $3.43\ cm^{-1}$, close to the experimental value of $3.49\ cm^{-1}$. Calculated and experimental blue shifts for other vibrational bands are presented in Table 6. The blue shift increases with υ', which means that the B state binding energy, $D_0(B)$, decreases with the number of quanta in the Cl-Cl stretching mode. This is the result of the averaging of the intermolecular potential $V(r,R,\gamma)$ over the Cl_2 wavefunction to give the effective potential, $V_{\upsilon,\upsilon}(R,\gamma)$.

Fig. 12 shows the ψ_1^{001} wavefunction and associated probability density for the $\upsilon' = 8$, B electronic state (the rotationless, ground van der Waals vibrational level). Note that there is significant delocalization of the He atom even in the lowest van der Waals vibrational state.

The coupling of the zero-order states to the continuum, which has been neglected in this calculation,

Table 6:

Summary of J=0 bound state and dynamics calculations for $HeCl_2(B,\upsilon')$ and comparison with experimental results of Ref. 6.

	blue shift/cm^{-1}		V.P. Lifetime/ps	
υ'	expt.	calc.	expt.	calc.
6	-	3.37	-	612
7	3.40	3.40	-	436
8	3.49	3.43	506	311
9	3.55	3.47	275	231
10	3.65	3.51	179	170
11	3.72	3.55	97	128
12	3.77	3.60	52	95

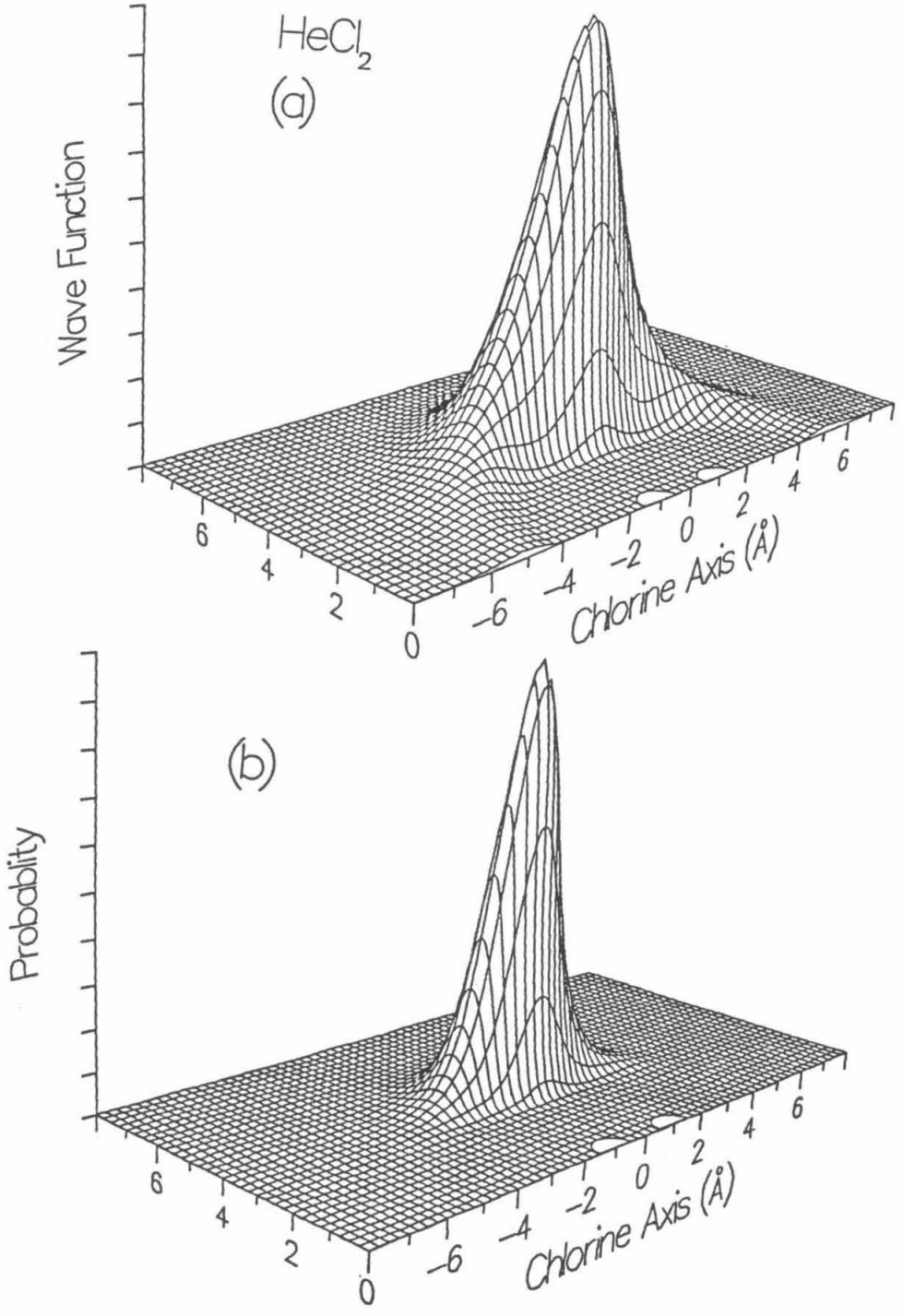

FIG. 12. (a) shows the vibrational wave function of the lowest van der Waals quasibound vibrational level for $He^{35}Cl_2(B,\upsilon'=8,J=0)$. (b) shows the associated probability density.

shifts the energies of the quasibound states slightly. The magnitude of this shift is a measure of the accuracy of the golden rule approximation, which will be used in Sec. IV(D) to calculate the dissociation dynamics. Halberstadt, *et al.*,[34] compared the golden rule treatment of the vibrational predissociation of $NeCl_2$ to an exact line shape calculation and found that the center of the $NeCl_2(B, \upsilon=11, J=0)$ resonance was shifted by only $0.0425\ cm^{-1}$. Since the coupling of the zero-order states to the continuum is of the same order for both He- and Ne-Cl_2 (He- and Ne-Cl_2 have very similar vibrational predissociation lifetimes), the golden rule approximation should also be valid for $HeCl_2$. Further technical details of the calculation are given in Appendix 2.

C. Spectroscopy

The spectroscopy of the B⟵X bands of $HeCl_2$ can be simulated if bound and quasibound state energies, transition line strengths among these states, and the initial rotational population distribution are known. In this section the calculation of the bound states is extended to levels with $J > 0$ in both the X and B electronic states.

An initial $X, \upsilon''=0, J''_{k_a''k_c''}$ level is coupled by the transition dipole to the quasibound $B, \upsilon', J'_{k_a'k_c'}$ levels. Selection rules and line strengths for these transitions

are determined by the line strength factors $S(\psi^{J'M'p_i'}_{p_j'};\psi^{J''M''p_i''}_{p_j''})$ for transitions between the two levels. Calculation of the line strength factors is described in Appendix 1.

A result of the analysis of Appendix 1 is that the transition selection rules are $\Delta J = 0$ or ± 1, $\Delta p_i = \pm 2$ and $\Delta p_j = \pm 2$. Fig. 13 shows calculated spectra for the $HeCl_2$ B⟵X, 8⟵0 band using the potential parameters of Table 4. The simulated spectrum was calculated for a Boltzmann rotational population distribution, and the line intensities were calculated using Eq.(A7) of Appendix 1. The lines are convoluted with the Voigt profile as was done for the previously described asymmetric top fits. The quality of the simulation was found to be most dependent on the potential parameters $x_m(X)$ and $x_m(B)$, to be expected since these parameters determine the position of the van der Waals well and hence the effective bond lengths R_X and R_B. The simulated spectrum obtained from the secular equation calculation gives a quantitatively better fit to the experimental spectrum than the simulation obtained from the asymmetric top treatment described in Sec. III(A), particularly for the higher rotational levels, although qualitatively the results appear quite similar.

It is interesting is to determine how the bond lengths obtained in the rigid, asymmetric top analysis of

FIG. 13. Solid curves are experimental, parity-selected excitation spectra of $He^{35}Cl_2(B,\upsilon'=8)$ obtained as described in Fig. 4. Stick spectra are line positions involving transitions among levels with $J \lesssim 3$ calculated as described in Sec. IV(C); more important transitions in this study are labeled with the asymmetric top designations for ease of identification. Table 8 shows the symmetry correspondence of these calculated levels and the asymmetric top functions. Dotted curves are simulated spectra convoluted with the proper Voigt lineshape for this vibrational transition. Note the subtle improvement of these fits over those obtained using the asymmetric top model of Fig. 4. (a) shows transitions to even-parity levels; (b) shows transitions to odd-parity levels.

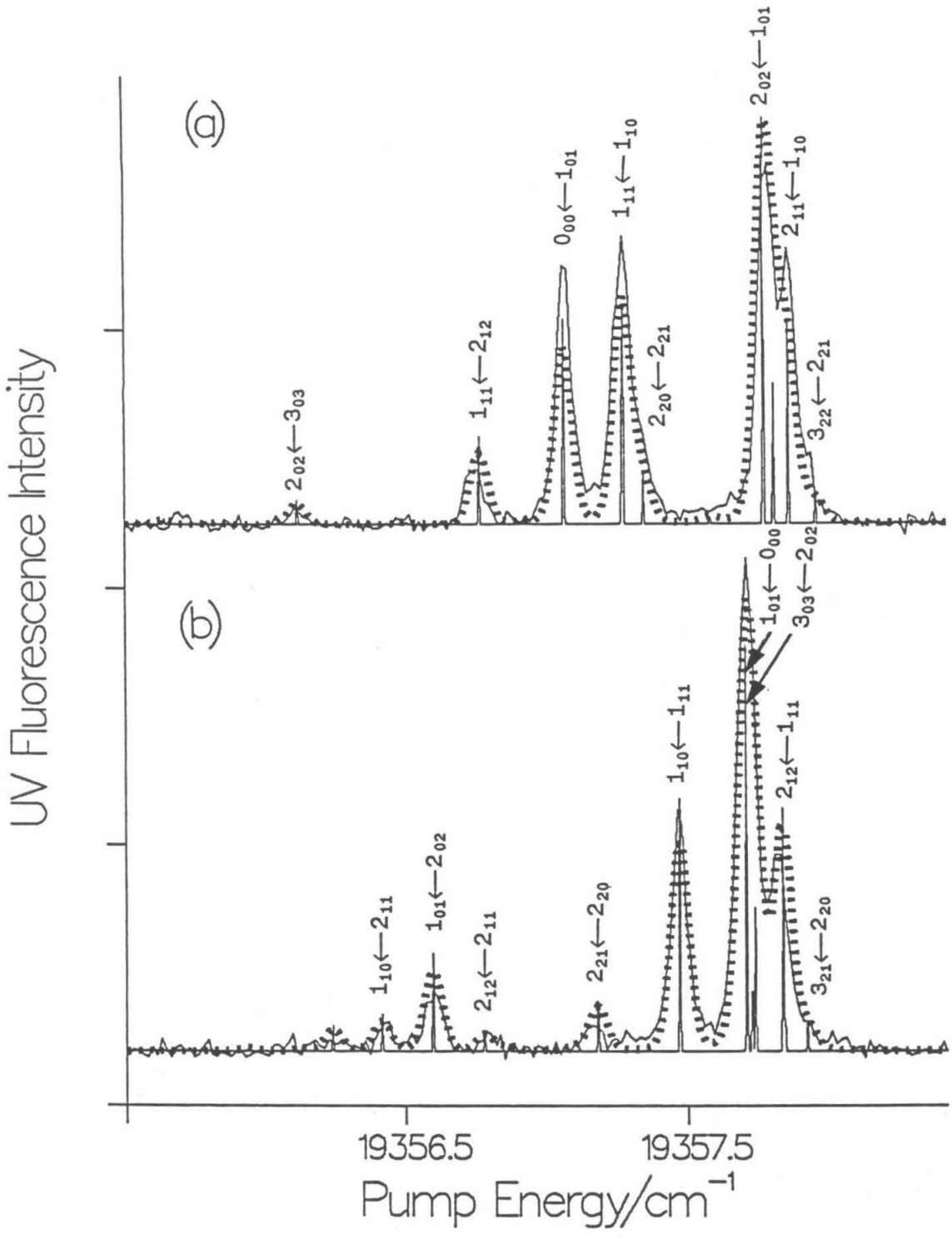
(a)
(b)
UV Fluorescence Intensity
$2_{02}\leftarrow 3_{03}$
$1_{11}\leftarrow 2_{12}$
$0_{00}\leftarrow 1_{01}$
$1_{11}\leftarrow 1_{10}$
$2_{20}\leftarrow 2_{21}$
$2_{02}\leftarrow 1_{01}$
$2_{11}\leftarrow 1_{10}$
$3_{22}\leftarrow 2_{21}$
$1_{10}\leftarrow 2_{11}$
$1_{01}\leftarrow 2_{02}$
$2_{12}\leftarrow 2_{11}$
$2_{21}\leftarrow 2_{20}$
$1_{10}\leftarrow 1_{11}$
$1_{01}\leftarrow 0_{00}$
$3_{03}\leftarrow 2_{02}$
$2_{12}\leftarrow 1_{11}$
$3_{21}\leftarrow 2_{20}$
19356.5
19357.5
Pump Energy/cm^{-1}

$HeCl_2$ are related to the potential surface of the molecule and to the average geometry of the complex. In order to compare directly the asymmetric top energy levels to those obtained by diagonalization of the Hamiltonian of Eq. (9), the correlation of the asymmetric top rotational wavefunctions and the $\psi_{p_j}^{JMp_i}$ must first be established. The asymmetric top rotational wavefunctions form a basis for the D_2 point group. Those wavefunctions belonging to the B_a and B_c representations of D_2 are antisymmetric with respect to the C_2^b operator (which exchanges the Cl atoms as seen in Fig. 3), while those belonging to the A and B_b representations are symmetric.[25] Thus, the wavefunctions of B_a and B_c symmetry have odd parity and the A and B_b wavefunctions have even parity. The rotational selection rules for *a*-type asymmetric top transitions are $A \longleftrightarrow B_a$ and $B_b \longleftrightarrow B_c$.[38] The spectrum of Fig. 4a then contains only $A \longleftarrow B_a$ and $B_b \longleftarrow B_c$ transitions, while the spectrum of Fig. 4b contains only $B_a \longleftarrow A$ or $B_c \longleftarrow B_b$ transitions. Reid, *et al.*,[33] showed how to correlate the symmetry of the $\psi_{p_j}^{JMp_i}$ to the asymmetric top wavefunctions. The symmetry correlation for $HeCl_2$ is shown in Table 7.

Table 8 shows how the energy levels obtained in the asymmetric top analysis of Fig. 4 compare with the energy levels calculated using Eqn. (9). With the exception of some of the highest rotational levels of the X state, the

Table 7:
Symmetry Correlation of Calculated Wavefunctions
with Asymmetric Top Functions

Wavefunction Symmetry		Asymmetric Top Symmetry
p_i	p_j	
1	1	A
1	-1	B_b
-1	1	B_c
-1	-1	B_a

Table 8:

Comparison of the rotational energy levels of the ground van der Waals vibrational state of $HeCl_2$ for the asymmetric top (AT) model (calculated for the bond lengths given in Fig. 4) or the secular equation calculation (SE) of Sec. IV(C). The symmetry correlation of the levels is also given. Energy levels are calculated for the $\upsilon'' = 0$ level of the X state and the $\upsilon' = 8$ level of the B electronic state.

Rotational Level			X, υ=0 Energy/cm^{-1}		B, υ=8 Energy/cm^{-1}	
D_2 Rep.	AT $J_{k_a k_c}$	SE $J\ {}^{p_i}_{p_j}$	$E_{AT}(X)$	$E_{SE}(X)$	$E_{AT}(B)$	$E_{SE}(B)$
A	0_{00}	$0\ {}_{1}\ {}^{1}$	0.0	0.0	0.0	0.0
B_a	1_{01}	$1_{-1}\ {}^{-1}$	0.383	0.400	0.233	0.239
B_b	1_{11}	$1\ {}_{1}\ {}^{-1}$	0.470	0.460	0.405	0.407
B_c	1_{10}	$1_{-1}\ {}^{1}$	0.573	0.597	0.448	0.461
A	2_{02}	$2\ {}_{1}\ {}^{1}$	1.098	1.113	0.693	0.708
B_c	2_{12}	$2_{-1}\ {}^{1}$	1.134	1.110	0.829	0.826
B_b	2_{11}	$2\ {}_{1}\ {}^{-1}$	1.443	1.517	0.957	0.990
B_a	2_{21}	$2_{-1}\ {}^{-1}$	1.704	1.691	1.472	1.486
A	2_{20}	$2\ {}_{1}\ {}^{1}$	1.757	1.773	1.479	1.497
B_a	3_{03}	$3_{-1}\ {}^{-1}$	2.091	2.062	1.367	1.383
B_b	3_{13}	$3\ {}_{1}\ {}^{-1}$	2.102	2.058	1.461	1.452
B_c	3_{12}	$3_{-1}\ {}^{1}$	2.701	2.819	1.716	1.775
A	3_{22}	$3\ {}_{1}\ {}^{1}$	2.854	2.830	2.172	2.179
B_a	3_{21}	$3_{-1}\ {}^{-1}$	3.063	3.139	2.206	2.225
B_b	3_{31}	$3\ {}_{1}\ {}^{-1}$	3.574	3.484	3.141	3.132
B_c	3_{30}	$1_{-1}\ {}^{1}$	3.593	3.525	3.141	3.133

agreement between the asymmetric top levels and the secular equation calculation is within a few hundredths of a wavenumber. Although such deviations would be significant in a microwave experiment, this agreement shows that within our experimental resolution the rigid, asymmetric top model can simulate the rovibronic spectrum of this highly non-rigid molecule with surprising accuracy, especially for transitions among the lower rotational levels, which account for the intense features in the B⟵X spectrum.

As expected, the rotational levels of the secular equation calculation given in Table 8 cannot be produced by any single set of asymmetric top rotational constants. The 3.8 Å He•••Cl_2 distance from the asymmetric top fit to the experimental spectrum is the same as the average value of *R* for the probability density of Fig. 12 along $\gamma = 90^\circ$. The bond length derived from the asymmetric top analysis for a T-shaped model thus gives an accurate description of the effective geometry of the complex. The average bond length is significantly longer than the 3.35 Å position of the well minimum along the $\gamma = 90^\circ$ section of the potential surface.

No progressions in the van der Waals vibrational modes could be measured experimentally. Previously, this has been attributed to the similarity of the ground and excited state potential surfaces. However, the line

strength factors calculated for our potential indicate that the transition intensity to the ground van der Waals of the B state mode accounts for roughly 80 % of the total line strength from the ground van der Waals mode of the X state. Most of the remaining strength is to the first excited bending mode, and the line strengths for transitions to successively higher excited levels decrease rapidly. Assuming our potential surface to be accurate, it is unclear why no van der Waals progression is observed. Our experimental signal-to-noise should enable us to measure at least the first combination band. It may be that the excited van der Waals levels are severely homogeneously broadened and are difficult to detect.

D. Dynamics

The zero-order Hamiltonian, $\mathcal{H}_{\upsilon,\upsilon'}$, of Eqn. (9) neglects the weak coupling due to the intermolecular potential, $V(r,R,\gamma)$, among the wavefunctions of Eq. (10). The decay rate of the initially prepared zero-order quasibound state, $\Psi_i^o(R,r) = \chi_{\upsilon_i}(r)\psi_i(R,\hat{r})$, is given within the golden rule approximation by the half-width,[34]

$$\Gamma_i = \pi \sum_{\upsilon_f} \sum_{j_f} |\langle\psi_{\upsilon_f j_f}|V_{\upsilon_i \upsilon_f}|\psi_i\rangle|^2 , \tag{11}$$

where the $V_{\upsilon_i \upsilon_f}(R,\gamma) = \langle\chi_{\upsilon_i}|V|\chi_{\upsilon_f}\rangle$ are the off-diagonal

matrix elements of the intermolecular potential between the Cl_2 vibrational wavefunctions. $\psi_{v_f j_f}(R,\hat{r})$ is a continuum wavefunction that describes the dissociated products. The methodology of the calculation of the continuum wavefunctions and the integration of Eq. (11) are described elsewhere.[34] The partial width,

$$\Gamma_{i \longrightarrow v_f j_f} = |\langle \psi_{v_f j_f} | V_{v_i v_f} | \psi_i \rangle|^2 , \tag{12}$$

is proportional to the population of Cl_2 fragments appearing in the vibrational state v_f with the rotational quantum number j_f. The lifetime of the initial state is given by $\tau = \frac{\hbar}{2\Gamma_i}$.

The coupling potential, $V_{v_i v_f}$, is symmetric with respect to rotations of $\gamma = \pi$ in Fig. 10. In order for the matrix elements of Eq. (12) to be non-zero, both ψ_i and $\psi_{v_f j_f}$ must be either symmetric ($p_j = 1$) or antisymmetric ($p_j = -1$). This requirement leads to parity conservation in the dynamics calculations.

Dynamics calculations were performed for dissociation of the $J = 0$ level of the ground van der Waals vibrational state. The results of the calculations are compared with experiment in Table 6 and in Figs. 9 and 14. The calculated vibrational predissociation lifetimes fall within a factor of two of the experimental values;

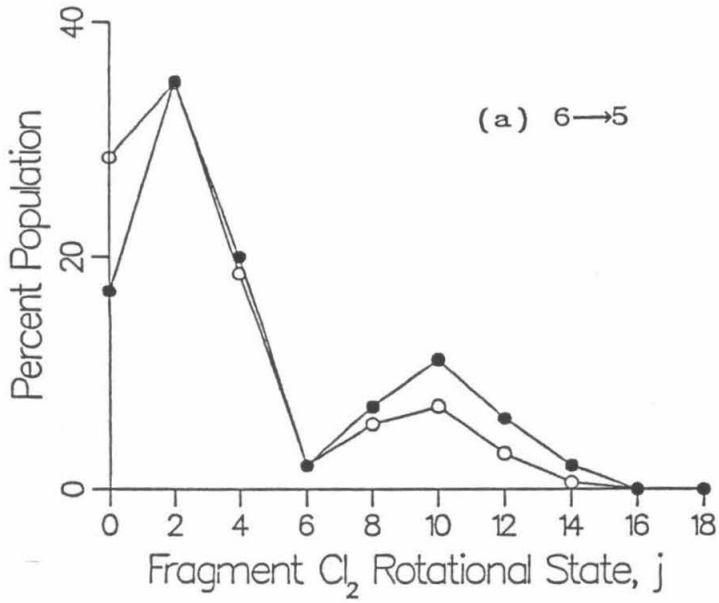

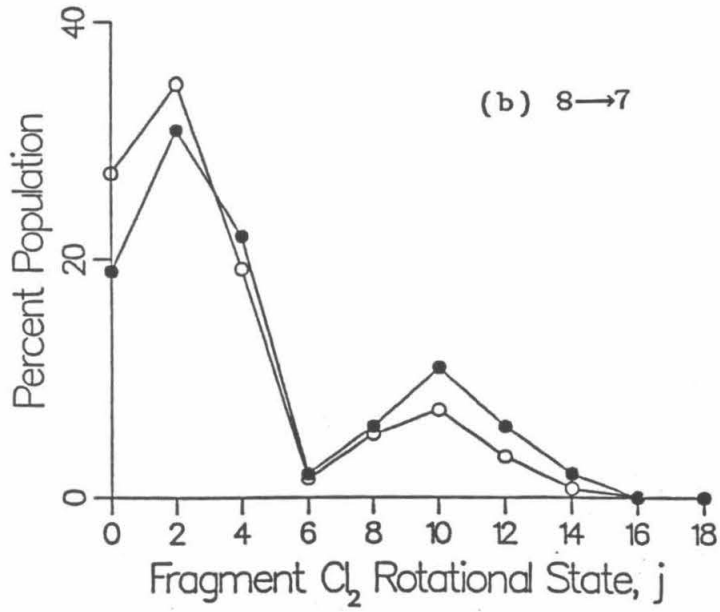

FIG. 14. Comparison of experimental and calculated fragment rotational population distributions for vibrational predissociation of the $J = 0$ level of $He^{35}Cl_2(B,\upsilon')$. (a) is for $\upsilon' = 6$; (b) is for $\upsilon' = 8$. Filled circles represent experimental data; open circles are calculated rotational distributions.

however, the calculated lifetimes decrease more slowly with υ' than do the actual lifetimes. Calculated rotational and vibrational population distributions also show good agreement with experiment. Both the minimum in the fragment rotational population distribution at $j = 6$ and the second maximum are evident, but the calculated fractional population in the second maximum is smaller than was observed experimentally. The population of the $\Delta\upsilon' = -2$ vibrational channel in the decomposition of $HeCl_2(B,\upsilon'=8,J=0)$ accounts for 1 % of the total population. Experimentally, we estimate the population of this channel to be less than 1 %. Fig. 9 compares the experimental and calculated rotational distributions for the decomposition of $HeCl_2(B,\upsilon'=12,J=0)$ level. The calculated population distribution among the $\Delta\upsilon = -1,-2$, and -3 channels is 96.6, 3.3, and 0.1 %, respectively, again in good agreement with experiment. In both the experimental and calculated rotational distributions, the relative population of the higher j peak increases with the number of Cl_2 vibrational quanta transferred in the fragmentation; however, this effect is not as dramatic in the calculation. In all cases the calculated population in the second peak of the rotational distribution is not as large as is observed experimentally, whereas the calculated low j populations are larger than observed. The overall agreement of the calculation with the

experiment is, however, remarkable, considering the simplicity of our potential energy surface.

The rotational distributions and lifetimes are relatively insensitive to the value of x_m used in the potential. However, both the lifetime and rotational distributions are extremely sensitive to the values of α and ϵ_{Cl}. For example, decreasing α by 0.4 $Å^{-1}$ increases the lifetime by several hundred picoseconds. The lifetime also varies inversely with ϵ_{Cl}. Holding other parameters constant, decreasing ϵ_{Cl} from 16 to 10 cm^{-1} increases the lifetime by approximately four hundred picoseconds. For a given value of ϵ_{Cl}, it is possible to adjust α to obtain the correct experimental lifetime for a given initial vibrational level.

Both the position of the intervening minimum and the high j tail of the fragment rotational distribution are shifted to larger j values as α is increased; high values of α lead to greater rotational excitation in addition to shorter lifetimes. Decreasing the value of ϵ_{Cl} enhances considerably the minimum in the rotational distribution.

It is possible to adjust the potential parameters to bring the dynamics calculation into essentially quantitative agreement with the data. Choosing $\epsilon_{Cl} = 8\ cm^{-1}$, $\alpha = 1.8\ Å^{-1}$, and $x_m = 3.65$ Å gives $\tau = 680$ ps and an excellent reproduction of the observed

rotational distribution. Such a potential, however, has a well minimum of only 16 cm^{-1}, which supports only one bound state with a binding energy, $D_0(B)$, of 2.8 cm^{-1}. These values are unrealistically small when compared to data from related systems [See Sec. IV(A)]. The values of the parameters in Table 4 were selected to give the best simultaneous agreement with all the available data.

V. DISCUSSION

The success of the atom-atom additive potential in these calculations is particularly exciting because it suggests that simple potential energy surfaces constructed in this manner for closely related van der Waals molecules may be reasonably accurate. It is interesting to compare our He•••Cl Morse potential to the experimentally measured potentials for the nearly isoelectronic He•••Ar system.[39] Our value of $\epsilon_{Cl}(X) = 16.5$ cm^{-1} is close to the value of 20.4 cm^{-1} for ϵ(He•••Ar). The position of the He•••Cl well minimum, $x_m(X) = 3.55$ Å, is slightly longer than the 3.50 Å value for the He•••Ar potential. It appears that the use of atom-atom potentials derived from rare-gas scattering data provides a good initial estimate of the intermolecular potentials of simple, rare-gas halogen van der Waals systems.

O'Loughlin[35] has performed a crossed-beams scattering experiment on He•••$Cl_2(X,\upsilon''=0)$; however, the

results did not lead to a unique determination of a potential. Both the well depth, $D_e(X) = 33\ cm^{-1}$ and anisotropy, $\Delta R_e(X) = 1.14$ Å of our potential fall within the range of values spanned by the two best potentials proposed in that study.

It is important to distinguish the origins of parity conservation in this experiment from an effect observed in another recent photodissociation experiment. Valentini, *et al.*,[40] have studied the photodissociation of ozone and have shown that formation of the homonuclear $^{16}O_2(^1\Delta_g)$ fragment occurs with preferential population of the even j rotational levels. This is due to selective depletion of the odd j population by a second decomposition channel to give the $^{16}O_2(^3\Sigma_g)$ fragment which can have only odd j rotational levels because of nuclear exchange symmetry. Heteronuclear $^{16}O^{18}O$ fragments show no preferential population of either even or odd rotational levels; the symmetry selection rule in the decomposition of ozone is due solely to nuclear exchange symmetry effects. The parity conservation observed in $HeCl_2$ is completely distinct from the electronically non-adiabatic ozone decomposition. The symmetry selection rules in the photodecomposition of $HeCl_2$ result from the symmetry of the $He\cdots Cl_2$ van der Waals potential; the effect is observed for both $He^{35}Cl_2$ and $He^{35}Cl^{37}Cl$. This effect is precisely the half-collision analogue of the $\Delta j = \pm 2, 4, \ldots$

selection rule in rotationally inelastic scattering. Since the center-of-mass of the $^{35}Cl^{37}Cl$ species does not lie precisely half the distance between the Cl nuclei, parity conservation should not, in principle, be complete. However, breakdown of the selection rule for $He^{35}Cl^{37}Cl$ is too small to be accurately measured in this experiment.

The general features of the vibrational predissociation dynamics of $HeCl_2$, that is, the $\Delta v = -1$ vibrational propensity rule and the small degree of rotational excitation of the Cl_2 fragment, follow closely the predictions of the now well-established propensity rules for vibrational energy transfer in van der Waals molecules.[41] The details of the rotational distributions, however, merit further discussion.

The unusual bimodal structure observed in the rotational distributions of the Cl_2 fragment cannot be explained as a result of averaging over initial states; complete rotational and vibrational initial state selection has been achieved. The quantum mechanical calculations provide assurance that our potential energy surface is a reasonable representation of the forces, but like the experimental results, they do not immediately lead to a simple physical picture for the dynamics. An analysis of the dynamical data in terms of other theoretical approaches is beyond the scope of the present paper, but we consider two simple treatments briefly: a

classical impulsive dissociation and the Franck-Condon approximation for dissociation.

First, we consider the classical dissociation. In a theoretical study of the vibrational predissociation of the H_2Ar van der Waals molecule, Hutson, *et al.*[42] calculated bimodal rotational distributions and suggested that they were the result of oscillatory rainbow structure associated with a classical rotational rainbow. More recent theoretical studies have explored rotational rainbow features observed in the rotational distributions of diatomic fragments of the direct photodissociation of covalently bound molecules. By simply treating the impulsive dynamics on the dissociative electronic potential surface classically, and weighting the classical trajectories by the initial wavefunction, qualitative agreement has been obtained with experimentally observed fragment rotational distributions for the direct photodissociation of several small molecules.[43] It is possible to draw an analogy between the latter treatments and vibrational predissociation. The optical transition that couples a bound state to the continuum on a repulsive electronic potential surface is analogous to the small potential couplings that lead to the decay of a zero-order quasibound level of a van der Waals molecule to the continuum of unbound vibrational states. In this method, classical trajectories are computed for different

initial angular configurations, γ_0, of the atom-diatom system to obtain the "classical excitation function," $j(\gamma_0)$, which gives the final angular momentum of the system following dissociation. A rotational rainbow results when $j(\gamma_0)$ passes through a maximum, resulting in a singularity in the classical rotational distribution. Fig. 15 shows the results of classical trajectory calculations for the impulsive dissociation of $HeCl_2(B,\upsilon'=12,J=0)$ on our B,v' = 11,10, and 9 potential surfaces. In these calculations the initial relative velocity of the fragments is set to zero, and trajectories were run for a variety of initial angular configurations to obtain $j(\gamma_0)$. The initial $He\cdots Cl_2$ distance, R, is fixed by conservation of energy; the available energy for the various product channels is determined by the number of Cl_2 vibrational quanta transferred in the decomposition. The trajectory calculations predict that the position of the classical rainbow should move from $j \approx 8$ for the $\Delta\upsilon = -1$ channel to $j \approx 13$ for the $\Delta\upsilon = -3$ channel. However, the second maximum of the experimental rotational distribution (which would be associated with the rotational rainbow) is insensitive to the available energy. For this reason we believe that the second maximum of the distribution cannot be attributed simply to a rotational rainbow effect.

A limiting case in photodissociation theory is the

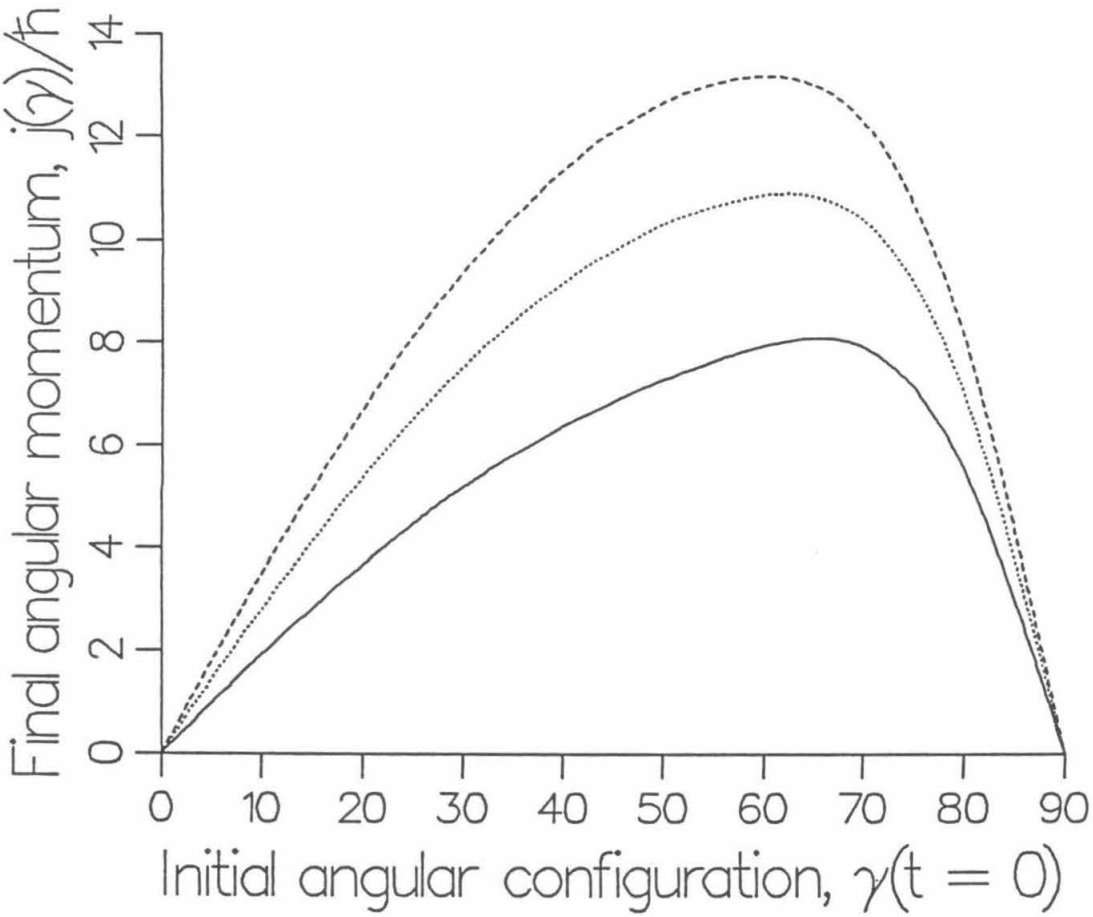

FIG. 15. Classical trajectory calculations for impulsive dissociation of $HeCl_2(B,\upsilon'=12,J=0)$ on the $He\cdots Cl_2(B,\upsilon'=11)$ potential surface. Solid curve shows the final angular momentum of the $\Delta\upsilon = -1$ channel Cl_2 fragment, j, as a function of $\gamma(t=0)$, the initial angular geometry of the complex. The dotted curve is calculated for the $\Delta\upsilon = -2$ channel and the dashed curve is for the $\Delta\upsilon = -3$ channel. See text for initial conditions. The method used to compute the classical trajectories is discussed in Appendix A to this thesis.

Franck-Condon approximation,[3] in which the relative final rotational populations are given by the overlap of the initially prepared state with the free rotor states, Y_{j0},

$$N(j) = |\langle\psi_i|Y_{j0}\rangle|^2 \quad . \tag{13}$$

The result of this treatment, using the wavefunctions calculated in Sec. IV(B), is presented in Fig. 16. The Franck-Condon distribution does show weak oscillatory structure, but it falls off much more rapidly than does the experimental distribution. However, a more sophisticated version of the Franck-Condon theory[44] may successfully model the observed dynamics. This is suggested by the insensitivity of the distributions to the available energy and the low degree of rotational excitation.

Yet a third possibility is that the bimodal distribution is the result of a quantal interference effect. Within a semiclassical picture, this results from the superposition of two or more trajectories originating from different configurations of the molecule that give rise to the same final rotational state of the fragment. The near or total node in the rotational distributions (which result from the decay of a single initial level) suggests that the distributions are truly the result of interferences, and that large j oscillatory features are

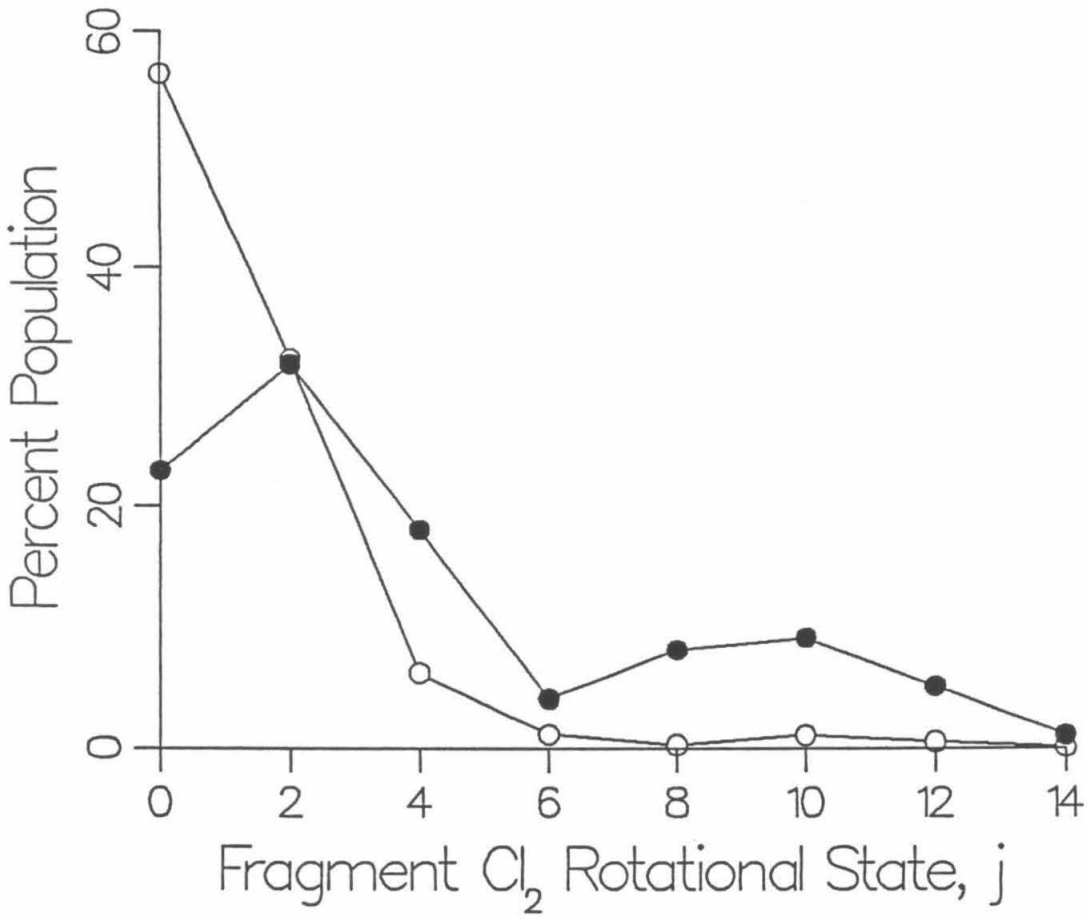

FIG. 16. Decomposition of the wave function of the $He^{35}Cl_2(B,\upsilon'=8,J=0)$ ground van der Waals vibrational level in terms of the $\Omega = 0$ spherical harmonics as a test of the Franck-Condon theory of photodissociation. Open circles show the overlaps given by Eq. (13). Filled circles show the experimental rotational population distribution.

missing because of the unphysically large impact parameters they require. The calculated $\Delta v = -3$ distribution for $HeCl_2(B, v'=12, J=0)$ in Fig. 15 shows a third maximum that appears to be a continuation of this oscillatory structure. Unfortunately, the low fractional population of this vibrational channel did not permit experimental measurement of the third maximum, but given the success of these calculations, we are confident that it exists.

VI. SUMMARY

The dynamics of the photodissociation of $HeCl_2$ has been studied at the state-to-state level. This unprecedented state resolution allows the experimental observation of dynamical symmetry constraints arising from the symmetry of the $He\cdots Cl_2$ van der Waals potential. The major vibrational predissociation product channel is the transfer of one Cl_2 vibrational quantum. Only a small fraction of the available energy appears as fragment rotation; however, the observed fragment rotational population distribution is distinctly bimodal.

The bond lengths extracted from an asymmetric top analysis of the excitation spectra of this molecule provide a reasonable representation of the effective geometry of the complex.

A potential energy surface was constructed for this

molecule on which three-dimensional quantum mechanical calculations were performed. These calculations agree with both the excitation spectroscopy of the complex and the fragmentation dynamics measured in the laboratory. The potential that gave the best agreement between experiment and theory has a binding energy of 12.8 and 9.4 cm^{-1} and He-Cl atom-atom equilibrium distances of 3.55 and 3.60 Å in the ground (X) and excited (B) electronic states, respectively.

The rotational distributions are not consistent with any simple dynamical model for the dissociation. The bimodal rotational distribution may arise from quantal interference effects in the photodissociation dynamics.

VII. ACKNOWLEDGEMENTS

The authors acknowledge the financial support of the National Science Foundation and NATO for an international collaboration grant. We appreciate helpful discussions with Prof. J.A. Beswick.

VIII. APPENDICES

1. Line Strength Factors

This appendix outlines the calculation of the intensities and selection rules for transitions between two energy levels $(J,\{\alpha\})$ and $(J',\{\alpha'\})$. The excited (B) electronic state of $HeCl_2$ is denoted with primes, while

the ground (X) state is unprimed. J is the total angular momentum of the level and $\{\alpha\}$ represents the set of quantum numbers and labels required to completely specify the particular level. The $2J+1$ M-states, $|J,M,\{\alpha\}\rangle$, which comprise the level $(J,\{\alpha\})$, are degenerate in the absence of external fields. The line strength[31,45] for transitions between these levels is

$$S(J',\{\alpha'\};J,\{\alpha\}) = \sum_{M',M} |\langle J',M',\{\alpha'\}|\boldsymbol{\varepsilon}\cdot\boldsymbol{\mu}|J,M,\{\alpha\}\rangle|^2. \qquad \text{(A1)}$$

The sum is over all M and M' states, $\boldsymbol{\varepsilon}$ is the electric field vector, and $\boldsymbol{\mu}$ is the transition dipole operator. Defining $\boldsymbol{\varepsilon}$ to lie along the spaced-fixed Z-axis and assuming a random distribution of molecular orientations gives

$$S(J',\{\alpha'\};J,\{\alpha\}) = 3\sum_{M',M} |\langle J',M',\{\alpha'\}|\varepsilon\mu_Z|J,M,\{\alpha\}\rangle|^2. \qquad \text{(A2)}$$

μ_Z is the projection of $\boldsymbol{\mu}$ on the spaced-fixed Z-axis. In $HeCl_2$, $\boldsymbol{\mu}$ for the B-X transition lies along the vector $\mathbf{r}$ (the Cl-Cl axis). Using spherical tensor operator notation,[45] the Z-projection of $\boldsymbol{\mu}$ is given by

$$\mu_Z = |\boldsymbol{\mu}|\ (4\pi/3)^{1/2} \sum_{q=-1}^{1} D^{1*}_{0q}(\phi,\theta,0)\ Y_{1q}(\gamma,\chi)\ , \qquad \text{(A3)}$$

where the $D^{J}_{M\Omega}$ are the Wigner functions and the $Y_{j\Omega}$ are the spherical harmonics. The $|J,M,\{\alpha\}\rangle$ are formed as linear combinations of the basis set described in Sec. IV(B),

$$|J,M,\{\alpha\}\rangle = \sum_{\Omega\geq 0,\, j,\, n} a^{J,\{\alpha\}}_{\Omega pn}\Phi_n(R)\Theta^{JMp_i}_{j\Omega}(\hat{R},\hat{r}) \quad , \tag{A4}$$

where[33]

$$\Theta^{JMp_i}_{j\Omega}(\hat{R},\hat{r}) = \left[\frac{2J+1}{8\pi(1+\delta_{\Omega,0})}\right]^{1/2} \times \left[D^{J*}_{M\Omega}(\phi,\theta,0)Y_{j\Omega}(\gamma,\chi) + p_i(-1)^J\, D^{J*}_{M-\Omega}(\phi,\theta,0)Y_{j-\Omega}(\gamma,\chi)\right]. \tag{A5}$$

The same $\Phi_n(R)$ harmonic oscillator basis functions are used for both the X and the B electronic states. The $a^{J,\{\alpha\}}_{\Omega pn}$ are the elements of the eigenvectors obtained in the bound state calculation of Sec. IV(B).

We proceed by substituting Eqs. (A3) and (A5) into (A2). After considerable effort, using the properties of the Wigner functions and the spherical harmonics, it can be shown that

$$S(J',\{\alpha'\};J,\{\alpha\}) = |\mu|^2 \left[\frac{2J+1}{4}\right] (1-p_i p_i')^2$$
$$\times \Big| \sum_{n,n'} \delta_{n,n'} a'_{\Omega' p' n'} a_{\Omega p n} \sum_{j,j'} \langle j0,10|j'0\rangle \left[\frac{2j+1}{2j'+1}\right]^{1/2}$$
$$\times \sum_{\Omega\geq 0,\Omega'\geq 0} [(1+\delta_{\Omega,0})(1+\delta_{\Omega',0})]^{-1/2} \sum_q \Big[[\langle J\Omega,1q|J'\Omega'\rangle\langle j\Omega,1q|j'\Omega'\rangle$$
$$+ p_i(-1)^J \langle J-\Omega,1q|J'\Omega'\rangle\langle j-\Omega,1q|j'\Omega'\rangle]\Big] \Big|^2. \qquad \text{(A6)}$$

In Eqn. (A6) expressions such as $\langle m,j'm'|j''m''\rangle$ are Clebsh-Gordon coefficients and δ_{nm} are Kronecker deltas.

The line strength, S, determines the selection rules and the relative intensities of the allowed transitions between levels. The conditions for S to be non-zero give rise to selection rules for the optical transition. The factor $(1-p_i p_i')$ requires that $p_i = -p_i'$, or $\Delta p_i = \pm 2$. Non-zero Clebsh-Gordon coefficients involving J have $\Delta J = 0,\pm 1$. The factor $\langle j,0,10|j',0\rangle$ will couple only basis functions for which $j = j'\pm 1$. Since, as discussed in Sec. IV(B), the wavefunctions contain only even or odd j basis functions (parity $p_j = \pm 1$), we have the selection rule $\Delta p_j = \pm 2$.

Assuming that the rotational population of $HeCl_2$ (X) formed in the jet can be described as a Boltzmann distribution, the relative intensity of a line is given by

$$I(J',\{\alpha'\};J,\{\alpha\})$$
$$\approx \omega_1 \, S(J',\{\alpha'\};J,\{\alpha\})\cdot\exp[-E(J,\{\alpha\})/kT] \; . \qquad \text{(A7)}$$

Where ω_1 is the laser frequency, T is the rotational temperature, and k is the Boltzmann constant.

2. Technical Details of the Calculations

Bound-state calculations were performed using two different sets of basis functions. In the calculation of the $J = 0$ bound-state energy levels of Tables 5 and 6, more spherical harmonics were included in the angular basis set than in the $J > 0$ spectroscopy calculations such as that in Table 8. The computational aspects of this type of calculation are discussed in more detail in Ref. 33.

In the $J = 0$ calculations, the radial basis set consisted of the lowest 17 harmonic oscillator functions for an equilibrium position of $R_e = 4$ Å and a frequency of 16 cm^{-1}. Since $J = 0$, we must have $\Omega = 0$, so that only $\Omega = 0$ spherical harmonics are needed in the angular functions of Eq. (A5). The angular basis was formed by first prediagonalizing the angular part of the potential at $R = 4.0$ Å for the first 20 $\Omega = 0$ spherical harmonics. The 12 lowest energy angularly diagonalized functions were then used in the diagonalization of the full Hamiltonian.

Because of computer memory constraints, the $J > 0$ bound-state calculations to obtain the spectroscopy used a smaller number of spherical harmonics in the angular basis

set. In this case, angular basis functions with $|\Omega| \leq J$ must be included. The angular basis was formed by first prediagonalizing the angular part of the potential independently for each value of Ω, for the first 12 spherical harmonics. The 6 lowest energy $\Omega = 0$ functions and all $\Omega > 0$ functions with energies lower than the highest of these 6 were retained for the overall diagonalization of the full Hamiltonian. Energies are estimated to be converged to within a few thousandths of a wavenumber for rotational levels of the ground van der Waals vibrational level; the energies of excited van der Waals levels are less well converged.

In the $\Delta\upsilon = -1$ dynamics calculations, continuum eigenfunctions corresponding to dissociated states with j up to 28 were included. However, in the $\upsilon' = 12$ calculation in which 3 vibrational channels were included, only continuum states for j up to 18 were considered. It was observed that neglecting the minor vibrational channels in the calculation did not appreciably alter the $\Delta\upsilon = -1$ rotational distributions.

REFERENCES

[1] J.P. Simons, J. Phys. Chem. **88**, 1287 (1984).

[2] R. Bersohn, J. Phys. Chem. **88**, 5145 (1984).

[3] R. Shinke, *Collision Theory for Atoms and Molecules*, edited by F. Gianturco (Plenum, 1988).

[4] K.C. Janda, Adv. Chem. Phys. **60**, 201 (1985).

[5] J.I. Cline, N. Sivakumar, D.D. Evard, and K.C. Janda, Phys. Rev. A **36**, 1944 (1987).

[6] J.I. Cline, D.D. Evard, F. Thommen, and K.C. Janda, J. Chem. Phys. **84**, 1165 (1986); Chapter 2 of this thesis.

[7] D.D. Evard, F. Thommen, J.I. Cline, and K.C. Janda, J. Phys. Chem. **91**, 2508 (1987).

[8] D.E. Brinza, C.M. Western, D.D. Evard, F. Thommen, B.A. Swartz, and K.C. Janda, J. Phys. Chem. **88**, 2004 (1984).

[9] B.A. Swartz, D.E. Brinza, C.M. Western, and K.C. Janda, J. Phys. Chem. **88**, 6272 (1984).

[10] F. Thommen, D.D. Evard, and K.C. Janda, J. Chem. Phys. **82**, 5295 (1985).

[11] J.I. Cline, D.D. Evard, B.P. Reid, N. Sivakumar, F. Thommen, and K.C. Janda, in *Structure and Dynamics of Weakly Bound Molecular Complexes*, A. Weber, ed. (D. Reidel Publishing Co., Dordrecht, 1987), p. 533.

[12] L.J. van de Burgt, J.-P. Nicolai, and M.C. Heaven, J. Chem. Phys. **81**, 5514 (1984).

[13] R.E. Smalley, D.H. Levy, and L.Wharton, J. Chem. Phys. **64**, 3266 (1976).

[14] K.E. Johnson, L. Wharton, and D.H. Levy, J. Chem. Phys. **69**, 2719 (1978).

[15]W. Sharfin, K.E. Johnson, L. Wharton, and D.H. Levy, J. Chem. Phys. **71**,1292 (1979).

[16]J.A. Blazy, B.M. DeKoven, T.D. Russell, and D.H. Levy, J. Chem. Phys. **72**, 2439 (1980).

[17]K.E. Johnson, W. Sharfin, and D.H. Levy, J. Chem. Phys. **74**, 163 (1981).

[18]J.M. Skene, J.C. Drobits, and M.I. Lester, J. Chem. Phys. **85**, 2329 (1986).

[19]J.C. Drobits and M.I. Lester, J. Chem. Phys. **86**, 1662 (1987).

[20]S.J. Harris, S.E. Novick, and W. Klemperer, J. Chem. Phys. **61**, 192 (1974).

[21]S.E. Novick, S.J. Harris, K.C. Janda, and W. Klemperer, Can. J. Phys. **53**, 2007 (1975).

[22]J.A. Coxon, J. Mol. Spectrosc. **82**, 264 (1980).

[23]M.A.A. Clyne and E. Martinez, J.C.S. Faraday II **76**, 1275 (1980).

[24]T. Ishiwata, T. Shinzawa, T. Kusayanagi, and I. Tanaka, J. Chem. Phys. **82**, 1788 (1985).

[25]The symmetry properties of asymmetric tops are described in detail in W. Gordy and R.L. Cook, *Microwave Molecular Spectra* (Wiley, New York, 1970), p. 172.

[26]The symmetries of the $J_{k_a k_c}$ states are worked out in G. Herzberg, *Molecular Spectra and Molecular Structure* (van Nostrand Reinhold, New York, 1945), Vol. II, p. 50. In the case of $HeCl_2$, a $J_{k_a k_c}$ level is even (odd) when the sum k_a+k_c is even (odd).

[27]G. Herzberg, *Molecular Spectra and Molecular Structure* (van Nostrand Reinhold, New York, 1966), Vol. III, Chap.II3d.

[28]See, for example, J.I. Steinfeld, *Molecules and Radiation* (The MIT Press, Cambridge, Massachusetts, 1981), p. 23.

[29]M.A.A. Clyne and I.S. McDermid, J.C.S. Faraday II **74**, 1935 (1978).

[30]M.A.A. Clyne and I.S. McDermid, J.C.S. Faraday II **75**, 1677 (1979).

[31]See, for example, E.U. Condon and G.H. Shortley, *The Theory of Atomic Spectra* (Cambridge University Press, Cambridge, 1935), Chap. IV.

[32]See, for example, G. Herzberg, *Molecular Spectra and Molecular Structure* (van Nostrand Reinhold, New York, 1950), Vol. I, p. 208.

[33]B.P. Reid, K.C. Janda, and N. Halberstadt, J. Phys. Chem., in press.

[34]N. Halberstadt, J.A. Beswick, and K.C. Janda, J. Chem. Phys. **87**, 3966 (1987).

[35]M.J. O'Loughlin, Ph.D. Thesis, California Insititute of Technology, 1986.

[36]J.I. Cline, N. Sivakumar, D.D. Evard, and K.C. Janda, J. Chem. Phys. **86**, 1636 (1987).

[37]J.A. Beswick and J. Jortner, Adv. Chem. Phys. **47**, 363 (1981).

[38]G. Herzberg, *Molecular Spectra and Molecular Structure* (van Nostrand Reinhold, New York, 1945), Vol. II, p. 55.

[39]R.A. Aziz, P.W. Riley, U. Buck, G. Maneke, J. Schleusener, G. Scoles, and U. Valbusa, J. Chem. Phys. **71**, 2637 (1979).

[40]J.J. Valentini, D.P. Gerrity, D.L. Phillips, J.C. Nieh, and K.D. Tabor, J. Chem. Phys. **86**, 6745 (1987).

[41]G.E. Ewing, J. Phys. Chem. **91**, 4662 (1987).

[42] J.M. Hutson, C.J. Ashton, and R.J. LeRoy, J. Phys. Chem. **87**, 2713 (1983).

[43] R. Shinke, J. Chem. Phys. **85**, 5049 (1986).

[44] See, for example, R.W. Heather and J.C. Light, J. Chem. Phys. **78**, 5513 (1983).

[45] R.N. Zare, *Angular Momentum in Quantum Mechanics*, in press, Chap.VI.

Chapter 4

Product State Distributions for the Vibrational Predissociation of $NeCl_2$[†]

[†]Part of this work has been published as a communication in J. Chem. Phys. **86**, 1636 (1987).

I. INTRODUCTION

Levy and coworkers,[1] in their seminal experimental studies of rare-gas I_2 van der Waals molecules, established that the general features of the vibrational predissociation dynamics of these molecules can be explained in terms of relatively simple dynamical selection rules.[2] Lester, *et al.*[3-5] and this group[6-10] have recently used laser pump-probe techniques to the study of rare-gas ICl, Cl_2, and Br_2 complexes. This recent work has revealed that while the gross dynamical features of these molecules are similar to the I_2 complexes, detailed measurements of the product state distributions show a wide variety of effects such as preliminary intramolecular vibrational energy redistribution prior to decomposition[10,11] and the evidence for rotational rainbows[12] and interference structures[7,9] in the fragment rotational population distributions. Because of the relative simplicity of the potential energy surfaces of these molecules, they are ideal candidates for fundamental theoretical studies of molecular photofragmentation.[13]

In a previous communication[6] we reported preliminary results of measurements of the product-state distributions for the vibrational predissociation of $NeCl_2$. In this paper we present a full account of these laser pump-probe

measurements. In this technique, a pump laser pulse prepares $NeCl_2$ in a quasibound vibrational level of the long-lived B excited electronic state. The vibrational energy in the Cl-Cl stretching mode of the quasibound molecule is greatly in excess of the well depth of the $Ne\cdots Cl_2$ van der Waals potential. Coupling of the Cl-Cl stretch to the low frequency vibrational modes of the molecule associated with the $Ne\cdots Cl_2$ motion eventually leads to decomposition. The van der Waals well depth is so small that the transfer of even one vibrational quantum is sufficient to break the $Ne\cdots Cl_2$ bond. However, because of the large frequency mismatch between the covalent and van der Waals vibrational modes, this process is inefficient so that the vibrational predissociation rate is relatively slow.

The spectroscopy of the $B(\upsilon')\longleftarrow X(\upsilon'')$ transitions of $NeCl_2$ has been previously studied in detail.[14-16] Homogeneous linewidth measurements show that the vibrational predissociation lifetime in the B electronic state is a function of the number of Cl-Cl stretching vibrational quanta, υ', and ranges from 258±42 ps for $\upsilon' = 9$ to 33±2 ps for $\upsilon' = 13$. The lifetime of the B electronic state of Cl_2 is ~305 μs;[17] thus, the decomposition dynamics occurs on a single electronic potential energy surface. $NeCl_2$ has a T-shaped effective geometry. In the ground (X) electronic state the Ne atom

lies 3.57±0.04 Å from the Cl_2 center-of-mass.

Recently, we presented a comprehensive experimental and theoretical study of the vibrational predissociation dynamics of the closely related $HeCl_2$ system.[9] That work revealed that the decomposition of $HeCl_2$ is primarily a V⟶T process and is governed by a dynamical selection rule resulting from the symmetry of the van der Waals potential, which allows initial states of even or odd parity with respect to interchange of Cl atoms decay to only fragment states having the same parity. An unusual bimodal rotational population distribution was measured for the Cl_2 fragment, which terminated well below rotational energy levels forbidden by conservation of energy and angular momentum. As expected, $NeCl_2$ obeys the same symmetry selection rule as $HeCl_2$. The larger mass of the Ne atom leads to greater rotational excitation of the Cl_2 product; all fragment rotational states consistent with conservation of energy and angular momentum can be populated in the dissociation. The rotational distributions show bimodal structures similar to those observed in the decomposition of $HeCl_2$.

Perhaps the most surprising result of these studies is that, aside from symmetry and conservation of energy constraints, the observed rotational distributions are independent of the initially excited $NeCl_2$ vibrational level and thus are independent of the amount of energy

released to the product degrees of freedom. This result is quite different from what would be predicted by a simple, impulsive model of vibrational energy transfer.

II. EXPERIMENTAL

A. Pump-Probe Scheme

The scheme for preparing the initial, vibrationally excited quasibound $NeCl_2$ molecules and for detecting the Cl_2 fragment following decomposition is analogous to a technique we have described in detail elsewhere.[9] The scheme is outlined as follows:

$$NeCl_2(X,\upsilon''=0,J'') + \hbar\omega_1 \longrightarrow NeCl_2(B,\upsilon',J') \qquad \text{pump} \quad (1)$$

$$NeCl_2(B,\upsilon',J') \longrightarrow Ne + Cl_2(B,\upsilon'-z,j) \qquad \text{vibr. pred.} \quad (2)$$

$$Cl_2(B,\upsilon'-z,j) + \hbar\omega_2 \longrightarrow Cl_2(E,\upsilon,j\pm1) \qquad \text{probe} \quad (3)$$

$$Cl_2(E) \longrightarrow Cl_2(B) + \hbar\omega_{fluor} \ . \qquad \text{detection} \quad (4)$$

The X and B electronic states of $NeCl_2$ correlate to the $X^1\Sigma_g^+$ and $B^3\Pi(0_u^+)$ states[18] of uncomplexed Cl_2, respectively. In Eq. (1), a pump laser pulse prepares the initial, quasibound level of $NeCl_2(B)$. The pump laser frequency, ω_1, is positioned on the maximum of a $NeCl_2$ $B(\upsilon')\longleftarrow X(\upsilon''=0)$ band. Following decomposition in Eq. (2), a probe laser pulse excites the $Cl_2(B)$ fragment to the $E(0_g^+)$ state,[19] Eq. (3). Finally, the prompt fluorescence from $Cl_2(E)$ is detected as the experimental signal. By

tuning the probe laser frequency, ω_2, through the fragment Cl_2 E←B transition, the population distribution of the products is measured.

In the previous study of $HeCl_2$, it was possible to position ω_1 to cleanly prepare individual rotational levels of the initial quasibound vibrational state. The smaller rotational constants of $NeCl_2$ leads to spectral congestion in the B(υ')←X(υ''=0) bands that precludes positioning ω_1 on a single, isolated rotational line in the band. The measured fragment population distribution of the Cl_2(B) fragment thus represents an average over the set of initial rotational levels of $NeCl_2$(B,υ') prepared by the ω_1 pulse.

B. Apparatus

$NeCl_2$ van der Waals molecules were formed in a pulsed, free jet expansion of a mixture prepared by passing Ne and He in a 9:1 Ne:He ratio over liquid Cl_2 held at -77°C at pressures ranging from 150 to 450 psi, depending upon the pulsed nozzle source. Either a piezo-ceramic (Lasertechnics, 150 μm nozzle diameter) or a solenoid (General Valve, 300 μm nozzle diameter) type pulsed nozzle was used. The vacuum apparatus and pumping system,[14] optics, and laser setup[9,10] are described in detail elsewhere. Briefly, an excimer (Lambda Physik 201MSC) pumped dye laser (Lambda Physik 2002E) provided

tunable pump (ω_1) pulses, with a 0.2 cm^{-1} bandwidth over a wavelength range centered about 500 nm. An angle-tuned etalon was sometimes installed in this dye laser to attain 0.04 cm^{-1} resolution. A second dye laser (Lambda Physik 2002), pumped by the same excimer laser, was frequency doubled to provide 0.02 cm^{-1} probe (ω_2) pulses over a wavelength range centered about 250 nm. The ω_2 pulse followed the ω_1 pulse by ~10 ns; however, the temporal width of the pulses are significantly wider so that the two pulses are somewhat overlapped in time. The two laser pulses travelled collinearly through the vacuum apparatus. The intersection volume of the laser and nozzle pulses was defined by a lens and slits and imaged onto a photomultiplier detector. Optical filters were used to eliminate scattered ω_1 laser light and visible fluorescence. Photomultiplier pulses resulting from the UV fluorescence of $Cl_2(E)$ were preamplified and recorded by a gated integrator. A second gated integrator monitored the energy of the second harmonic of the probe dye laser pulse. Laser tuning, sychronization, and signal averaging were computer-controlled.

II. RESULTS

Fig. 1 shows the probe laser spectrum of the $^{35}Cl_2(B)$ fragment resulting from decomposition of

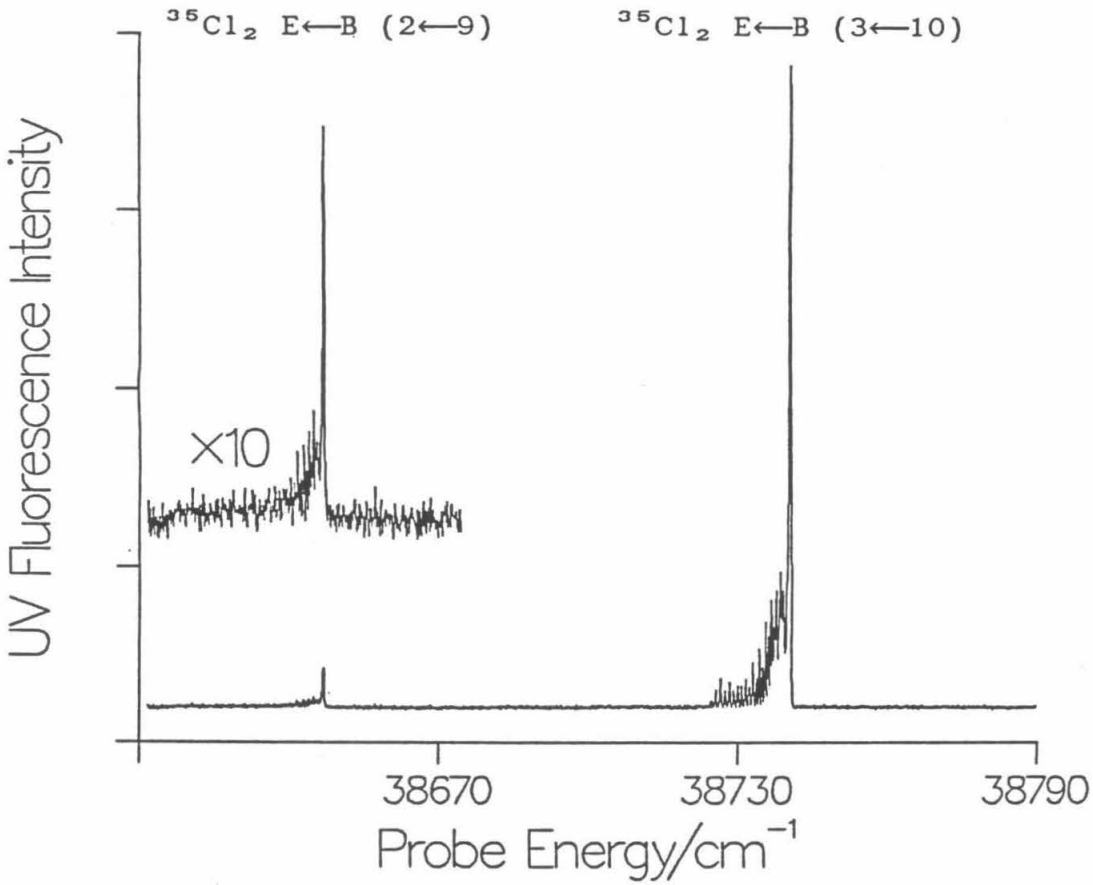

FIG. 1. Laser pump-probe spectrum obtained when ω_1 is tuned to the maximum intensity position on the $Ne^{35}Cl_2$ E←B (11←0) transition and ω_2 is scanned through the $^{35}Cl_2$ E←B 2←9 and 3←10 bands. The relative populations of the two vibrational channels are obtained from the integrated intensities of the two bands (after a small correction for the Franck-Condon factors).

$Ne^{35}Cl_2(B,\upsilon'=11)$ (υ' is the number of vibrational quanta in the Cl-Cl stretch and the complex has no excitation of the vibrational modes involving $Ne\cdots Cl_2$ motion). In Fig. 1, the pump frequency, ω_1, was positioned on the maximum of the $Ne^{35}Cl_2$ B←X, 11←0 band, and ω_2 was tuned through the $^{35}Cl_2$ E←B transition. Comparing the relative intensity of the feature due to the $^{35}Cl_2(B)$ fragment with 10 vibrational quanta remaining to that of the $^{35}Cl_2(B,\upsilon=9)$ fragment, it is apparent that the dominant decomposition mechanism for $NeCl_2$ is the loss of a single Cl_2 vibrational quantum (the $\Delta\upsilon = -1$ channel). There was no measurable signal for the $^{35}Cl_2(B,\upsilon=8)$ fragment: the population of the $\Delta\upsilon = -3$ channel is negligible. Using Eqn. (A1) of Chap. 5 to correct the integrated intensities of the fragment Cl_2 E←B, 3←10 and 2←9 bands for the Franck-Condon factors,[20] the $\Delta\upsilon = -2$ channel accounts for 6 % of the total population.

Figs. 2 and 3 show in detail the $^{35}Cl_2(B)$ fragment E←B, 3←10 and 2←9 bands, respectively, of Fig. 1. The rotational structure of these bands consists of R and P branches. The R branch forms a bandhead to the blue, whereas the P branch extends to the red so that the higher j rotational lines of the P branch are completely resolved. (j is the rotational quantum number of the fragment Cl_2.) Although most of the intensity in both spectra lies in the rotational lines resulting from Cl_2

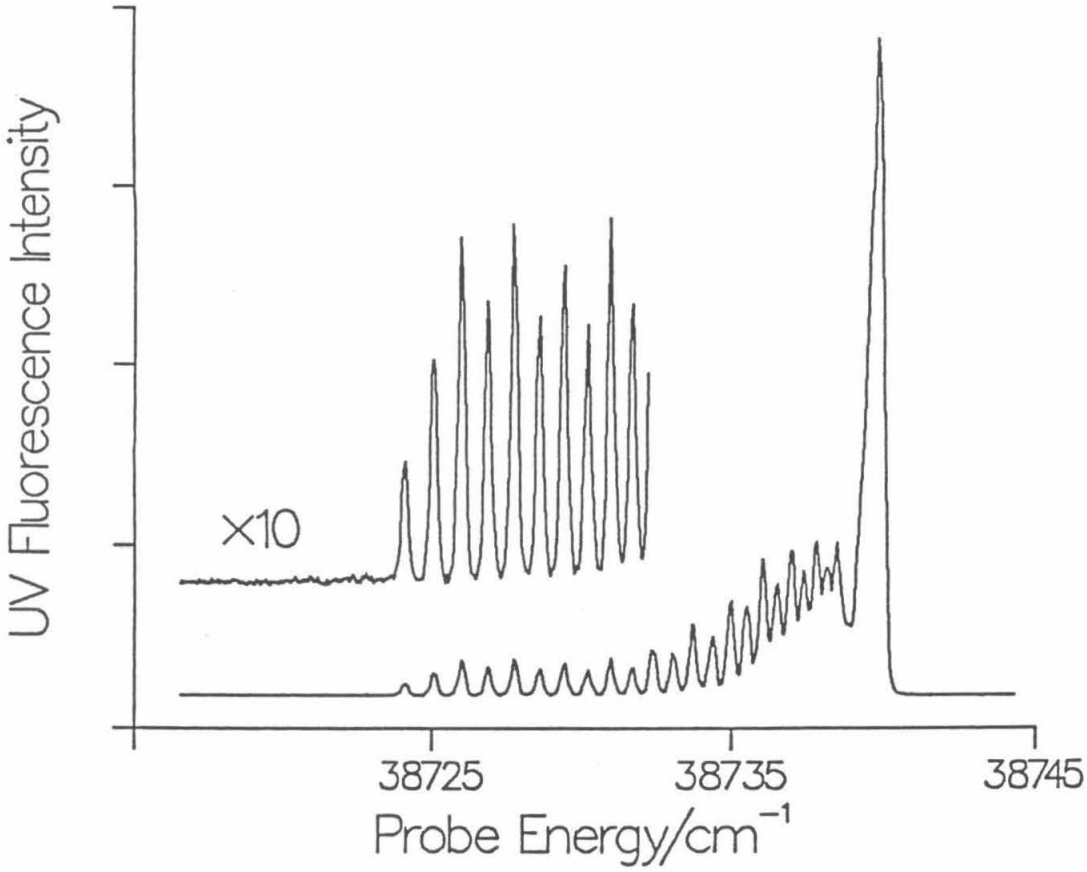

FIG. 2. Signal-averaged spectrum of the fragment $^{35}Cl_2$ E⟵B (3⟵10) band of Fig. 1 when ω_1 is positioned on the $Ne^{35}Cl_2$ B⟵X (11⟵0) band. The fragment rotational population distribution of the $\Delta\upsilon = -1$ channel is extracted from this spectrum.

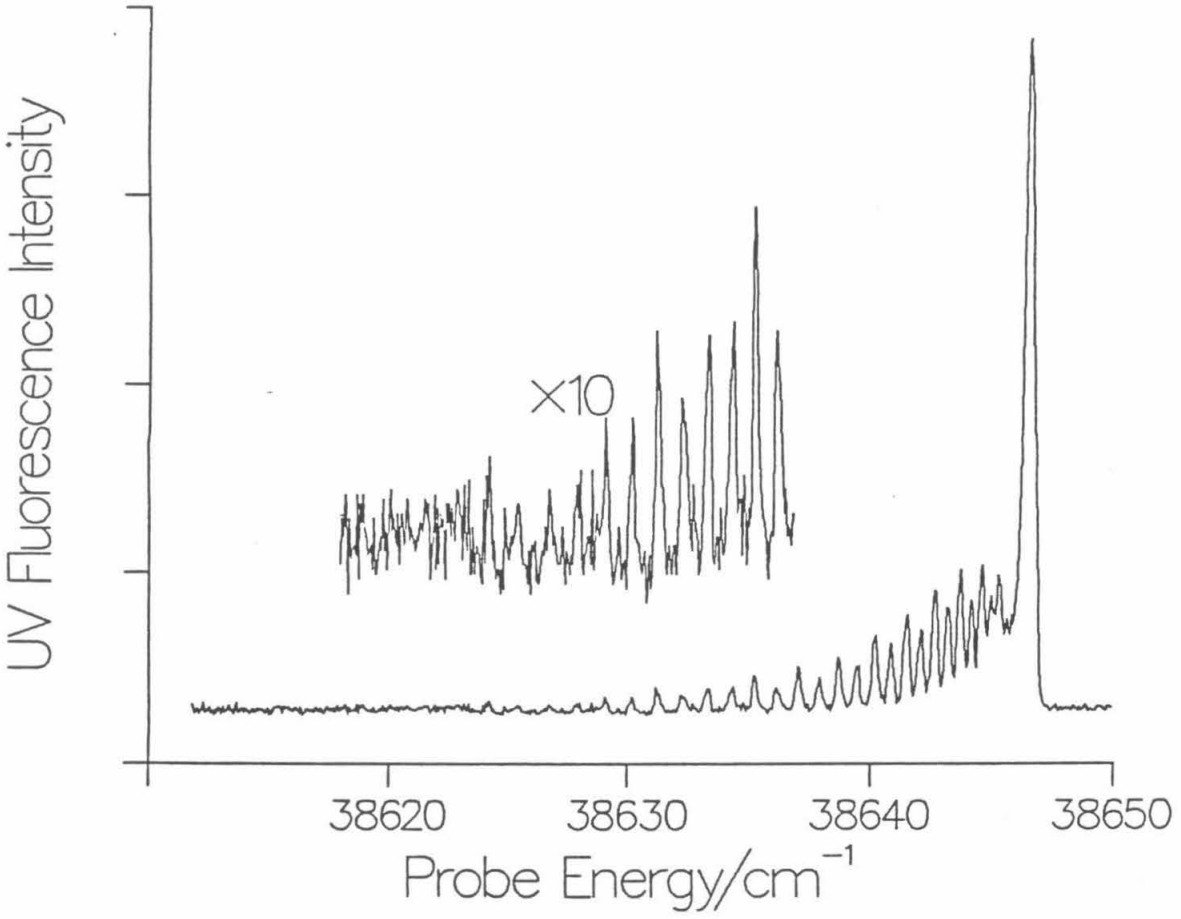

FIG. 3. Signal-averaged spectrum of the fragment $^{35}Cl_2$ E⟵B (2⟵9) band of Fig. 1 when ω_1 is positioned on the $Ne^{35}Cl_2$ B⟵X (11⟵0) band. The fragment rotational population distribution of the $\Delta v = -2$ channel is extracted from this spectrum.

fragments in the lower j rotational levels ($j \leq 12$), they differ dramatically in the intensities of the high j lines of the P branch. In Fig. 2 there is an abrupt termination of the P-branch between the P(24) and P(25) lines in the spectrum of the Cl_2 fragment in the $\Delta\upsilon = -1$ channel. In Fig. 3, however, the intensity of the P branch lines decreases gradually to unobservable levels around the P(30) line.

In Fig. 2 (the $\Delta\upsilon = -1$ channel), the abrupt termination of the P branch at $j = 24$ is the result of restrictions imposed by the conservation of energy; there is a limited amount of energy available in the Cl_2 vibrational quantum for rotational excitation of the products. In contrast, in Fig. 3 (the $\Delta\upsilon = -2$ channel), the gradual decline in the intensity of the high j lines of the P branch would appear to be the result of the kinematics of the decomposition; there still remains plenty of energy to populate yet higher rotational levels.

Cl_2 fragment spectra analogous to those in Figs. 2 and 3 were recorded for the decomposition of several initial quasibound levels of $NeCl_2(B,\upsilon')$. In each case, ω_1 was tuned to the maximum intensity position of the $NeCl_2$ $B \leftarrow X$, $\upsilon' \leftarrow 0$ band.

Fig. 4 shows fragment rotational state population distributions extracted from the line intensities in the

FIG. 4. $^{35}Cl_2(B,\upsilon'-z)$ fragment rotational population distributions for the vibrational predissociation of $Ne^{35}Cl_2(B,\upsilon')$. z is the number of Cl_2 vibrational quanta transferred in the dissociation. Since the parity of the initial level is conserved in the dynamics, the populations of the even j fragment levels (filled circles) and odd j levels (open circles) are each independently normalized to 100 %. (a) $\upsilon' = 6$, $z = 1$; (b) $\upsilon' = 7$, $z = 1$; (c) $\upsilon' = 8$, $z = 1$; (d) $\upsilon' = 9$, $z = 1$; (e) $\upsilon' = 11$, $z = 1$; (f) $\upsilon' = 11$, $z = 2$; (g) $\upsilon' = 12$, $z = 1$; (h) $\upsilon' = 13$, $z = 1$; (i) $\upsilon' = 13$, $z = 2$

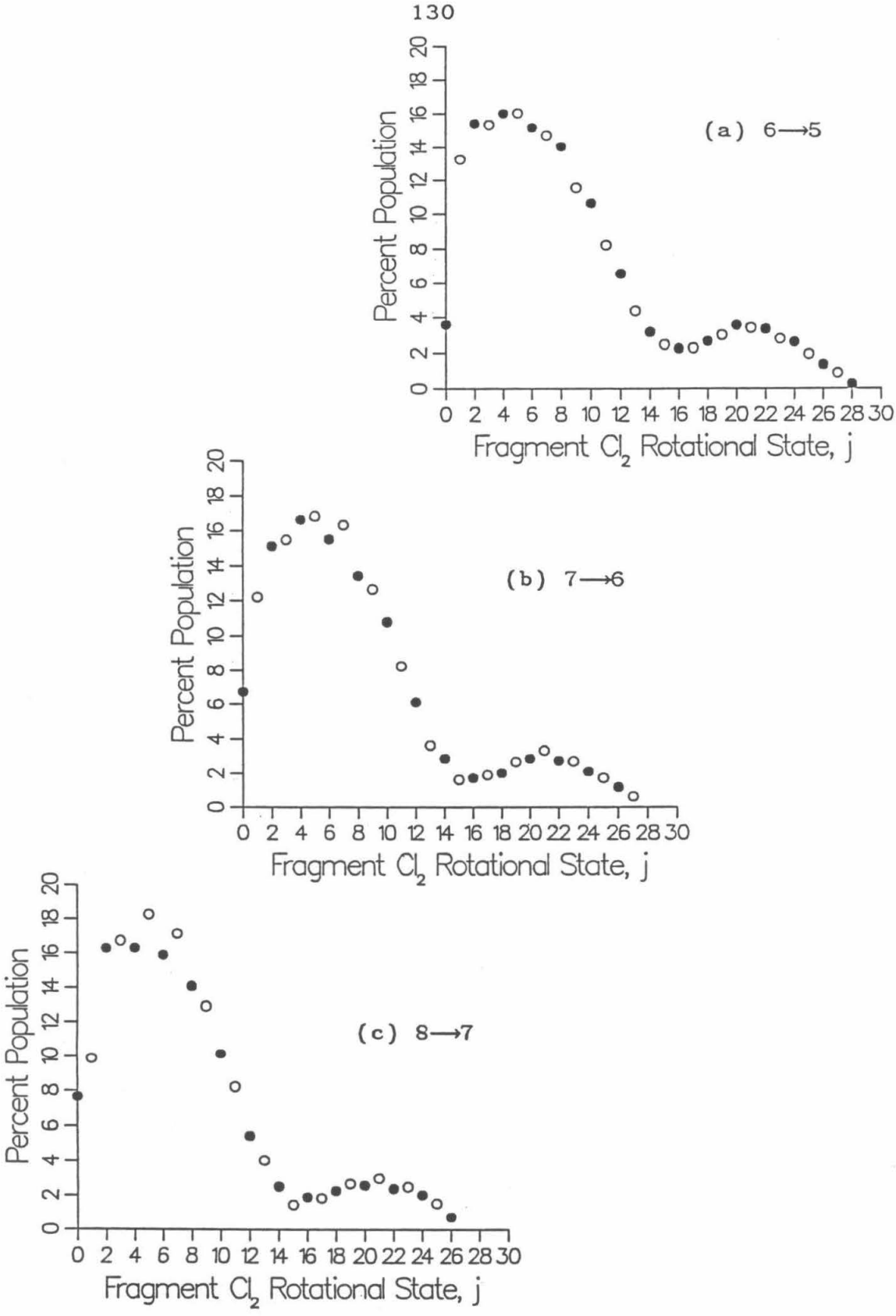
(a) 6⟶5
(b) 7⟶6
(c) 8⟶7
Percent Population
Fragment Cl_2 Rotational State, j
0 2 4 6 8 10 12 14 16 18 20
0 2 4 6 8 10 12 14 16 18 20 22 24 26 28 30

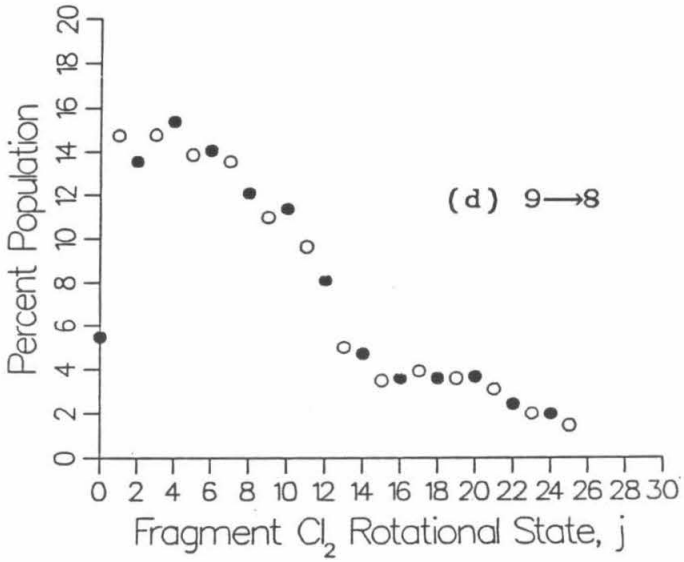
(d) 9⟶8
Percent Population
Fragment Cl_2 Rotational State, j

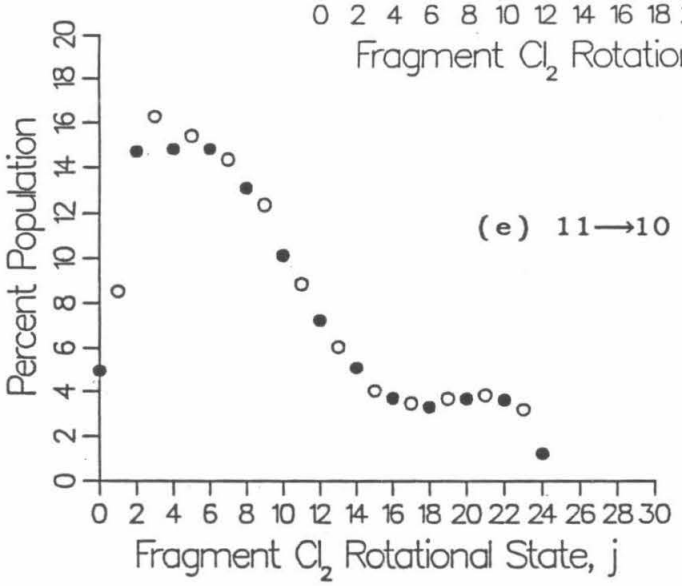
(e) 11⟶10
Percent Population
Fragment Cl_2 Rotational State, j

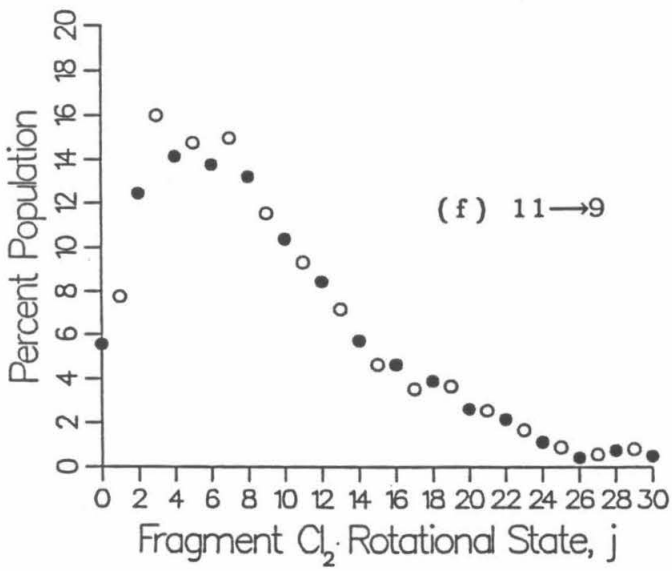
(f) 11⟶9
Percent Population
Fragment Cl_2 Rotational State, j

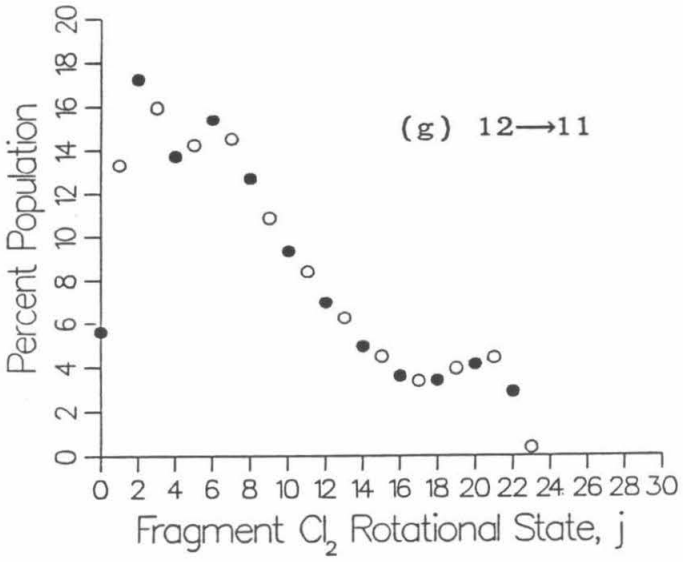
(g) 12⟶11
Percent Population
Fragment Cl_2 Rotational State, j

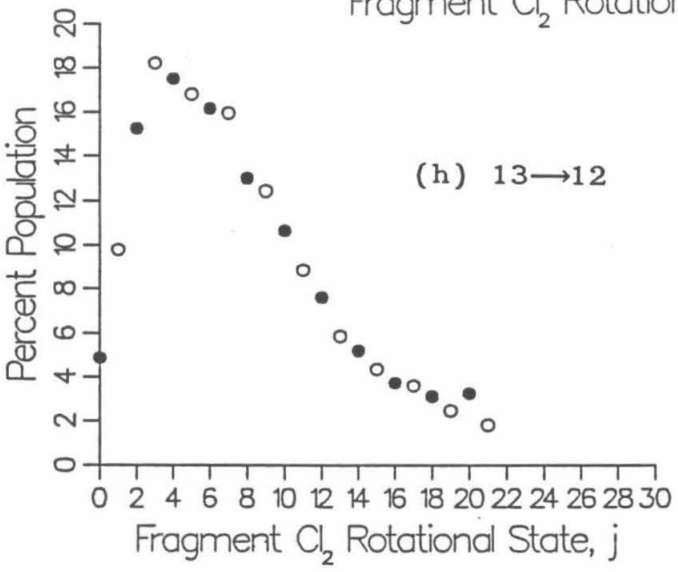
(h) 13⟶12
Percent Population
Fragment Cl_2 Rotational State, j

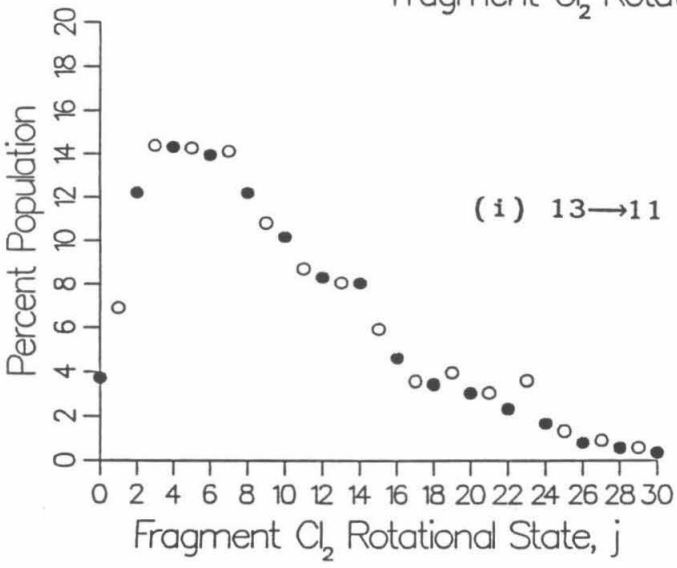
(i) 13⟶11
Percent Population
Fragment Cl_2 Rotational State, j

experimentally observed Cl_2 E←B spectra by computer simulation. The details of the simulation procedure are described elsewhere.[9] In the computer fitting, resolved, high *j*, P branch lines were individually fit prior to simulation of the congested bandhead region of the spectra. In this manner the intensities of the R branch lines that overlap the low *j* region of the P branch are accounted for while extracting the low *j* populations. The low *j* populations extracted from the spectra exhibit large variations for two reasons. First, the experimental uncertainty is larger for the low *j* populations as a result of the spectral congestion in the low *j* region of the probe laser spectrum, so the intensities of individual lines cannot be measured as accurately. Second, the low *j* populations are very sensitive to the specific initial rotational levels of the complex.[21] If the coriolis coupling can be neglected as is suggested by the theoretical study of $NeCl_2$ of Halberstadt, *et al*,[21] then $J > 0$ levels of the complex that have a *J*-projection onto the $Ne\text{-}Cl_2$ bond axis of Ω cannot decay to fragment rotational levels with $j < \Omega$. *J* is the total angular momentum of the initial quasibound level of $NeCl_2$. As a result, the low *j* distribution is sensitive to precisely where the pump laser is positioned on the $NeCl_2$ band contour.

In Fig. 4 the odd *j* and even *j* rotational

populations are independently normalized to 100 % because they undergo independent dynamics. In Refs. 7 and 9 we showed that initial rotational levels of $HeCl_2(B,\upsilon')$ can decay only to $Cl_2(B)$ fragment rotational levels having the same parity as the initial level, as a result of the symmetry of the $He\cdots Cl_2$ van der Waals potential. Precisely the same effect is observed for $NeCl_2$. The parity of the initially prepared quasibound level of $NeCl_2$ is given by the behavior of the rotational wavefunction upon exchange of the Cl atoms. The parity of the final $Cl_2(B)$ rotational wavefunction is even for *j* even and odd for *j* odd. Fig. 5 shows the E⟵B, 3⟵10 band of $^{35}Cl^{37}Cl$ when ω_1 is positioned on the maximum of the $Ne^{35}Cl^{37}Cl$ B⟵X, 11⟵0 band. The weak even/odd *j* intensity alternation observed in the resolved P branch is a result of the ω_1 frequency being positioned such that a larger number of molecules are prepared in even-parity initial rotational levels than odd-parity levels. It should be pointed out that for $Ne^{35}Cl^{37}Cl$ the dynamical parity conservation is not completely rigorous because the $^{35}Cl^{37}Cl$ center-of-mass does not lie precisely at the inversion center of the $Ne\cdots^{35}Cl^{37}Cl$ van der Waals potential. However, in the decomposition of $He^{35}Cl^{37}Cl$ (for which it is possible to prepare individual rotational levels of definite parity), there was no experimentally measurable violation of parity conservation and the same

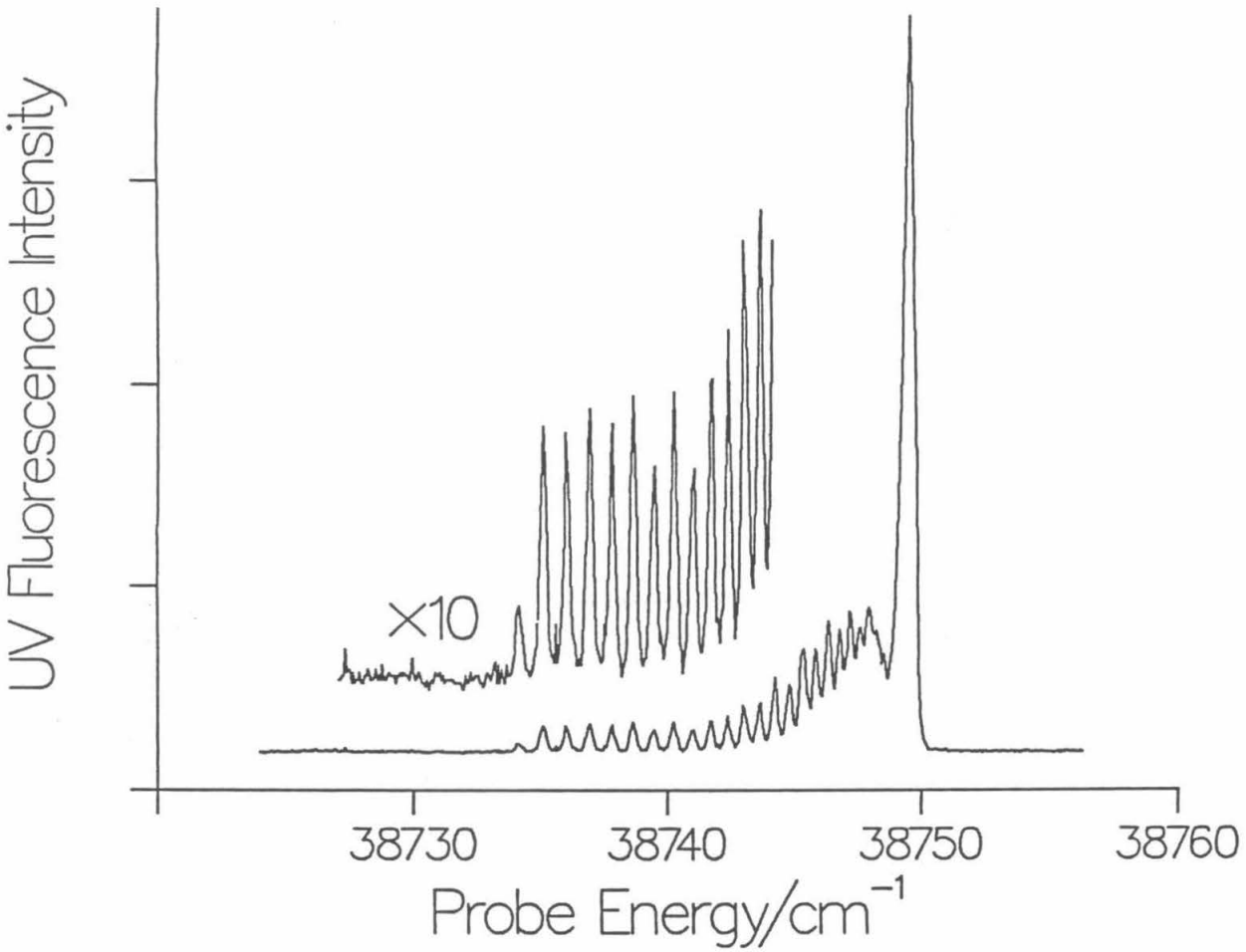

FIG. 5. Laser pump-probe spectrum of the fragment $^{35}Cl^{37}Cl$ E⟵B (3⟵10) band obtained when ω_1 is positioned on the maximum of the $Ne^{35}Cl^{37}Cl$ B⟵X (11⟵0) band. The weak even/odd alternation is a result of ω_1 preparing a larger fraction of even parity levels of $Ne^{35}Cl^{37}Cl$ than odd parity levels.

is likely to be true for $NeCl_2$.

The more dramatic even/odd *j* alternation in the $^{35}Cl_2$ E⟵B bands for the decomposition of $Ne^{35}Cl_2$ is the result of nuclear exchange symmetry. The $Ne^{35}Cl_2$ isotopic species exists in *ortho* and *para* forms that have a 3:5 degeneracy ratio. Since the vibrational predissociation should not change the nuclear spin state of ^{35}Cl, dynamical parity conservation is mandatory both as a *result of* the symmetry of the $Ne^{35}Cl_2$ van der Waals potential and nuclear exchange symmetry.

As a result of this symmetry phenomenon, it is possible to obtain B⟵X excitation spectra of $NeCl_2$, which consist of transitions to B state rotational levels of either even or odd parity. These parity-selected excitation spectra are recorded by positioning ω_2 to detect an individual rotational line in the P-branch of the fragment Cl_2 E⟵B transition and tuning ω_1 through the $NeCl_2$ B⟵X absorption. Spectra of this type are shown in Fig. 6. By adding the even- and odd-parity excitation spectra, the "normal" excitation spectrum previously obtained in one-laser LIF studies of $NeCl_2$ is recovered. Also shown in Fig. 6 are calculated asymmetric top rotational spectra for transitions to either even- or odd-parity levels. The structural parameters of Ref. 16 were used in the asymmetric top calculations.

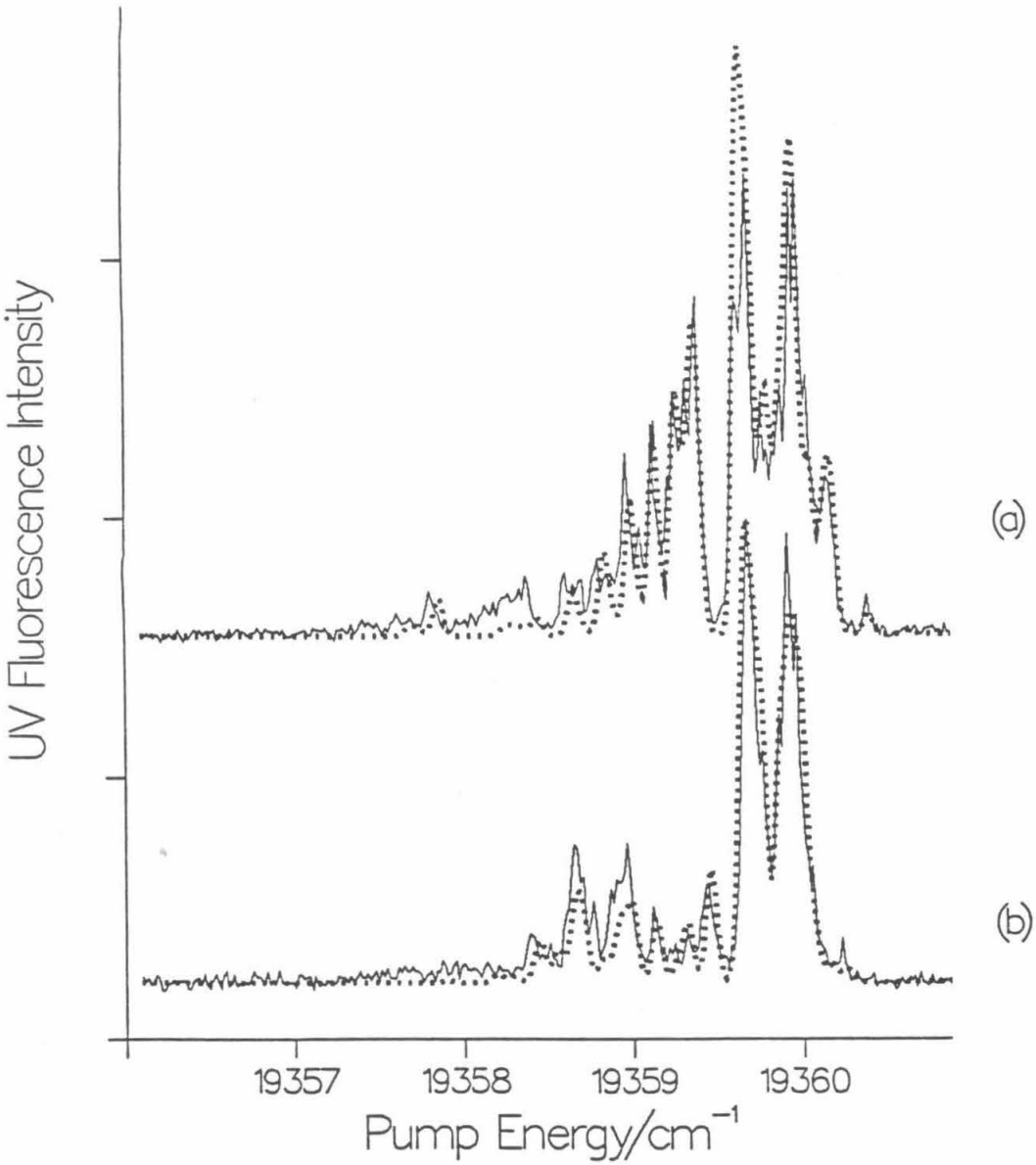

FIG. 6. Solid curves are parity selected excitation spectra of $Ne^{35}Cl_2$ obtained by scanning ω_1 through the $Ne^{35}Cl_2$ B←X (8←0) band and (a) positioning ω_2 on the P(20) line of the $^{35}Cl_2$ E←B (0←7) transition, or (b) positioning ω_2 on the P(19) line. Dotted curves are calculated asymmetric top spectra for transitions to only (a) even- or (b) odd- parity rotational states of $Ne^{35}Cl_2(B,\upsilon'=8)$. The rigid, T-shaped model has Ne to Cl_2 center-of-mass distances of 3.57 and 3.51 Å in the X and B electronic states, respectively. The computed lines are convoluted with the experimental lineshape, and the Boltzmann temperature is 1.0 K.

IV. DISCUSSION

The rotational distributions for the $\Delta v = -1$ decomposition channel of $NeCl_2(B, 9 \geq v' \geq 13)$ are abruptly terminated at a well-defined rotational level, j_{max}. In contrast, the rotational distributions for all $\Delta v = -2$ decomposition channels and the $\Delta v = -1$ channels for $v' \leq 8$ appear to decay gradually to zero. The abrupt termination at j_{max} for the $9 \leq v' \leq 13$ levels can be used to obtain the van der Waals bond energy in the B electronic state, $D_0(B)$.

We first consider the $\Delta v = -1$ channel of the rotationless, $J = 0$, level of $NeCl_2(B, v'=12)$. Assuming for the moment that the diagram in Fig. 7 accurately represents the energy of the initial $NeCl_2(B, v'=12, J=0)$ state and fragment $Cl_2(B, v=11)$ rotational levels, we see that it is not energetically possible to populate fragment $Cl_2(B, v=11, j)$ levels with $j > 24$. Imposing conservation of angular momentum still further decreases the maximum possible Cl_2 fragment rotational level. Since the total angular momentum, J, is zero, we must have $j = -l$, where j is the rotational angular momentum of the Cl_2 following fragmentation, and l is the orbital angular momentum of the recoiling fragments. Fig. 8 shows potential energy curves for the decomposition of $NeCl_2(B, v'=12, J=0)$ along the reaction coordinate, R, which is the distance between the Ne atom than the Cl_2 center-of-mass. The isotropic,

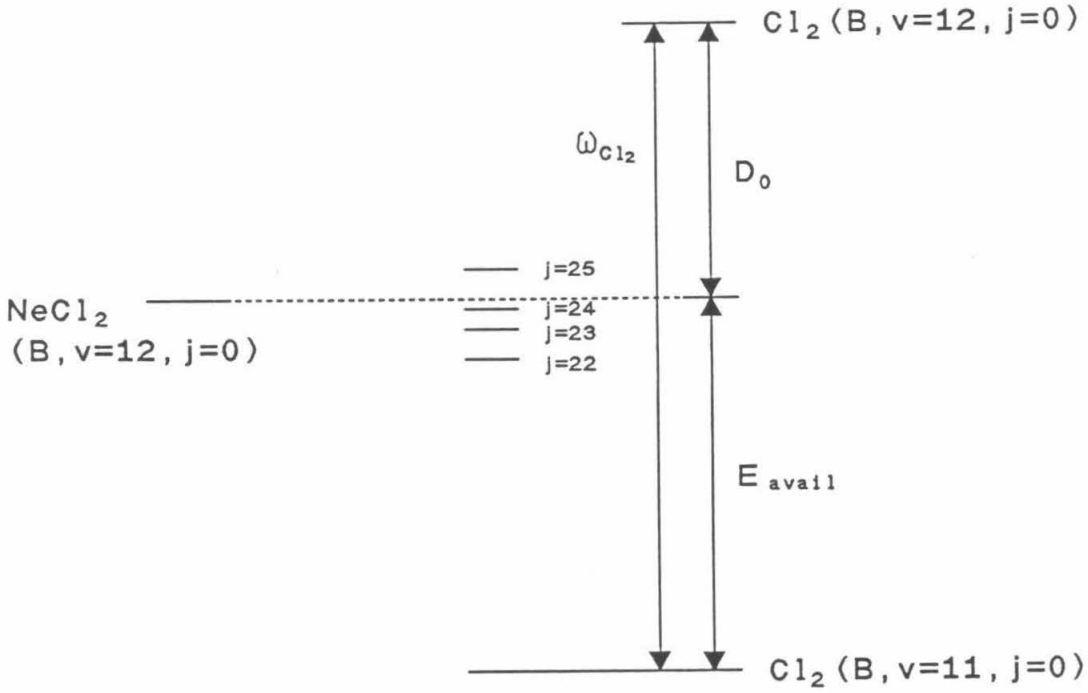

FIG. 7. This energy level diagram illustrates the energetic constraints in the decomposition of $NeCl_2(B,\upsilon'=12)$. The energy available for rotational and translational kinetic energy of the fragments is $E_{avail} = \omega(Cl_2) - D_0 = 77\ cm^{-1}$. $\omega(Cl_2)$ is the energy in the Cl_2 vibrational quantum ($131\ cm^{-1}$) and D_0 is the binding energy of $NeCl_2$ ($54\ cm^{-1}$). Only rotational levels of $Cl_2(B,\upsilon=11)$ with $j \lesssim 24$ can be populated energetically; conservation of angular momentum imposes further constraints as described in the text.

FIG. 8. Schematic diagram illustrating the effect of the centrifugal barrier in the vibrational predissociation of $NeCl_2(B, v'=12)$. The centrifugal barriers in the effective radial potentials for fragment levels with $j > 22$ lie above the energy of the prepared state. This prevents population of the $j = 23$ and 24 fragment levels, even though they are energetically allowed, as shown in Fig. 7.

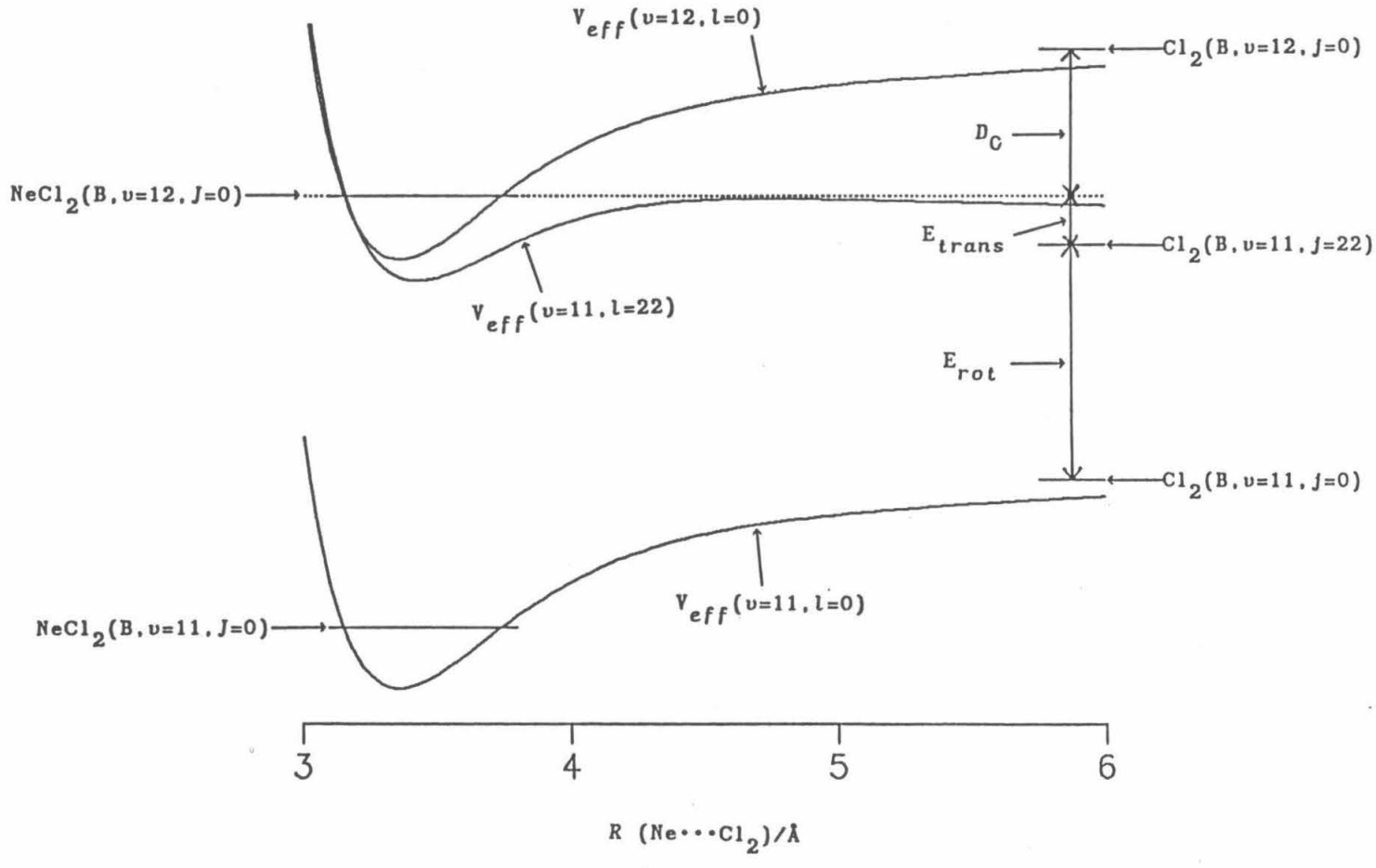
$V_{eff}(v=12, l=0)$
$Cl_2(B, v=12, J=0)$
D_C
$NeCl_2(B, v=12, J=0)$
E_{trans}
$Cl_2(B, v=11, J=22)$
$V_{eff}(v=11, l=22)$
E_{rot}
$Cl_2(B, v=11, J=0)$
$V_{eff}(v=11, l=0)$
$NeCl_2(B, v=11, J=0)$
3
4
5
6
R (Ne···Cl_2)/Å

long-range part of the $NeCl_2$ potential is given by[22]

$$V(R) = -\frac{C_6}{R^6} \quad , \tag{5}$$

where C_6 has the value 1.33×10^5 $cm^{-1}\cdot Å^6$. Addition of the centrifugal potential due to the orbital angular momentum gives the effective potential along the reaction coordinate,

$$V_{eff}(R,l) = -\frac{C_6}{R^6} + \frac{l(l+1)\hbar^2}{2\mu R^2} \quad , \tag{6}$$

where μ is the reduced mass given by $m_{Ne}m_{Cl_2}/(m_{Ne}+m_{Cl_2})$. The height of the centrifugal barrier is then

$$V_{barrier}(l) = (54\ C_6)^{-½} \left[\frac{l(l+1)\hbar^2}{2\mu R^2}\right]^{\frac{3}{2}} \quad . \tag{7}$$

It can be seen in Fig. 8 that the presence of the centrifugal barrier prevents population of the highest energetically allowed energy levels. Upper and lower limits on the value of $D_0(B)$ can now be obtained from the experimental determination of j_{max} and the known energy of the Cl_2 vibrational quantum given by $\omega(12) = E[Cl_2(B,\upsilon=12,j=0)] - E[Cl_2(B,\upsilon=11,j=0)]$. $D_0(B)$ is bracketed by

$$\omega(12) - E_{rot}(\upsilon=11, j_{max}+1) - V_{barrier}(j_{max}+1)$$
$$\leq D_0(B) \leq \omega(12) - E_{rot}(B, \upsilon=11, j_{max}) - V_{barrier}(j_{max}). \quad (8)$$

$E_{rot}(\upsilon, j)$ is the rotational energy of the $Cl_2(B, \upsilon, j)$ fragment, given by $B_v j(j+1) - D_\upsilon j^2(j+1)^2$, where B_υ and D_υ are the spectroscopic rotational and distortion constants for $Cl_2(B)$.[18] Table 1 shows the results of these calculations. By considering the range of $D_0(B)$ obtained in the analysis of several rotational bands, $D_0(B)$ is bracketed to lie between 52.0 and 56.0 cm^{-1}.

In Table 1 note that for the $\upsilon' = 11$ state, j_{max} was chosen as 23, even though $j = 24$ was observed experimentally. In Fig. 2 it can be seen that the population of $j = 24$ is substantially less than $j = 23$, as if the $j = 24$ channel were only partly open. This behavior has also been observed in $ArCl_2$[10,11] and is a result of the fact that the observed rotational distribution includes contributions from initial rotational levels of the complex with $J > 0$. Some of the higher J rotational levels of $NeCl_2(B, \upsilon'=11)$ have energy such that they lie just above the threshold for production of the $Cl_2(B, \upsilon=10, j=24)$ fragment, whereas lower J levels of the complex lie below the threshold and can decay to fragments only with $j < 24$. Since the rotational temperature of the jet is 1.0 K (measured in the fits of

Table 1:

Bracketing of the binding energy of $NeCl_2$ by the j_{max} threshold in the decomposition of $NeCl_2(B, 9 \leq v' \leq 11)$.

v'	j_{max}	$\omega(v')/cm^{-1}$	$D_0(B)/cm^{-1}$
13	21	120.29	49.5 - 56.0
12	22	131.02	51.0 - 58.0
11	23	141.89	51.9 - 59.5
9	25	163.77	52.0 - 60.6

$52.0 \leq D_0(B) \leq 56.0\ cm^{-1}$

$57.7 \leq D_0(X) \leq 61.7\ cm^{-1}$

Fig. 6), there is little population of initial J levels lying more than 2 cm^{-1} above the $J = 0$ level of the complex. This suggests that the actual value of $D_0(B)$ lies closer to the lower bound of the 52.0-56.0 cm^{-1} range. This range for $D_0(B)$ is revised from the estimate in our earlier preliminary communication[6] in which we chose $j_{max} = 24$ for the dissociation of the $\upsilon' = 11$ state of $NeCl_2(B)$.

The $NeCl_2$ B←X, υ'←0 bands are blue-shifted from the associated Cl_2 B←X, υ'←0 bands. This means that the binding energy in the ground electronic state is larger than in the B electronic state. By adding the observed average blue shift of 5.66 cm^{-1} for the 9 through 13 bands[14] to $D_0(B)$, we have $57.7 \leq D_0(X) \leq 61.7$ cm^{-1}. Both the anisotropy and short-range parts of the actual potential are neglected in this calculation, and the isotropic long-range part of the van der Waals potential of $NeCl_2(B)$ was assumed to be the same as for $NeCl_2(X)$. For this reason the binding energy determined in this manner should be considered as only an approximate measurement. This estimate of the binding energy for $NeCl_2$ is somewhat smaller than the measured binding energies of $NeBr_2$[23] and NeI_2,[24] which have values of $D_0(X)$ between 68.5-72.6 cm^{-1} and 72.4-74.7 cm^{-1}, respectively.

The maximum classical impact parameter, b, for the photodissociation half-collision is given by

$b \cong \hbar[j_{max}(j_{max}+1)]^{1/2}/\mu u$, where u is the relative velocity of the fragments at large R. The value of u is obtained from the translational kinetic energy of the fragments, given by $E_{trans} = \omega(\upsilon') - E_{rot}(j_{max}) - D_0$. Assuming $D_0(B) = 54\ cm^{-1}$, the observation of $j_{max} = 22$ in the dissociation of $NeCl_2(B,\upsilon'=12)$ gives a maximum classical impact parameter of 6.4 Å, much larger than the molecular dimensions of $NeCl_2$.

The rotational distributions in Fig. 4 are independent of the initial vibrational level, υ', of the complex for $\upsilon' \leq 8$. j_{max} for these levels appears to be determined by constraints other than conservation of energy, which prematurely terminates the rotational distributions for $\upsilon' > 8$. These constraints do not appear to be simply kinematic in nature; in a simple, impulsive, classical picture for the dissociation, one would expect more rotational excitation of the fragments in the $\Delta\upsilon = -2$ channel than in the $\Delta\upsilon = -1$ channel because of the much larger amount of energy in the half-collision. No population of rotational levels with $j > 30$ was observed, regardless of the energy of the half-collision.

Tables 2 and 3 present a summary of the analysis of the Cl_2 fragment rotational distributions for all the experimentally measured spectra. The average energy appearing in rotation, $\langle E_{rot} \rangle$, for the $\Delta\upsilon = -2$ distributions is not significantly different than that for

Table 2:

Summary of the fragment rotational state population distributions of the $\Delta\upsilon = -1$ channel for decomposition of $NeCl_2$ (B,υ'). E_{avail} is calculated assuming $D_0(B) = 54\ cm^{-1}$.

Prepared $Ne^{35}Cl_2$ (B) state: υ'

	υ' parity													
	6		7		8		9		11		12		13	
	+	−	+	−	+	−	+	−	+	−	+	−	+	−
$\frac{\langle E_{rot}\rangle}{cm^{-1}}$	18.0	17.5	15.5	16.1	13.9	14.6	15.9	15.7	14.9	15.4	13.2	13.2	10.8	10.8
$\frac{E(j_{max})}{cm^{-1}}$	120.2	112.0	101.7	109.5	99.3	92.0	82.8	89.7	78.2	71.9	63.8	69.6	51.1	56.3
$\frac{E_{avail}}{cm^{-1}}$	142.1		131.5		120.7		109.76		87.8		77.2		66.3	
Probe Trns $v(E)\leftarrow v(B)$	0←5		0←6		0←7		2←9		3←11		4←12		5←12	

Table 3:

Summary of the fragment rotational state population distributions of the $\Delta v = -2$ channel for decomposition of $NeCl_2$ (B,v'). E_{avail} is calculated assuming $D_0(B) = 54\ cm^{-1}$.

Prepared $Ne^{35}Cl_2$ (B) state: v'

	v' parity			
	11		13	
	+	−	+	−
$\langle E_{rot} \rangle / cm^{-1}$	16.7	16.8	16.6	16.6
$E(j_{max}) / cm^{-1}$	124.8	116.7	117.3	109.8
E_{avail} / cm^{-1}	240.6		197.3	
Probe Trans. v(E)←v(B)	2←9		4←11	

the $v' \leq 8$, $\Delta v = -1$ distributions, despite the large change in E_{avail}.

The $\Delta v = -1$ rotational distributions are distinctly bimodal for $v' \leq 8$. For $v' > 8$, the second maximum at $j = 20$ and 21 is apparently obscured by the energetic termination of the rotational distributions. The bimodal rotational distribution is similar to one observed in the vibrational predissociation of $HeCl_2$. However, in $HeCl_2$ the $\Delta v = -2$ distribution is also bimodal, whereas for $NeCl_2$ the $\Delta v = -2$ rotational population decreases monotonically with j.

Apparently, the kinematic limit for rotational excitation in the dissociation of $NeCl_2$ is $j = 30$, while that for $HeCl_2$ is $j = 14$. Assuming that the maximal impact parameters (the origin of the kinematic constraint) for the He- and Ne-Cl_2 half-collisions are similar, then the classical relation $|l| = \mu ub = b(2\mu E_{avail})^{1/2}$ correctly predicts that the ratio of the rotational excitation limits $(|l(Ne)|/|l(He)| = [30(30+1)/14(14+1)]^{1/2} = 2.1)$ should be given by the square root of the ratio of the reduced masses $([\mu(Ne)/\mu(He)]^{1/2} = 2.0)$, provided the collision energies, E_{avail}, are the same. However, as mentioned above, this very simple picture does not account correctly for the insensitivity of the rotational excitation to E_{avail}.

Halberstadt, *et al.*[21] have performed 3-dimensional

quantum mechanical calculations on a model potential surface for $NeCl_2(B,v'=11)$ and obtained product rotational distributions using the golden rule approximation. The calculated distributions showed significantly less rotational excitation than is observed experimentally, and there was no evidence for a second peak in the distribution. This is probably due to deficiencies in the potential surface used.

An analogous calculation for $HeCl_2$ on a potential surface optimized to reproduce experimental data gave good agreement with the experimental bimodal rotational distribution, and a refined potential surface for $NeCl_2$ should bring the full quantum calculation into agreement with experiment. However, it was not possible in the $HeCl_2$ study to draw a simple physical picture to explain the origin of this phenomenon. The results of such a large basis set diagonalization calculation are difficult to interpret. The dynamics of $NeCl_2$, like that of $HeCl_2$, is not easily rationalized in terms of a simple model. Here we explore some possible approaches to the future further analysis of this data.

Hutson, *et al.*[25] performed close-coupled calculations for the vibrational predissociation of ArHD that predicted a bimodal distribution of the HD fragment. They speculated that the bimodal distribution originates from oscillatory structure associated with a rotational

rainbow singularity in the classical rotational distribution. Interference patterns arise because of the superposition of trajectories originating from different initial angular configurations of the molecule that give rise to the same final rotational level of the products. The position of the minimum and second peak of our distribution appears to be independent of the available energy, whereas the position of the classical rainbow feature would be expected to scale with approximately the square root of E_{avail}.[26] The rotational rainbow phenomenon has been used successfully to model rotational distributions for a variety of photodissociations[27]. One particularly relevant result is that of Sato, *et al.*,[28] who reported an unusual, "inverted" rotational distribution of NO fragments from the direct photodissociation (not vibrational predissociation) of the Ne- and Ar-NO van der Waals molecules. In that study, the position of the maximum in the rotational distribution was found to be proportional to the both square root of the half-collision energy and the square root of the reduced mass, compelling evidence for the presence of the rotational rainbow effect. Because of the insensitivity of the rotational distribution of $NeCl_2$ to E_{avail}, it is not possible to identify the rotational distributions for vibrational predissociation with quantum interference patterns associated with a rotational rainbow.

Another method for predicting rotational distributions for the photodissociation of triatomics molecules is the Franck-Condon or sudden approximation.[21] In this picture the bending wavefunction of the initial state is decomposed in terms of a free rotor basis set. In its simplest form, the Franck-Condon model predicts that the population of a given fragment rotational level is given by the weighting of that rotor basis function in the initial bending wavefunction. Thus, this model predicts that the rotational distribution is independent of the available energy for the products, in agreement with the experimental results for $NeCl_2$. It may be that a more sophisticated application of the Franck-Condon model[29] to $NeCl_2$ would be successful in describing the observed distributions; such work is beyond the scope of the present paper.

In conclusion, rotational and vibrational product-state distributions are measured in this work for the Cl_2 fragment of the vibrational predissociation of $NeCl_2$ from several initial quasibound levels. The dominant vibrational channel for the dissociation is the transfer of one Cl-Cl vibrational quantum to the van der Waals modes. The rotational distributions are, in some cases, abruptly terminated because of energy conservation constraints. In these cases, the measured thresholds for production of the highest allowed rotational level are

used to estimate the binding energy of $NeCl_2(X)$ to lie between 57.7 and 61.7 cm^{-1}. For dissociation from initial states for which energy constraints do not affect the dynamics, the rotational distributions extend to a maximum j of about 30, regardless of the available energy for translational and rotational excitation of the recoiling fragments. Rotational distributions for the $\Delta\upsilon = -1$ channel are bimodal. It seems impossible to rationalize the observed distributions in terms of a simple physical model for the decomposition; it is clear that further theoretical work is required to understand the dynamics of this molecule.

V. ACKNOWLEDGEMENTS

We thank Nadine Halberstadt for helpful discussions and gratefully acknowledge the National Science Foundation for the financial support of this research.

REFERENCES

[1]D.H. Levy, Adv. Chem. Phys. **47**, 323 (1981).

[2]G.E. Ewing, J. Phys. Chem. **91**, 4662 (1987).

[3]J.C. Drobits, J.M. Skene, and M.I. Lester, J. Chem. Phys. **84**, 2896 (1986).

[4]J.M. Skene, J.C. Drobits, and M.I. Lester, J. Chem. Phys. **85**, 2329 (1986).

[5]J.C. Drobits and M.I. Lester, J. Chem. Phys. **74**, 163 (1981).

[6]J.I. Cline, N. Sivakumar, D.D. Evard, and K.C. Janda, J. Chem. Phys. **86**, 1636 (1987).

[7]J.I. Cline, N. Sivakumar, D.D. Evard, and K.C. Janda, Phys. Rev. A **36**, 1944 (1987).

[8]N. Sivakumar, D.D. Evard, J.I. Cline, and K.C. Janda, Chem. Phys. Lett. **137**, 403 (1987).

[9]J.I. Cline, B.P. Reid, D.D. Evard, N. Sivakumar, N. Halberstadt, and K.C. Janda, manuscript in preparation; Chap. 3 of this thesis.

[10]D.D. Evard, Ph.D. Thesis, California Institute of Technology, 1988.

[11]D.D. Evard, J.I. Cline, and K.C. Janda, manuscript in preparation.

[12]J.C. Drobits, J.M. Skene, and M.I. Lester, poster presentation at the 1987 Conference on the Dynamics of Molecular Collisions, July, 1987, Wheeling, WV.

[13]N. Halberstadt and J.A. Beswick, Faraday Discuss. Chem. Soc. **73**, 357 (1982).

[14]D.E. Brinza, C.M. Western, D.D. Evard, F. Thommen, B.A. Swartz, and K.C. Janda, J. Phys. Chem. **88**, 2004 (1984).

[15]D.D. Evard, F. Thommen, and K.C. Janda, J. Chem. Phys. **84**, 3630 (1986).

[16]D.D. Evard, F. Thommen, J.I. Cline, and K.C. Janda, J. Phys. Chem. **91**, 2508 (1987).

[17]M.A.A. Clyne and E. Martinez, J.C.S. Faraday II **76**, 1275 (1980).

[18]J.A. Coxon, J. Mol. Spectrosc. **82**, 264 (1980).

[19]T. Ishiwata, T. Shinzawa, T. Kusayanagi, and I. Tanaka, J. Chem. Phys. **82**, 1788 (1985).

[20]Franck-Condon factors for the E⟵B transition of $^{35}Cl_2$ were calculated using the RKR potentials of Refs. 18 and 19.

[21]N. Halberstadt, J.A. Beswick, and K.C. Janda, J. Chem. Phys. **87**, 3966 (1987).

[22]M.J. O'Loughlin, Ph.D. Thesis, California Institute of Technology, 1986.

[23]J.I. Cline, D.D. Evard, B.P. Reid, N. Sivakumar, F. Thommen, and K.C. Janda, in *Structure and Dynamics of Weakly Bound Molecular Complexes*, A. Weber, ed. (D. Reidel Publishing Co., Dordrecht, 1987), p. 533.

[24]J.A. Blazy, B.M. DeKoven, T.D. Russell, and D.H. Levy, J. Chem. Phys. **72**, 2439 (1980).

[25]J.M. Hutson, C.J. Ashton, and R.J. LeRoy, J. Phys. Chem. **87**, 2713 (1983).

[26]R. Shinke and V. Engel, J. Chem. Phys. **83**, 5068 (1985).

[27]R. Shinke, J. Chem. Phys. **85**, 5049 (1986).

[28]K. Sato, Y. Achiba, H. Nakamura, and K. Kimura, J. Chem. Phys. **85**, 1418 (1986).

[29] R.W. Heather and J.C. Light, J. Chem. Phys. **78**, 5513 (1983).

Chapter 5

Vibrational Predissociation Dynamics of the $Ne\cdots Br_2$ van der Waals Molecule[†]

[†]This work was published in a slightly different form in *Structure and Dynamics of Weakly Bound Molecular Complexes*, A. Weber, ed. (D. Reidel Publishing Co., Dordrecht, 1987), p. 533.

I. INTRODUCTION

Levy and coworkers initiated the study of the molecular dynamics of the rare-gas halogen complexes with their work on the vibrational predissociation of HeI_2, NeI_2, and ArI_2 in the B electronic excited state.[1] The HeI_2 results have received a great deal of attention because theory for that molecule is relatively easy to perform.[2] It was found that vibrational predissociation of HeI_2, for vibrational levels up to $\upsilon' = 27$, is dominated by the $\Delta\upsilon = -1$ vibrational channel, and that the vibrational predissociation lifetime of the complex ranged from 221 ps for $\upsilon' = 12$ to 38 ps for $\upsilon' = 27$. The mechanism of this decomposition has been interpreted as a nearly pure V-T type process and the dependence of the decomposition rate upon the number of vibrational quanta initially in the I-I stretch in terms of a energy gap[2] or momentum gap[3,4] model. An early indication that the energy-gap law is at least qualitatively accurate over a very large range of vibrational predissociation rates was the observation of quasibound vibrational levels ($\tau > 10^{-5}$ s) for the ground electronic state of $NeCl_2$.[5]

The V-T mechanism for vibrational predissociation of HeI_2 and NeI_2 was supported by dispersed fluorescence experiments, which revealed the product I_2 molecules to be rotationally cold. For ArI_2 there is considerable

rotational energy in the products.[1] This may be due to the ability of ArI_2 to dissociate via a $\Delta v = -3$ sequential mechanism, allowing the first two quanta of energy released from the I_2 stretch to be randomized over the van der Waals modes before the third quantum dissociates the molecule.

In this experiment we show that the vibrational predissociation dynamics of $NeBr_2$ is primarily a V-T process, not too different from what one might have expected on the basis of the HeI_2 and NeI_2 results. However, measurements of vibrational predissociation dynamics for related rare-gas halogen systems have indicated that in some cases there is significant rotational excitation of the products. Skene, *et al.*[6] have shown that HeICl and NeICl have product rotational distributions consistent with an impulsive V-T,R predissociation mechanism from a bent molecular geometry configuration. For these two molecules it appears that the results are consistent with the same impulsive mechanism that applies to HeI_2, NeI_2, and $NeBr_2$, except that the bent structures of HeICl and NeICl increase the probability of large classical impact paramters, leading to a peak in the ICl fragment rotational distribution at relatively large values of j. Results from our laboratory[7,8] indicate that the mechanism for $NeCl_2$ vibrational predissociation is also different from that of

$NeBr_2$. The primary vibrational dissociation channel for $NeCl_2$ (B,v' = 11) remains $\Delta\upsilon = -1$ as for $NeBr_2$; however, there is significantly more rotational excitation than would have been predicted on the basis of a simple half-collision mechanism. Interpretation of the results using such a model would predict classical impact parameters > 6 Å.

The spectroscopy of the $NeBr_2$ B⟵X transition has been previously studied in detail. A high resolution excitation spectrum of the $NeBr_2$ B⟵X, 10⟵0 band has been analyzed to obtain the effective molecular geometry of the complex.[9] The molecule was found to have a T-shaped structure in both electronic states, with a Ne to Br_2 center-of-mass distance of 3.67±0.01 Å in the X electronic state and 3.65±0.01 Å in the B state. The similarity of the two bond lengths is surprising, considering that the Br_2 bond length increases by 0.6 Å upon electronic excitation. That the intermolecular potentials for the two electronic states are very similar was shown by the fact that careful searching revealed no combination bands involving excitation of the van der Waals vibrational modes in the electronic spectrum. Vibrational predissociation lifetimes for $NeBr_2$ (B,υ') have been obtained from homogeneous broadening measurements, which range from 355±100 ps to 1.7±0.3 ps for υ' = 10 and 27, respectively.[10]

Linebroadening measurements in van der Waals molecule excitation spectra give information about the decay rate of the prepared state but do not describe how the energy is distributed among the available product channels. Studies of the predissociation of electronically excited rare-gas halogen complexes have exploited the well-characterized B-X transitions of the halogens.[11] By dispersing the B⟶X fluorescence of the halogen fragment of the dissociation, its rotational and vibrational quantum state distribution is obtained. Here we present data on the product-state distribution of the Br_2 fragment from the photodissociation of $NeBr_2$.

II. EXPERIMENTAL

A mixture of 9:1 Ne:He (Spectra Gases) was passed over a trap maintained at -40°C containing Br_2 (MCB, reagent grade, naturally occurring isotopic abundances). $NeBr_2$ was prepared in a pulsed, free jet expansion of this mixture through a 500 μm nozzle at stagnation pressures of 100-140 psig. Care was taken to minimize the concentration of clusters containing more than one Ne atom. Higher-order clusters can be detected in LIF experiments as features blue-shifted from the $NeBr_2$ bandhead.[12] The rotational temperature of the jet was 0.7 K as measured by the relative intensity of Br_2 rotational lines.

The beam from an excimer (Lambda Physik EMG 201MSC) pumped dye laser (Lambda Physik FL 2002, 0.2 cm^{-1} bandwidth) crossed the expansion > 80 nozzle diameters downstream of the nozzle. The fluorescence from emitting species in the jet was either dispersed or, in some cases, total fluorescence was measured. The optical system for collecting total fluorescence from emitting species in the jet, the vacuum chamber, and pumping system has been previously described.[13] A cooled S-20 photomultiplier tube was used to measure total fluorescence spectra. Franck-Condon factors for the B-X transition of Br_2 favor emission at wavelengths significantly redder than the excitation wavelength;[14] therefore, scattered laser light was rejected by appropriate red-pass filters. A Spex 1269 monochrometer was used to disperse product emission collected by an optical system described elsewhere.[15] A red-sensitive RCA 31034 photomultiplier tube was used to measure dispersed fluorescence spectra. The preamplified photomultiplier signals were recorded by boxcar integrators (Stanford Research Systems). An IBM-PC microcomputer controlled the synchronization of the pulsed valve, lasers, and boxcar, scanned the dye laser and monochrometer, and performed signal averaging.

III. DATA AND RESULTS

Fig. 1 shows a total fluorescence spectrum of the

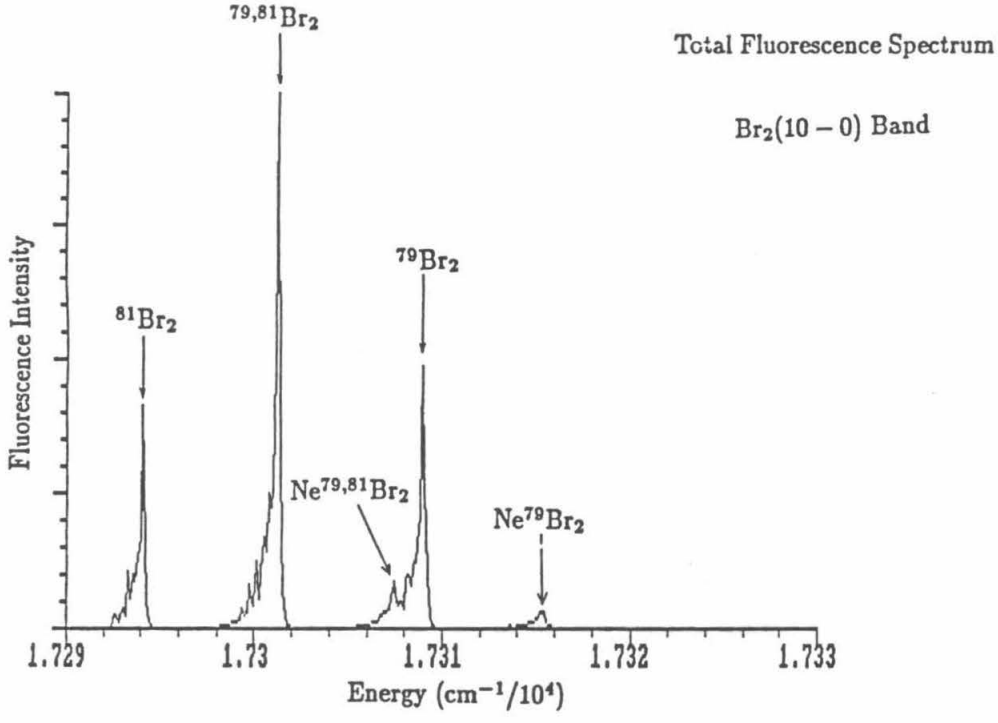

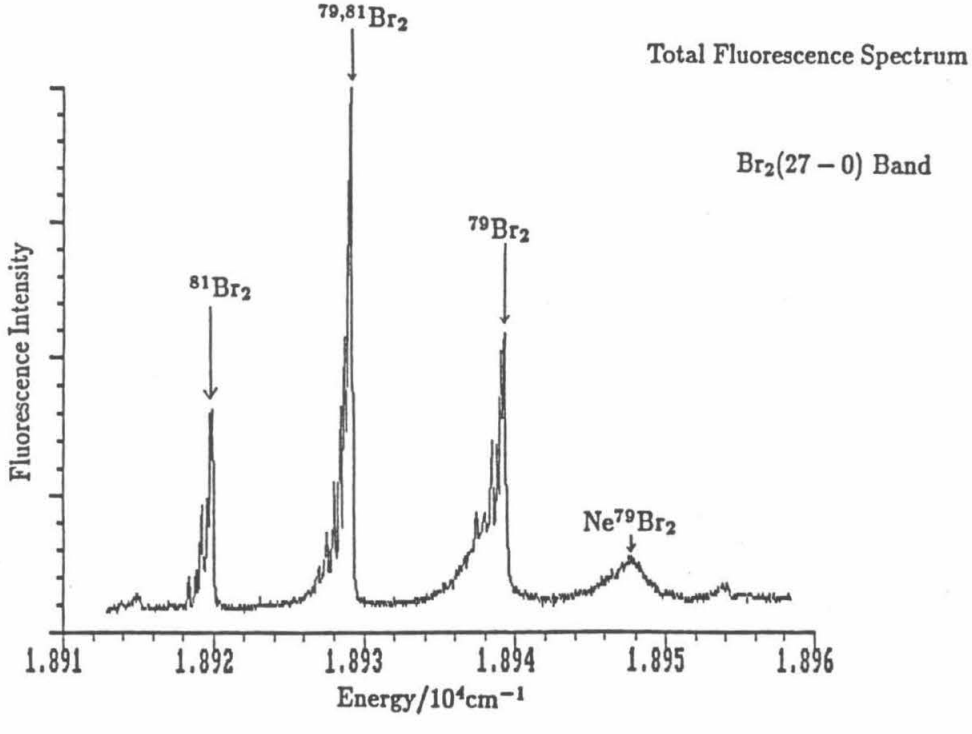

FIG. 1. Total fluorescence spectra of the Br_2 and $NeBr_2$ species in the jet.

jet obtained by detecting all the fluorescence from the excited species. The weak features to the blue of each Br_2 band have been assigned to the $NeBr_2$ van der Waals molecule.[12] In Fig. 1, the homogeneous broadening of the $NeBr_2$ B⟵X, 27⟵0 transition is clearly observable. Product state distributions for the photodissociation of $NeBr_2$ were obtained by tuning the excitation laser to the maximum of the $Ne^{79}Br_2$ B⟵X, υ'⟵υ''=0 van der Waals band and recording the emission spectrum of the Br_2 fragment of the decomposition. Only the $Ne^{79}Br_2$ isotopic species was studied in detail since it is best separated from the other isotopic species in the excitation spectrum.

The experiment can be best described in the following steps:

$$NeBr_2(X,\upsilon''=0,J'') + h\nu_{laser} \longrightarrow NeBr_2(B,\upsilon',J') \qquad \text{excitation} \quad (1)$$

$$NeBr_2(B,\upsilon',J') \longrightarrow Ne + Br_2(B,\upsilon'-z,j) \qquad \text{vibrational predissociation} \quad (2)$$

$$Br_2(B,\upsilon'-z,j) \longrightarrow Br_2(X) + h\nu_{fluor} \quad . \qquad \text{product fluorescence} \quad (3)$$

The vibrational predissociation lifetime in Eq. (2) ranges from 355 ps for υ' = 10 to 1.7 ps for υ' = 27. The radiative lifetime for fluorescence of $Br_2(B)$ in Eq. (3) is ~8 μs,[11] so that a negligible amount of fluorescence

occurs from the van der Waals complex prior to its fragmentation.

Fig. 2 shows the Br_2 product emission spectra obtained by positioning the pump laser on various $Ne^{79}Br_2$ $B \longleftarrow X$, $\upsilon' \longleftarrow 0$ band maxima and scanning the monochometer through the fragment Br_2 $B \longrightarrow X$ emission bands. Wide monochrometer slits were required (~5 cm^{-1} resolution) to obtain acceptable signal-to-noise ratios so that band contours, rather than resolved transitions of the $B \longrightarrow X$ emission bands, were obtained. For $NeBr_2$ ($B, \upsilon' < 26$) the dominant product vibrational channel is that in which one quantum of the Br_2 stretch is used to dissociate the molecule. As higher vibrational states of $NeBr_2$ are excited, the product channels in which multiple Br_2 quanta are lost become increasingly more probable. Particularly striking in Fig. 2 is the dramatic cutoff of intensity in the one quantum loss channel for $\upsilon' > 28$.

Relative populations of the vibrational states of the Br_2 fragment of the decomposition are extracted from the spectra of Fig. 2. There are three phenomena that complicate the extraction of quantitative product-state distributions. One is the relatively long fluorescence lifetime of the Br_2 B electronic state. Inelastic collisions of the Br_2 fragment with other species in the expansion prior to fluorescence will make the observed Br_2 fragment-state distribution different from that initially

FIG. 2. Br_2 fragment emission spectra observed when the laser is positioned on the maximum of the $Ne^{79}Br_2$ B⟵X, υ'⟵0 vibrational band. The transition labels on the far left of each row of spectra indicate the number of quanta deposited in the Br-Br stretch of $Ne^{79}Br_2(B)$, and the Br_2 fragment emission spectra on that row show the relative fluorescence intensity of the $Br_2(B)$ fragments that appear in different product channels. Each column of spectra correspond to a specific $\Delta\upsilon$ relaxation channel: left column, $\Delta\upsilon = -1$; center column, $\Delta\upsilon = -2$; right column, $\Delta\upsilon = -3$. The identity of each emission band is indicated by a transition label, υ'⟶υ''. The $\Delta\upsilon = -1$ channel is dominant while it is energetically open; however, the population of other vibrational channels increases with υ'. In the decomposition of $Ne^{79}Br_2(B,\upsilon'=28)$, the $\Delta\upsilon = -1$ channel has completely closed. (The weak emission to the red of the $^{79}Br_2$ B⟶X, 27⟶1 origin is due to isotopic contamination.) See the text for further discussion.

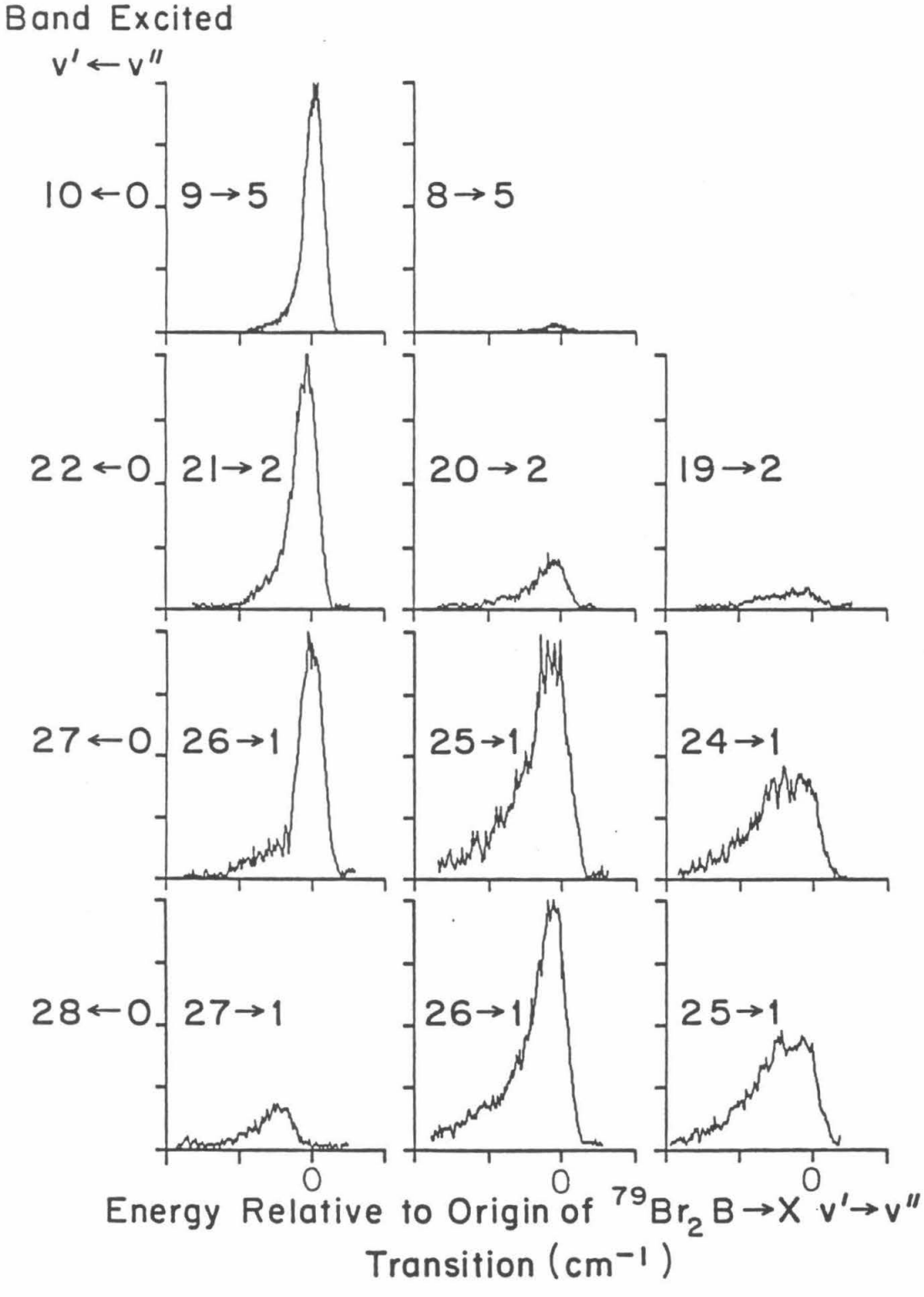
Band Excited
v′ ← v″
10 ← 0
9 → 5
8 → 5
22 ← 0
21 → 2
20 → 2
19 → 2
27 ← 0
26 → 1
25 → 1
24 → 1
28 ← 0
27 → 1
26 → 1
25 → 1
0
0
0
Energy Relative to Origin of $^{79}Br_2$ B → X v′ → v″
Transition (cm^{-1})

produced by the dissociation. In such collisions there is the possibility for rotational, vibrational, and electronic relaxation of the fragment Br_2.[11] Far from the nozzle, the number density of molecules in the expansion varies as the inverse square of the distance from the nozzle source. By increasing the distance of the excitation region from the nozzle, the number of collisions is reduced at the expense of fluorescence intensity. The relative amount of vibrational relaxation of the nascent Br_2 in this experiment was determined by exciting uncomplexed Br_2 in the expansion and dispersing the fluorescence. At a position 80 nozzle diameters downstream of the nozzle, where the number density is $\sim 10^{16}/cm^3$, the measured population of vibrationally relaxed uncomplexed Br_2 never exceeded 8 % of the unrelaxed population. The Appendix to this chapter shows how these experimental measurements of the vibrational relaxation of uncomplexed Br_2 are used to correct the measured vibrational population distributions of the Br_2 (B) fragment of $NeBr_2$ (B) decomposition for vibrational relaxation of the nascent fragment. Collisions also alter the nascent rotational state distribution to some degree. The rotational temperature of uncomplexed Br_2 emitting from the same vibrational state in which it was prepared is identical to the 0.7 K rotational temperature of the jet within experimental error. However, vibrationally

inelastic collisions also appear to alter significantly the rotational state of the Br_2. For example, the rotational temperature of Br_2 (B,υ'=21), which has undergone an inelastic collision in which $\Delta\upsilon'$=-1 is ~8 K. Br_2 produced by the photodissociation of $NeBr_2$, will have significantly more translational energy than uncomplexed Br_2. Russell, *et al.*[16] have performed a careful study of the energy redistribution that occurs in low-energy collisions of I_2 (B) and He in a free jet expansion. They found that there is a very high cross section for vibrational relaxation in low-energy collisions and that the cross section actually decreases with increasing collision energy. This result implies that vibrational relaxation of Br_2 (B) produced by van der Waals molecule predissociation should be smaller than that measured for uncomplexed Br_2 (B). In order to confirm that the translationally excited Br_2 (B) rotational distribution was not significantly altered in vibrationally elastic collisions, the 10$\longleftarrow$0 B$\longleftarrow$X band of $NeBr_2$ was studied by the laser pump-probe technique discussed in Chap. 3 in which the probe laser is delayed by only 10 ns so that the product state distributions are not affected by collisions.[17] Within experimental uncertainty, the rotational distribution of the υ'=9 Br_2 fragment was the same in both measurements.

Another complication in obtaining product-state

distributions results from the fact that the Br_2 B state undergoes electronic predissociation at a rate which depends upon its rotational state, j.[11,18] This effect reduces significantly the lifetime of the excited state Br_2 fragments for the higher j states populated in the dissociation. In order to minimize the potential distortion of the emission spectra due to this effect, fluorescence was averaged for only the first 400 ns following the laser pulse. Since the j-dependent electronic predissociation rate constants are not known for each band studied, no attempt was made to correct the distributions for this effect. The agreement of the values for the rotational temperature of Br_2 (B,υ'=10) obtained by dispersed fluorescence and the pump-probe technique (which should be practically unaffected by electronic predissociation) indicate that electronic predissociation does not qualitatively change the results obtained.

Finally, there are interferences arising from the presence of other Br_2 isotopic species present in the expansion. The broad Lorentzian profiles of higher υ' bands of $NeBr_2$ prevent selective excitation of van der Waals molecules associated with only one Br_2 isotopic species. Also, because of the limited resolution of our monochrometer, it is difficult to separate totally the fluorescence from the $^{79}Br_2$ and the $^{79}Br^{81}Br$ species.

Among the bands studied, only the 10⟵0 and 22⟵0 are completely free from contamination of the dispersed $^{79}Br_2$ emission by the $^{79}Br^{81}Br$ species. With these caveats in mind, the results presented here should be accepted as a good qualitative description of the photodissociation dynamics. A quantitative description of the final rotational quantum state distribution remains to be determined in detailed laser pump-probe experiments such as those described in Chap. 3.

Table 1 presents the product state distributions for the vibrational predissociation of $Ne^{79}Br_2$ extracted from the spectra of Fig. 1. Because of the uncertainties described above, only one significant figure is reported. Populations are extracted from the observed intensities, corrected for collisional vibrational relaxation and fluorescence Franck-Condon factors as described in the Appendix. Rotational temperatures are reported for the $\Delta\upsilon = -1$ channels of $\upsilon'=10$ and $\upsilon'=22$ states of $NeBr_2(B)$.

IV. DISCUSSION

Comparison of the product emission spectra for $Ne^{79}Br_2$ $(B,\upsilon=27)$ and $Ne^{79}Br_2$ $(B,\upsilon'=28)$ shows a dramatic decrease in the apparent product population in the $\Delta\upsilon = -1$ channel. That the weak emission near where emission from the $^{79}Br_2$ $(B,\upsilon'=27)$ fragment of $Ne^{79}Br_2$ $(B,\upsilon'=28)$ should occur is actually due entirely to the $^{79}Br^{81}Br$ species, is

Table 1. Vibrational Product-State Distributions for the Photodissociation of $Ne^{79}Br_2$

Band Excited $\upsilon' \longleftarrow \upsilon''$	Relative Population of Product Channel $\Delta\upsilon$				
	$\Delta\upsilon=-1$	$\Delta\upsilon=-2$	$\Delta\upsilon=-3$	$\Delta\upsilon=-4$	$\Delta\upsilon=-5$
$10 \longleftarrow 0$	1[1]	0	-	-	-
$22 \longleftarrow 0$	1[2]	0.2	0.1	0.1	0
$27 \longleftarrow 0$	0.7	1	0.6	0.3	0.1
$28 \longleftarrow 0$	0[3]	1	0.6	0.4	0.2

(1) $T_{rot} = 6$ K

(2) $T_{rot} = 5$ K

(3) The weak fluorescence observed in this channel is entirely due to the decomposition of $Ne^{79}Br^{81}Br$ (see text).

shown by the absence of any emission at the $^{79}Br_2$ B$\longrightarrow$X, 27$\longrightarrow$1 band origin. Because of the very broad homogeneous linewidth of the van der Waals features in this region, it is no longer possible to excite selectively only one isotopic species of $NeBr_2$. The $\Delta\upsilon = -1$ channel has, in fact, closed for $Ne^{79}Br_2$ (B,υ'=28). Assuming that the Br_2 product rotational energy is negligible, then by conservation of energy $\omega_\upsilon = D_0(B) + E_{trans}$, where E_{trans} is the relative translational kinetic energy of the recoiling fragments, $D_0(B)$ is the dissociation energy of the Ne•••Br_2 (B) bond, and ω_υ is the energy of the υth vibrational quantum of Br_2 (B). Because of the anharmonicity of the Br-Br B state potential, ω_υ decreases with υ. When $\omega_\upsilon < D_0$, the $\Delta\upsilon = -1$ channel must close. The amount of energy released in the $\Delta\upsilon = -1$ channel for $Ne^{79}Br_2$ (B,υ'=27) is the energy in a quantum of the Br_2 stretch, $\omega_{27} = 63.5\ cm^{-1}$. The $\Delta\upsilon = -1$ channel closes at υ'=28, where $\omega_{28} = 59.7\ cm^{-1}$. Thus, the van der Waals bond energy for $Ne^{79}Br_2$ in the B electronic state is bracketed to be $59.7 \leq D_0(B) \leq 63.5\ cm^{-1}$. The blue shift[12] of a $Ne^{79}Br_2$ band origin from the $^{79}Br_2$ band origin is a measure of how much deeper the van der Waals potential is in the ground (X) electronic state than in the excited (B) state. By adding the blue shift of the $Ne^{79}Br_2$ bandhead from the $^{79}Br_2$ bandhead to the bond energy of the B state, the X state bond energy is

$68.5 \leq D_0(X) \leq 72.6\ cm^{-1}$. This bond energy determination is close to an estimate of $D_0(B) = 64 \pm 4\ cm^{-1}$ made by Swartz, et al.[12] on the basis of an increasing lifetime for $NeBr_2$ (B,υ'>27).

There remains the question of why weak fluorescence is observed in the $\Delta\upsilon = -1$ channel for $Ne^{79}Br^{81}Br$ (B,υ'=28). It may appear contradictory that fluorescence from $\upsilon' = 27$ of $^{79}Br^{81}Br$ should be detected upon excitation of a band that cannot populate $\upsilon' = 27$ for $Ne^{79}Br_2$. For $NeBr_2$ $\upsilon' = 28$, the full width at half-maximum of the Lorentzian lineshape is ~3 cm^{-1}. When the excitation laser is positioned on the maximum of the $Ne^{79}Br_2$ (B,υ'=28) band, it also excites the blue tail of the Lorentzian profile of the $Ne^{79}Br^{81}Br$ (B,υ'=28) absorption at an energy that lies above the threshold for population of the $^{79}Br^{81}Br$ (B,υ'=27) product. In a separate experiment where the monochrometer is positioned at the origin of the $^{79}Br_2$ fluorescence band (so that fluorescence of the other isotopic species is not detectable) and the excitation laser is tuned through the Lorentzian profile of $Ne^{79}Br_2$ (B,υ'=28), a weak threshold occurs when the energy of the prepared state is sufficient to predissocate via the one-quantum mechanism. This phenomena is illustrated in Fig. 3.

The rotational distributions obtained for the Br_2 fragment can be closely simulated by a Boltzmann

FIG. 3. Threshold for population of the $\Delta\upsilon = -1$ channel. The top figure schematically illustrates how the energy of $NeBr_2$ (B,υ'=28) level overlaps with the continuum product states. The bottom figure shows the observed emission intensity from $^{79}Br_2$ (B,υ'=26) and $^{79}Br_2$ (B,υ'=27), when the laser is tuned across the $Ne^{79}Br_2$ B$\longleftarrow$X, 28$\longleftarrow$0 band. Since excitation anywhere on the band profile gives rise to a state that can decay into the $^{79}Br_2$ (B,υ'=26) continuum (the $\Delta\upsilon = -2$ channel), the full Lorentzian profile of the $Ne^{79}Br_2$ B$\longleftarrow$X, 28$\longleftarrow$0 absorption is observed when the emission from $^{79}Br_2$ (B,υ'=26) is monitored. Detection of fluorescence from $^{79}Br_2$ (B,υ'=27) (the $\Delta\upsilon = -1$ channel) is not observed until the excitation energy exceeds the threshold for production of products in the $^{79}Br_2$ (B,υ'=27) set of continuum product states.

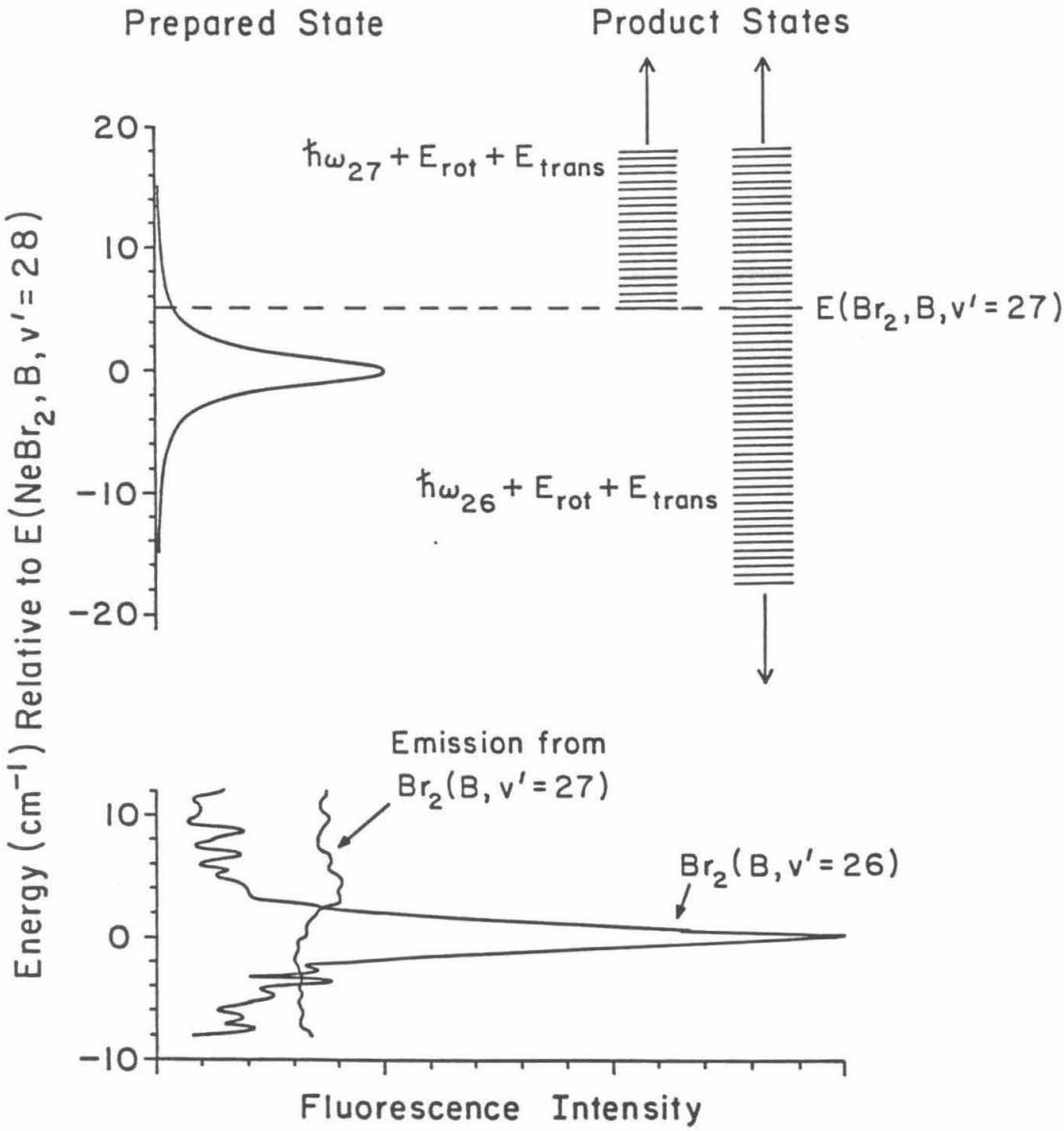
Prepared State
Product States
20
10
0
-10
-20
$\hbar\omega_{27} + E_{rot} + E_{trans}$
$E(Br_2, B, v' = 27)$
$\hbar\omega_{26} + E_{rot} + E_{trans}$
Energy (cm^{-1}) Relative to $E(NeBr_2, B, v' = 28)$
Emission from
$Br_2(B, v' = 27)$
$Br_2(B, v' = 26)$
10
0
-10
Fluorescence Intensity

distribution, although our limited resolution does not preclude somewhat non-Boltzmann behavior. In fact, the distribution must have a definite termination at some maximum rotational quantum number, j_{max}, that is the largest j that can be populated according to conservation of energy. For the $Ne^{79}Br_2$ (B,υ'=10) $\Delta\upsilon = -1$ channel, 70 cm^{-1} is available for product rotational and relative translational kinetic energy and $j_{max} \sim 35$. The observed rotational temperature of 6 K has an average of 4 cm^{-1} of energy in rotation and gives practically no population of rotational levels approaching $j = 35$. This contrasts strongly with the $NeCl_2$ (B,υ'=11) rotational distribution in which every state kinematically and energetically allowed has significant population (available energy = 87 cm^{-1}) and an average of 15 cm^{-1} of energy in rotation.[7,8] The very cold ($\lesssim$ 1 K) rotational distribution of the Br_2 (B,υ'=26) product from $NeBr_2$ (B,υ'=27) is due to the small amount of energy available for rotation near the closure of the one-quantum channel.

These results are in complete agreement with the dynamical propensity rules proposed by Ewing for vibrational predissociation of van der Waals molecules.[4] Because of the relatively large rotational constant of Cl_2, a Cl_2 fragment can accept much more rotational energy than a Br_2 fragment in the same rotational state. This

means that Br_2 must have a much larger population of the high-j levels than Cl_2 in order to accept the same amount of rotational energy. According to Ewing's model, large values of j are of low probability, so the fragment Br_2 should be rotationally cold.

For high υ' states of $NeBr_2$ (B), the vibrational product state distributions are qualitatively quite broad, with appreciable intensity still present at $\Delta\upsilon = -5$ for excitation of $NeBr_2$ (B) $\upsilon' = 27$ and 28. It is apparent that the number of vibrational product channels with significant population increases with υ'. A similar result is observed in the vibrational predissociation of NeI_2, where for NeI_2 (B,υ'=21) more that 90 % of the product population is present in the $\Delta\upsilon = -1$ channel[19] and for NeI_2 (B,υ'=33), where significant population is observed in several product channels.[20]

In conclusion, the distribution of product energy upon dissociation of $NeBr_2$ is much as would be expected from consideration of the momentum gap theories of Beswick and Jortner[2] and Ewing,[3] in that little rotational energy is imparted to the Br_2 fragment ($\langle E_{rot} \rangle \sim 4$ K), and the highest open vibrational product channel is favored in the dissociation. The binding energy of $NeBr_2$ in the ground (X) electronic state is bracketed by measurement of a dynamical threshold to be $68.5 \leq D_0 \leq 76.2$ cm^{-1}.

V. ACKNOWLEDGEMENT

We gratefully acknowlege the National Science Foundation for the financial support of this research.

VI. APPENDIX

This appendix describes how relative vibrational populations of the $Br_2(B)$ fragment from the photodissociation of $NeBr_2$ can be calculated from the integrated intensities of the fragment fluorescence and experimental measurements of the population relaxation of uncomplexed $Br_2(B)$. Vibrational state population ratios were extracted from the integrated rotational contours of each vibrational emission band of the Br_2 $B \longrightarrow X$ transition using the equation

$$\frac{[Br_2(\upsilon'-z)]}{[Br_2(\upsilon')]} = \frac{I_{\upsilon'-z,\upsilon''}}{I_{\upsilon',\upsilon''}} \cdot \frac{q_{\upsilon',\upsilon''}}{q_{\upsilon'-z,\upsilon''}} \cdot \frac{\nu^3_{\upsilon',''}}{\nu^3_{\upsilon'-z,\upsilon''}} , \qquad \text{(A1)}$$

where $I_{\upsilon',\upsilon''}$ is the observed integrated intensity of the $\upsilon' \longrightarrow \upsilon''$ band, $q_{\upsilon',\upsilon''}$ is the Franck-Condon factor,[14] and $\nu_{\upsilon',\upsilon''}$ is the frequency of the transition.

The derivation of the kinetic equations describing the relaxation of the initial distribution following the laser pulse follows closely that of Sharfin, *et al.* for a cw laser experiment.[21] The relaxation processes for uncomplexed Br_2 are

$$Br_2(\upsilon_i') \xrightarrow{A(\upsilon_i',\upsilon'')} Br_2(\upsilon'') + h\nu_{fluor}$$

fluorescence (A2)

$$Br_2(\upsilon_i') + X \xrightarrow{Q(\upsilon_i')} 2Br + X$$

quenching (A3)

$$Br_2(\upsilon_i') + X \xrightarrow{R(\upsilon_i',\upsilon_f')} Br_2(\upsilon_f') + X \ .$$

vibrational relaxation (A4)

Here we adopt the conventional notation where the primed υ is the vibrational quantum number in the excited electronic state, and the double primed υ in the ground electronic state. The duration of the excitation pulse is negligible with respect to the rate of these processes. The population of the initially prepared vibrational level υ_i' of the B state, $[Br_2(\upsilon_i')]$, decays as

$$[Br_2(\upsilon_i')] = [Br_2(\upsilon_i')]_o \ e^{-\Gamma t} \ . \tag{A5}$$

$[Br_2(\upsilon_i')]_o$ is the concentration of $Br_2(\upsilon_i')$ immediately following laser excitation, t is the elapsed time since the laser pulse, and

$$\Gamma = \sum_{\upsilon''} A(\upsilon_i',\upsilon'') - \sum_{\upsilon_f'<\upsilon_i'} R(\upsilon_i',\upsilon_f')[X] - Q(\upsilon_i')[X] \ . \tag{A6}$$

The decay rate, Γ, is assumed to be independent of the

initial vibrational state, υ_i', over a narrow range of initial states.

The population of $Br_2(\upsilon_i'-1)$ varies in time as

$$\frac{d[Br_2(\upsilon_i'-1)]}{dt} = -\Gamma[Br_2(\upsilon_i'-1)] + R(\upsilon_i',\upsilon_i'-1)[X][Br_2(\upsilon_i')] \ . \qquad (A7)$$

Applying the initial condition of $[Br_2(\upsilon_i'-1)]_{t=0} = 0$ gives

$$[Br_2(\upsilon_i'-1)] = [Br_2(\upsilon_i')]_o \ R(\upsilon_i',\upsilon_i'-1)[X]t \ e^{-\Gamma t} \qquad (A8)$$

$$[Br_2(\upsilon_i'-2)] = R(\upsilon_i',\upsilon_i'-2)[X][Br_2(\upsilon_i')]_o t \ e^{-\Gamma t} + \tfrac{1}{2}R(\upsilon_i'-1,\upsilon_i'-2)R(\upsilon_i',\upsilon_i'-1)[X]^2[Br_2(\upsilon_i')]_o t^2 \ e^{-\Gamma t} \ . \qquad (A9)$$

At a given observation time, τ, the vibrational state population ratios are

$$\left[\frac{[Br_2(\upsilon_i'-1)]}{[Br_2(\upsilon_i')]}\right]_{t=\tau} = R(\upsilon_i',\upsilon_i'-1)[X]\tau \equiv f_1 \qquad (A10)$$

$$\left[\frac{[Br_2(\upsilon_i'-2)]}{[Br_2(\upsilon_i'-1)]}\right]_{t=\tau} = R(\upsilon_i',\upsilon_i'-2)[X]\tau + \tfrac{1}{2}R(\upsilon_i'-1,\upsilon_i'-2)R(\upsilon_i',\upsilon_i'-1)[X]^2\tau^2 \equiv f_2 \ . \qquad (A11)$$

Now consider the relaxation of the population distribution that arises from the photodissociation of

$NeBr_2$. Again, the duration of the laser pulse and the subsequent fragmentation lifetime of $NeBr_2$ are negligible with respect to the rate of the relaxation processes. At time $t=0$, the initial population of each vibrational state is $[Br_2(\upsilon_i'-z)]_o$, where z is the number of Br_2 vibrational quanta lost in the dissociation. Applying this set of initial conditions and assuming the relaxation rate constants to be equal to those for uncomplexed Br_2 as discussed in Sec. III, the time-dependent vibrational state populations are

$$[Br_2(\upsilon_i'-1)] = [Br_2(\upsilon_i'-1)]_o \; e^{-\Gamma t} \tag{A12}$$

$$\begin{aligned}[Br_2(\upsilon_i'-2)] &= [Br_2(\upsilon_i'-2)]_o \; e^{-\Gamma t} \\ &\quad + Br_2(\upsilon_i'-1)]_o R(\upsilon_i'-1,\upsilon_i'-2)[X]t \; e^{-\Gamma t}\end{aligned} \tag{A13}$$

$$\begin{aligned}[Br_2(\upsilon_i'-3)] &= [Br_2(\upsilon_i'-3)]_o \; e^{-\Gamma t} \\ &\quad + R(\upsilon_i'-1,\upsilon_i'-3)[X][Br_2(\upsilon_i'-1)]_o t \; e^{-\Gamma t} \\ &\quad + \tfrac{1}{2}R(\upsilon_i'-2,\upsilon_i'-3)R(\upsilon_i'-1,\upsilon_i'-2)[X]^2[Br_2(\upsilon_i'-1)]_o t^2 \; e^{-\Gamma t} \\ &\quad + [Br_2(\upsilon_i'-2)]_o R(\upsilon_i'-2,\upsilon_i'-3)t \; e^{-\Gamma t} \; .\end{aligned} \tag{A14}$$

At a given observation time, τ, the product population ratios are

$$\left[\frac{[Br_2(\upsilon_i'-2)]}{[Br_2(\upsilon_i'-1)]}\right]_{t=\tau} = \frac{[Br_2(\upsilon_i'-2)]_o}{[Br_2(\upsilon_i'-1)]_o} + f_1 \tag{A15}$$

$$\left[\frac{[Br_2(\upsilon_i'-3)]}{[Br_2(\upsilon_i'-1)]}\right]_{t=\tau} = \frac{[Br_2(\upsilon_i'-3)]_o}{[Br_2(\upsilon_i'-1)]_o} + f_2 + f_1 \frac{[Br_2(\upsilon_i'-2)]_o}{[Br_2(\upsilon_i'-1)]_o} , \tag{A16}$$

where f_1 and f_2 are the values obtained in Eqs. (A10) and (A11) for an experiment on uncomplexed Br_2.

The branching ratios $[Br_2(\upsilon_i'-z)]_o/[Br_2(\upsilon_i'-1)]_o$ are obtained by experimental measurements of the relaxation of uncomplexed Br_2 and then by using Eqs. (A15) and (A16). In our experiment the emission is observed for a short but finite length of time, determined by the width of the boxcar gate. This requires Eqs. (A5), (A8-9), and (A12-14) to be integrated over the observation time. The equations are then somewhat more algebraically complex, but the final ratios are identical.

REFERENCES

[1]D.H. Levy, Adv. Chem. Phys. **47**, 323 (1981).

[2]J.A. Beswick and J. Jortner, Adv. Chem. Phys. **47**, 363 (1981).

[3]G.E. Ewing, Faraday Discuss. Chem. Soc. **73**, 325 (1982).

[4]G.E. Ewing, J. Phys. Chem. **91**, 4662 (1987).

[5]D.E. Brinza, B.A. Swartz, C.M. Western, and K.C. Janda, J. Chem. Phys. **79**, 1541 (1983).

[6]J.M. Skene, J.C. Drobits, and M.I. Lester, J. Chem. Phys. **85**, 2329 (1986).

[7]J.I. Cline, N. Sivakumar, D.D. Evard, and K.C. Janda, J. Chem. Phys. **86**, 1636 (1987).

[8]Chap. 4 of this thesis.

[9]F. Thommen, D.D. Evard, and K.C. Janda, J. Chem. Phys. **82**, 5295 (1985).

[10]J.I. Cline, D.D. Evard, B.P. Reid, N. Sivakumar, F. Thommen, and K.C. Janda, in *Structure and Dynamics of Weakly Bound Molecular Complexes*, in A. Weber, ed. (D. Reidel Publishing Co., Dordrecht, 1987), p. 533.

[11]M.C. Heaven, Molecular Spectroscopy, Chem. Soc. Spec. Per. Rep., The Chemical Society, London, in press.

[12]B.A. Swartz, D.E. Brinza, C.M. Western, and K.C. Janda, J. Phys. Chem. **84**, 6272 (1984).

[13]D.E. Brinza, C.M. Western, D.D. Evard, F. Thommen, B.A. Swartz, and K.C. Janda, J. Phys. Chem. **88**, 2004 (1984).

[14]J.A. Coxon, J. Quant. Spectrosc. Radiat. Transfer **12**, 639 (1972).

[15]B.A. Swartz, Ph.D. Thesis, California Institute of Technology, 1984.

[16]T.D. Russell, B.M. DeKoven, J.A. Blazy, and D.H. Levy, J. Chem. Phys. **72**, 3001 (1980).

[17]N. Sivakumar, J.I. Cline, and K.C. Janda, manuscript in preparation.

[18]M. Siese, E. Tiemann, and U. Wulf, Chem. Phys. Lett. **117**, 208 (1985).

[19]J.E. Kenny, K.E. Johnson, W. Sharfin, and D.H. Levy, J. Chem. Phys. **72**, 1109 (1980).

[20]J.A. Blazy, B.M. DeKoven, T.D. Russell, and D.H. Levy, J. Chem. Phys. **72**, 2439 (1980).

[21]W. Sharfin, K.E. Johnson, L. Wharton, and D.H. Levy, J. Chem. Phys. **71**, 1292 (1979).

APPENDIX A

Classical Trajectory Program

The following FORTRAN computer code generates classical trajectories for an atom-rigid diatom system. It is designed to be the starting point for semiclassical analyses of direct photodissociations using the theory of Schinke.

The classical Hamiltonian of the system is

$$H(R,\gamma,P,j) = \frac{P^2}{2\mu} + Bj^2 + \frac{l^2}{2\mu R^2} + V(R,\gamma) \ ,$$

where R, γ, j, l, and μ have the same definitions as in Chap. 3, P is the radial momentum conjugate to R, B is the rotational constant of the diatom, and V is the atom-diatom potential averaged over the diatom vibration as described immediately following Eq. (9) of Chap. 3. Defining the total angular momentum of the system, J, as zero, requires $j = -l$. The classical equations of motion are then

$$\frac{dR}{dt} = \frac{P}{\mu} \qquad \frac{dP}{dt} = -\frac{\partial V}{\partial R} + \frac{j^2}{\mu R^3} \ ;$$

$$\frac{d\gamma}{dt} = 2j\left[B + \frac{1}{2\mu R^2}\right] \qquad \frac{dj}{dt} = -\frac{\partial V}{\partial \gamma} \ .$$

The initial conditions are chosen according to the recipe given in R. Schinke, J. Chem. Phys. **85**, 5049 (1986) for the semiclassical treatment of the direct photodissociation of triatomic molecules; namely, $P_o = 0$, $j_o = 0$, γ_o is varied, and R_o is chosen such that the total energy of the system is E. However, this program also allows $|j_o|$ to vary from 0 to $3\hbar$.

It is assumed that a potential is given in a subroutine POTEVAL, which returns the potential energy in wavenumbers as a function of R in Å and γ in radians.

```
      PROGRAM TRAJ
C
C     PROGRAM TO CALCULATE CLASSICAL TRAJECTORIES FOR
C     ATOM-DIATOM DISSOCIATIONS.  THE DIATOMIC BOND LENGTH
C     IS FIXED.
C     GENERALIZED COORDS FOR THE PROBLEM:
C          R -> ATOM-DIATIOMIC CENTER-OF-MASS DISTANCE
C          P -> CONJUGATE MOMENTUM FOR R
C          GAMMA -> ANGLE OF Rvector WITH RESPECT TO
C                   DIATOMIC AXIS
C          J -> CONJUGATE MOMENTUM FOR GAMMA, I.E. ANG.
C                   MOMENTUM
C
C     FOR A DESCRIPTION OF THE CLASSICAL HAMILTONIAN FOR
C     THIS SYSTEM SEE R. SCHINKE, J. CHEM. PHYS., VOL. 85,
C     5049 (1986).
C
      IMPLICIT REAL*4 (J)
      COMMON FMU,SR,JCONV,ECONV,B
C
C*****************************************************************
C
C     PHYSICAL CONSTANTS FOR MOLECULE
C     B, ROTATIONAL CONSTANT OF DIATOMIC, IN CM^(-1)
      B=.12616
C     FMU, REDUCED MASS OF ATOM-DIATOMIC SYSTEM, IN AMU
      FMU=3.784
C     SR, THE BOND LENGTH OF THE DIATOMIC, IN ANGSTROMS
      SR=2.7637
C     SR IS NOT USED IN TRAJ, BUT MAY BE NECESSARY IN
C     THE SUBROUTINE POTEVAL THAT COMPUTES THE POTENTIAL.
C     EO, THE TOTAL ENERGY OF THE SYSTEM, IN CM^(-1)
      EO=121.809
C
C*****************************************************************
C
C     PARAMETERS FOR TRAJECTORIES
C     NANG, NUMBER OF ANGLES TO CALCULATE TRAJECTORIES
      NANG=19
C     AMAX, GAMMA WILL RANGE FROM 0. TO AMAX, IN DEGREES
      AMAX=90.
C     MAXIT, MAXIMUM NUMBER OF ITERATIONS
      MAXIT=5000
C     RMAX, MAXIMUM RADIAL DISTANCE TO CALCULATE
C          TRAJECTORIES, ANGSTROMS
      RMAX=25.
C     DELTAT, THE TIME INCREMENT, IN PICOSECONDS
      DELTAT=0.01
C
C*****************************************************************
C
      PI=3.14159
```

```
C
C
C*************************************************************
C
C     INITIAL CONDITIONS:
C     THE INITIAL CONDITIONS ARE SELECTED WITH INTEGRAL
C     VALUES OF J UP TO 6 Hbar, PO=0, AND RO SELECTED FOR
C     ENERGY CONSERVATION.
C     GAMMAO IS VARIED.
C     P, THE RADIAL MOM. OF THE REDUCED MASS, IN UNITS OF
C          AMU*ANGSTROM/PS
      PO=0.0
C     J, THE ANGULAR MOM. OF THE REDUCED MASS, IN UNITS OF
C          HBAR
C     GAMMA=VARIED, R=SELECTED TO GIVE THE CORRECT VALUE
C          OF EO-EZPT
C
C     GAMMA IS DEFINED IN DEGREES AS:
C
C         C
C          \         B IS THE (A-B) ROTATIONAL CONT.(CM-1)
C           \R       FMU IS THE C-(A-B) REDUCED MASS (AMU)
C            \       R,SR IN ANGSTROMS
C       GAMMA \
C A-------------------------B
C             SR
C
C
C*************************************************************
C
C
C     INTERNALLY, THIS PROGRAM OPERATES IN THE FOLLOWING
C     UNITS:
C     R -> ANGSTROM
C     P -> AMU*ANGSTROM/PS
C     GAMMA -> UNITLESS
C     J -> AMU*(ANGSTROM**2)/PS
C     V (ENERGY) -> AMU*(ANGSTROM**2)/(PS**2)
C
C     TO GET ENERGY IN REDUCED UNITS, MULTIPLY E IN
C     CM^(-1) BY THE FACTOR ECONV
      ECONV=1.196259
C     B IS GIVEN AS THE SPECTROSCOPIC B IN CM^(-1), IT
C     MUST BE CONVERTED TO THE CLASSICAL VALUE OF 1/2I, IN
C     UNITS OF 1/(AMU*(ANGSTROM**2))
C     TO GET CLASSICAL B, MULTIPLY SPECTROSCOPIC B BY
C     BCONV
      BCONV=.029660
      B=B*BCONV
C     TO GET ANG. MOM. IN REDUCED UNITS, MULTIPLY J IN
C     UNITS OF HBAR BY THE FACTOR JCONV
      JCONV=6.350772
      J=J*JCONV
```

```
C
C*****************************************************************
C
C     LOOP OVER THE ANGLES, COMPUTE TRAJECTORIES
C
C     DIRECT OUTPUT TO UNIT 9
      OPEN(9,STATUS='NEW',FORM='FORMATTED')
C
      DO 300 I=1,NANG
      GAMMA=(I-1)*(AMAX/(NANG-1))
C
C     CONVERT GAMMA TO RADIANS
      GAMMA=GAMMA*2*PI/360
      GAMMAO=GAMMA
C
C     ASSUME INITIAL ANGULAR MOMENTUM RANGES
C     FROM JO=0 TO 3
C     LOOP OVER INITIAL ANGULAR MOMENTUM
      DO 250 II=1,4
      JO=(II-1)*2.*JCONV
      GAMMAO=GAMMA
      PO=0.
C - - - - - - - - - - - - - - - - - - - - - - - - - - - - - - - - -
C     COMPUTE INITIAL VALUE OF RO, SO THAT
C     Erot(R)+V(R)=EO; I.E. INNER TURNING POINT OF THE
C     COLLISION
C
      ETOLER=0.01
C     ENERGY TOLERANCE
C
      RGUESS=2.0
C     LOWER LIMIT FOR RO IS ASSUMED TO BE 2 ANGSTROMS
C
      DR=0.05
 40   FORMAT(A)
      CALL POTEVAL(COS(GAMMAO),RGUESS,SR,VGUESS,DVDR)
      EROT=B*JO**2+(JO**2)/(2*FMU*RGUESS**2)
      FOLD=EROT/ECONV+VGUESS-EO
 50   RGUESS=RGUESS+DR
      CALL POTEVAL(COS(GAMMAO),RGUESS,SR,VGUESS,DVDR)
      EROT=B*JO**2+(JO**2)/(2*FMU*RGUESS**2)
      IF((FOLD*(EROT/ECONV+VGUESS-EO)) .GT. 0.) GOTO 60
      RGUESS=RGUESS-DR
      DR=DR/2.
 60   IF(ABS(EROT/ECONV+VGUESS-EO) .GT. ETOLER) GOTO 50
C
C     THE VALUE OF RO IS NOW KNOWN
C - - - - - - - - - - - - - - - - - - - - - - - - - - - - - - - - -
C
C     IF JO>O THEN CALCULATE TRAJECTORY FOR +JO AND -JO
      DO 225 IJ=1,2
      IF ((II .EQ. 1) .AND. (IJ .EQ. 2)) GOTO 225
      IF (IJ .EQ. 2) JO=-(II-1)*2.*JCONV
```

```
      RO=RGUESS
      GAMMAO=GAMMA
      PO=0.
      CALL POTEVAL(COS(GAMMAO),RO,SR,V,DVDR)
      E=((PO**2)/(2*FMU)+B*JO**2+(JO**2)
     &                    /(2*FMU*RO**2)+V*ECONV)/ECONV
C
C
C     COMPUTE TRAJECTORY
C
      IT=0
      T=0.
C     OUTPUT TO SCREEN AND TO UNIT 9
C     INITIAL CONDITIONS
      WRITE(*,'(A)')
*****************************************'
      WRITE(*,'(A)') ' T, R, P, GAMMA, J,E'
100   WRITE(*,'(6F12.5)')
     &          T,RO,PO,GAMMAO*360/(2*PI),JO/JCONV,E
      WRITE(9,'(A)') ' T, R, P, GAMMA, J,E'
      WRITE(9,'(6F12.5)')
     &          T,RO,PO,GAMMAO*360/(2*PI),JO/JCONV,E
110   CALL PROPAGATE(RO,PO,GAMMAO,JO,DELTAT)
      IF (GAMMAO .LT. (2*PI)) GOTO 120
      GAMMAO=GAMMAO-2*PI*INT(GAMMAO/(2*PI))
C
C     IF ALL POINTS ON THE TRAJECTORY ARE REQUIRED,
C     REMOVE C'S
C     WRITE(*,'(A)')
*****************************************'
C     WRITE(*,'(A)') ' T, R, P, GAMMA, J,E'
C     WRITE(*,'(6F12.5)')
T,RO,PO,GAMMAO*360/(2*PI),JO/JCONV,E
C     ENDIF
C
120   IT=IT+1
      T=T+DELTAT
      IF (RO .GT. RMAX) GOTO 200
      IF (IT .GT. MAXIT) GOTO 200
      GOTO 110
C
C     TRAJECTORY COMPLETED,
C     WRITE OUT FINAL STATE OF SYSTEM
200   CALL POTEVAL(COS(GAMMAO),RO,SR,V,DVDR)
      E=((PO**2)/(2*FMU)+B*JO**2+(JO**2)
     &                    /(2*FMU*RO**2)+V*ECONV)/ECONV
      WRITE(*,'(6F12.5)')
     &                    T,RO,PO,GAMMAO*360/(2*PI),JO/JCONV,E
      WRITE(9,'(A)') ' T, R, P, GAMMA, J,E'
      WRITE(9,'(6F12.5)')
     &                    T,RO,PO,GAMMAO*360/(2*PI),JO/JCONV,E
225   CONTINUE
250   CONTINUE
```

```
300   CONTINUE
      CLOSE(9)
      STOP
      END
C
      SUBROUTINE PROPAGATE(RO,PO,GAMMAO,JO,DELTAT)
C
C     THIS SUBROUTINE PROPAGATES THE TRAJECTORY THROUGH
C     ONE TIME STEP, DELTAT
C     USES RUNGE-KUTTA METHOD FOR SYSTEMS OF DIFFER.
C     EQUATIONS DESCRIBED IN G.A. KORN AND T.M. KORN,
C     MATHEMATICAL HANDBOOK FOR SCIENTISTS AND
C     ENGINEERS, 2ND ED. (McGRAW-HILL, NEW YORK, 1968),
C     P. 783.
C
      IMPLICIT REAL*4 (I,J,K,M,N)
      COMMON FMU,SR,JCONV,ECONV,B
      K1=DELTAT*FFUN(RO,PO,GAMMAO,JO)
      M1=DELTAT*GFUN(RO,PO,GAMMAO,JO)
      N1=DELTAT*HFUN(RO,PO,GAMMAO,JO)
      O1=DELTAT*IFUN(RO,PO,GAMMAO,JO)
      K2=DELTAT*FFUN(RO+K1/2,PO+M1/2,GAMMAO+N1/2,JO+O1/2)
      M2=DELTAT*GFUN(RO+K1/2,PO+M1/2,GAMMAO+N1/2,JO+O1/2)
      N2=DELTAT*HFUN(RO+K1/2,PO+M1/2,GAMMAO+N1/2,JO+O1/2)
      O2=DELTAT*IFUN(RO+K1/2,PO+M1/2,GAMMAO+N1/2,JO+O1/2)
      K3=DELTAT*FFUN(RO+K2/2,PO+M2/2,GAMMAO+N2/2,JO+O2/2)
      M3=DELTAT*GFUN(RO+K2/2,PO+M2/2,GAMMAO+N2/2,JO+O2/2)
      N3=DELTAT*HFUN(RO+K2/2,PO+M2/2,GAMMAO+N2/2,JO+O2/2)
      O3=DELTAT*IFUN(RO+K2/2,PO+M2/2,GAMMAO+N2/2,JO+O2/2)
      K4=DELTAT*FFUN(RO+K3,PO+M3,GAMMAO+N3,JO+O3)
      M4=DELTAT*GFUN(RO+K3,PO+M3,GAMMAO+N3,JO+O3)
      N4=DELTAT*HFUN(RO+K3,PO+M3,GAMMAO+N3,JO+O3)
      O4=DELTAT*IFUN(RO+K3,PO+M3,GAMMAO+N3,JO+O3)
      RO=RO+(K1+2*K2+2*K3+K4)/6
      PO=PO+(M1+2*M2+2*M3+M4)/6
      GAMMAO=GAMMAO+(N1+2*N2+2*N3+N4)/6
      JO=JO+(O1+2*O2+2*O3+O4)/6
      RETURN
      END
C
C
C     THESE ARE THE FOUR CLASSICAL EQUATIONS OF MOTION FOR
C     THE SYSTEM:
C
C     DR/DT
      REAL*4 FUNCTION FFUN(R,P,GAMMA,J)
      IMPLICIT REAL*4 (J,K,M,N)
      COMMON FMU,SR,JCONV,ECONV,B
      FFUN=P/FMU
      RETURN
      END
C
C     DP/DT
```

```
      REAL*4 FUNCTION GFUN(R,P,GAMMA,J)
      IMPLICIT REAL*4 (J,K,M,N)
      COMMON FMU,SR,JCONV,ECONV,B
      DR=.001
      CALL POTEVAL(COS(GAMMA),R+DR,SR,POT1,DVDR)
      CALL POTEVAL(COS(GAMMA),R-DR,SR,POT2,DVDR)
      DVDR=(POT1-POT2)/(2.*DR)
      DVDR=DVDR*ECONV
      GFUN=J**2/(FMU*R**3) - DVDR
      RETURN
      END
C
C     DGAMMA/DT
      REAL*4 FUNCTION HFUN(R,P,GAMMA,J)
      IMPLICIT REAL*4 (J,K,M,N)
      COMMON FMU,SR,JCONV,ECONV,B
      HFUN=2*B*J+J/(FMU*R**2)
      RETURN
      END
C
C     DJ/DT
      REAL*4 FUNCTION IFUN(R,P,GAMMA,J)
      IMPLICIT REAL*4 (I,J,K,M,N)
      COMMON FMU,SR,JCONV,ECONV,B
      DG=0.0001
      CALL POTEVAL(COS(GAMMA+DG),R,SR,POT1,DVDR)
      CALL POTEVAL(COS(GAMMA-DG),R,SR,POT2,DVDR)
      DVDG=(POT1-POT2)*ECONV/(2*DG)
      IFUN=-DVDG
      RETURN
      END
```

APPENDIX B

Program for Extraction of Rotational Populations from Probe Laser Spectrum

"POP" is a VAX-FORTRAN program to extract rotational populations by simulating line intensities in $^1\Sigma$-$^1\Sigma$ diatomic vibronic bands. It is designed to be run interactively on a terminal with graphics capability, so the experimental and calculated spectra can be directly compared. Except for the graphics subroutines, the program should be transportable to other computers. Since graphics capabilities are typically system-dependent, our graphics subroutines are not included here. Generic graphics calls are listed, which should be easily implemented on any system.

The calculated spectrum is determined by two sets of parameters, documented in the function FUNCTN. The first set contains the spectroscopic constants (*e.g.*, rotational constants and band origin) and experimental conditions (*e.g.*, laser lineshape and background level). The second set of parameters gives the relative populations of the rotational levels. Usually, if the spectroscopic constants are known, they are set first, and then the populations are optimized to fit the experimental spectrum.

All the program I/O is contained in the main program and is documented in the listing. The user is presented with a list of parameters or fitting options and is then given the opportunity to alter the list. If the current settings are to be retained, respond with a "/"; otherwise, input a new list, separated by commas.

```
      PROGRAM POP
C     PROGRAM TO EXTRACT ROTATIONAL POPULATIONS FROM
C     THE LASER-INDUCED FLUORESCENCE SPECTRA OF DIATOMIC
C     MOLECULES.
C     WRITTEN BY JOE I. CLINE
C     SET UP FOR SINGLET-SIGMA----->SINGLET SIGMA
C     TRANSITIONS ONLY, BUT SUBROUTINE FUNCTN
C     COULD BE MODIFIED FOR THE SELECTION RULES OF OTHER
C     TYPES OF TRANSITIONS.
C     A GAUSSIAN LASER LINESHAPE (FWHM), GAMMA, IS ASSUMED
C     MAGNETIC SUBLEVELS ARE ASSUMED TO BE STATISTICALLY
C     POPULATED, I.E., AN ISOTROPIC ORIENTATION OF THE
C     PROBED MOLECULES.
C     FOR NASCENT DIATOMIC FRAGMENTS FROM
C     PHOTODISSOCIATIONS THIS MEANS THAT NO ALIGNMENT IS
C     ASSUMED-THE METASTABLE STATE OF THE PARENT MOLECULE
C     IS LONG-LIVED.
C
C     REFERENCES:     E.U. CONDON AND G.H. SHORTLEY,
C                     THE THEORY OF ATOMIC SPECTRA
C                     (CAMBRIDGE U. PRESS, CAMBRIDGE,
C                     1935), CHAP. IV.
C
C                     G. HERZBERG
C                     MOLEC. SPECTRA AND MOLEC. STRUCTURE
C                     (VAN NOSTRAND REINHOLD, N.Y., 1950),
C                     VOL. 1.
C
C     MARQUARDT NONLINEAR LEAST SQUARES OPTIMIZATION
C     IS USED.  THE MARQUARDT PROGRAM USED HERE IS
C     A SUBSTANTIALLY MODIFIED VERSION OF THE CODE GIVEN
C     IN:
C                     P.R. BEVINGTON
C                     DATA REDUCTION AND ERROR ANALYSIS
C                     FOR THE PHYSICAL SCIENCES
C                     (McGRAW-HILL, N.Y., 1969), CHAP. 11.
C
      IMPLICIT REAL*8 (A-H,O-Z)
      CHARACTER*50 DNAME
      CHARACTER*50 PNAME
      CHARACTER*50 DUMMY
      DIMENSION XX(1200),YY(1200)
      COMMON/DATA/X(1200),Y(1200),YFIT(1200),NPTS
      COMMON/FIT/SIGMAY(60),NTERMS,MODE,DELTAA(60),
     &ASIGMA(60),FLAMDA,CHISQR,QDELTAA(60)
      COMMON/PARMS/A(60),QA(60),JUGGLE(15)
C
C     INITIALIZE FITTING PARAMETERS
C
```

```
      DO 5 I=1,10
      JUGGLE(I)=0
      DELTAA(I)=0.
      ASIGMA(I)=0.
      A(I)=0.
      QDELTAA(I)=0.
      QA(I)=0.
    5 CONTINUE
C
C     GET FILENAMES:
C     THE .SPC FILE CONTAINS THE EXPERIMENTAL SPECTRUM IN
C     THE FORMAT:
C          NPTS       -NUMBER OF POINTS IN SPECTRUM
C          XX1, YY1   -LASER FREQ., INTENS. AT POINT 1
C          XX2, YY2         "      ,    "    AT POINT 2
C          ..., ...        ...     ,   ...
C
C     THE .DAT FILE CONTAINS THE FITTING DATA IN THE
C     FORMAT:
C          NVAR, MODE     -NO. PARAMETERS, MODE NOT USED
C          NFIRST, NLAST -FIRST AND LAST POINTS TO FIT
C          CONV           -CONVERGENCE CRITERION
C          QA(1)          -PARAMETER NO. 1
C          QA(2)          -PARAMETER NO. 2
C          ...               ...
C          QA(NVAR)
C          QDELTAA(1)     -INCREMENT FOR PARAMETER NO. 1
C          ...
C          QDELTA(NVAR)
C
      WRITE (*,10)
   10 FORMAT(' INPUT NAME OF SPC FILE:')
      READ (*,20) DNAME
   20 FORMAT (A)
      OPEN (1,FILE=DNAME,STATUS='OLD')
      WRITE (*,30)
   30 FORMAT(' INPUT NAME OF DAT FILE:')
      READ (*,20) PNAME
      OPEN (2,FILE=PNAME,STATUS='OLD')
C
C     READ IN FIT PARAMETERS
C
      READ (2,'(2I6)') NVAR,MODE
      MODE=0
      READ (2,'(2I6)') NFIRST,NLAST
      READ (2,'(F20.0)') CONV
      IF (CONV.EQ.0.) CONV=1.E-6
      IF (CONV.LT.0.) CONV=1.E-6
C
C     READ IN DATA SET
C
      READ (1,'(I6)') NPTSX
      DO 40  I=1,NPTSX
```

```
      READ (1,'(3F20.0)') XX(I),YY(I),YFIT(I)
   40 CONTINUE
      CLOSE(1)
C
      DO 50 I=1,NVAR
   50 READ (2,'(F20.0)') QA(I)
C
      DO 60 I=1,NVAR
   60 READ (2,'(F20.0)') QDELTAA(I)
C
   70 CLOSE(2)
C
C     ASSIGN X,Y MATRICES FOR DATA RANGE SELECTED
C     ONLY DATA IN THE SELECTED RANGE WILL BE FIT
C     THESE DATA ARE SUPPLIED TO CURFIT IN THE X,Y ARRAYS.
C
      CALL RANGE(NPTS,NFIRST,NLAST,X,Y,XX,YY)
C
C
      IFLAG=-1
      NTERMS=0
C
C     WRITE SPECTROSCOPIC PARAMETERS TO SCREEN
  400 WRITE(*,410) (QA(J),J=1,15)
  410 FORMAT ((3F20.10))
C
C     READ IN ANY CHANGES TO PARAMETERS
C     IF PARAMETER NO. 1 .LT. 0 THEN TERMINATE PROGRAM.
      READ(*,*) (QA(J),J=1,15)
      IF (QA(1) .LT. 0.) GOTO 2020
C
C     WRITE POPULATION PARAMETERS TO SCREEN
      WRITE(*,410) (QA(J),J=20,60)
C
C     READ IN ANY CHANGES
      READ(*,*) (QA(J),J=20,60)
      WRITE(*,410) (QDELTAA(J),J=1,15)
      READ(*,*) (QDELTAA(J),J=1,15)
C
C     OPPORTUNITY TO ALTER CONVERGENCE CRITERION
      WRITE(*,'(F20.10)') CONV
      READ(*,*) CONV
C
C     INPUT FIRST AND LAST POINTS TO FIT
      WRITE(*,'(2I6)') NFIRST,NLAST
      READ(*,*) NFIRST,NLAST
      CALL RANGE(NPTS,NFIRST,NLAST,X,Y,XX,YY)
C
C     READ IN NTERMS, THE NUMBER OF PARAMETERS TO FIT
C     FOLLOWED BY THE LIST OF NTERMS PARAMETER NUMBERS.
      WRITE(*,420) NTERMS,(JUGGLE(J),J=1,15)
      READ(*,*) NTERMS,(JUGGLE(J),J=1,15)
  420 FORMAT (I4,(10I4))
```

```
C
      IF (NTERMS .EQ. 0) THEN
C     IF NOT FITTING ANYTHING, JUST CALCULATE THE ERROR
      DO 427 K=1,NPTS
  427   YFIT(K)=FUNCTN(X,K,QA)
        NFREE=NPTS-NTERMS
      CHISQR=FCHISQ(Y,SIGMAY,NPTS,NFREE,MODE,YFIT)
      WRITE(*,217) CHISQR
      GOTO 300
C     NOW JUMP TO PLOT ROUTINE
      ENDIF
C
C     THE FIRST NTERMS PARAMETERS IN JUGGLE() ARE TO BE
C     FIT, TRANSFER THE PROPER VALUES FROM QA() TO A().
C     CURFIT WILL OPTIMIZE THE PARAMETERS IN A().
      CALL ORDERA(JUGGLE,A,QA,DELTAA,QDELTAA,NTERMS)
C
C
C     INITIALIZE COUNTERS AND MARQUARDT PARAMETER
      FLAMDA=.001
      I=0
      IFLAG=0
C
C     WRITE PROGRESS OF ITERATION TO SCREEN
  200 WRITE (*,205) I
  205 FORMAT (' ITERATION NO ',I6)
      DO 210 J=1,NTERMS
C     WRITE PARAMETER, VALUE, ESTIMATED UNCERTAINTY
  210 WRITE (*,215)  J,A(J),ASIGMA(J)
  215 FORMAT (' A(',I3,')=',E20.10,E20.10)
      IF(I.EQ.0) GOTO 100
      WRITE (*,217)  CHISQR
  217 FORMAT (' CHISQR=',E20.10)
      IF (IFLAG.EQ.1) GOTO 300
C
  100 CALL CURFIT
C     CURFIT DOES THE NON-LINEAR OPTIMIZATION
      IF (I .GT. 0) GOTO 105
      ACHISQR=CHISQR
      I=I+1
      GOTO 200
105   DIFF=(ACHISQR-CHISQR)/ACHISQR
      I=I+1
      ACHISQR=CHISQR
C     CHECK FOR CONVERGENCE TOLERANCE
      IF (DIFF.GT.CONV) GOTO 200
      IFLAG=1
      GOTO 200
  300 CONTINUE
C
C     PLOT ROUTINE
C
C     CALCULATE LIMITS FOR PLOTTING
```

```
      XMIN=X(1)
      XMAX=X(1)
      YMIN=Y(1)
      YMAX=Y(1)
      DO 510 I=1,NPTS
      IF (X(I) .GT. XMAX) XMAX=X(I)
      IF (X(I) .LT. XMIN) XMIN=X(I)
      IF (Y(I) .GT. YMAX) YMAX=Y(I)
      IF (YFIT(I) .GT. YMAX) YMAX=YFIT(I)
      IF (Y(I) .LT. YMIN) YMIN=Y(I)
  510 IF (YFIT(I) .LT. YMIN) YMIN=YFIT(I)
      WRITE(*,'(4F20.10)') XMIN,XMAX,YMIN,YMAX
C!!!!!!!!!!!!!!!!!!!!!!!!!!!!!!!!!!!!!!!!!!!!!!!!!!!!!!!!!!!!!
C     THESE ARE GRAPHICS CALLS TO SYSTEM-DEPENDENT
C     SUBROUTINES, ONLY THEIR GENERIC FUNCTION
C     IS DESCRIBED.  THEY ARE ASSUMED SINGLE PRECISION.
C
C     INITIALIZE GRAPHICS MODE
      CALL GSTART
C
C     SET UP PLOT LIMITS ON PLOT DEVICE
      CALL MAP(SNGL(XMIN), SNGL(XMAX), SNGL(YMIN),
     & SNGL(YMAX))
C     DRAW AXES, NOT CURRENTLY IMPLEMENTED
C      CALL AXIS(SNGL(XMIN), SNGL(XMAX), SNGL(YMIN),
C    & SNGL(YMAX), .TRUE.)
C     PLOT INITIAL POINT OF EXPERIMENTAL SPECTRUM
      CALL POINT(SNGL(X(1)),SNGL(Y(1)))
C     JOIN SUBSEQUENT DATA POINTS TO THE FIRST
      DO 515 I=2,NPTS
  515 CALL JOIN(SNGL(X(I)),SNGL(Y(I)))
C     PLOT THE CALCULATED SPECTRUM
      CALL POINT(SNGL(X(1)),SNGL(YFIT(1)))
      DO 517 I=2,NPTS
  517 CALL JOIN(SNGL(X(I)),SNGL(YFIT(I)))
      READ(*,20) DUMMY
C!!!!!!!!!!!!!!!!!!!!!!!!!!!!!!!!!!!!!!!!!!!!!!!!!!!!!!!!!!!!!
C
C     PLOTTING IS COMPLETE.
C     NOW JUMP BACK TO INPUT SECTION TO DO ANOTHER FIT.
      GOTO 400
C
C
C     FITTING IS COMPLETED. BEFORE TERMINATING,
C     WRITE CALCULATED SPECTRUM TO SPC FILE
2020  OPEN (1,FILE=DNAME,STATUS='OLD')
      WRITE (1,'(I6)') NPTSX
      DO 2010 I=1,NPTSX
      IF (I .GE. NFIRST) THEN
        IF (I .LE. NLAST) THEN
          WRITE (1,'(3E20.10)')
     &            XX(I),YY(I),YFIT(I-NFIRST+1)
        ELSE
```

```
          WRITE (1,'(3E20.10)') XX(I),YY(I)
        ENDIF
      ELSE
        WRITE (1,'(3E20.10)') XX(I),YY(I)
      ENDIF
 2010 CONTINUE
C
C     WRITE UPDATED PARAMETERS TO DAT FILE.
      OPEN (2,FILE=PNAME,STATUS='OLD')
      WRITE (2,'(2I6)') NVAR,MODE
      WRITE (2,'(2I6)') NFIRST, NLAST
      WRITE (2,'(E20.10)') CONV
      DO 1000 I=1,NVAR
 1000 WRITE (2,'(E20.10)') QA(I)
      DO 1010 I=1,NVAR
 1010 WRITE (2,'(E20.10)') QDELTAA(I)
 1020 CLOSE (2)
      END
C
C
C*****************************************************************
C
C
      SUBROUTINE RANGE(NPTS,NFIRST,NLAST,X,Y,XX,YY)
      IMPLICIT REAL*8 (A-H,O-Z)
      DIMENSION X(1200),Y(1200),XX(1200),YY(1200)
C
C     ASSIGN X,Y MATRICES FOR DATA RANGE SELECTED
      NPTS=NLAST-NFIRST+1
C
   41 DO 43 I=1, NPTS
      X(I)=XX(NFIRST+I-1)
      Y(I)=YY(NFIRST+I-1)
   43 CONTINUE
      RETURN
      END
C
C
C*****************************************************************
C
C
C       SUBROUTINE CURFIT: ADAPTED FROM P.R. BEVINGTON
C       DATA REDUCTION AND ERROR ANALYSIS FOR THE
C       PHYSICAL SCIENCES
C       (McGRAW-HILL, N.Y., 1969), P. 237.
C     THE MARQUARDT ALGORITHM FOR LEAST-SQUARES FIT OF
C     AN ARBITRARY FUNCTION TO DATA IS DESCRIBED THEREIN.
C
      SUBROUTINE CURFIT
      IMPLICIT REAL*8 (A-H,O-Z)
      DIMENSION WEIGHT(1200),ALPHA(15,15),BETA(15),
     1 DERIV(15),ARRAY(15,15),B(15)
      COMMON/DATA/X(1200),Y(1200),YFIT(1200),NPTS
```

```
      COMMON/FIT/SIGMAY(60),NTERMS,MODE,DELTAA(60),
     1 ASIGMA(60),FLAMDA,CHISQR,QDELTAA(60)
      COMMON/PARMS/A(60),QA(60),JUGGLE(15)
   11 NFREE=NPTS-NTERMS
      IF (NFREE) 13,13,20
   13 CHISQR=0.
      GOTO 110
C
C        EVALUATE WEIGHTS
C     IN THIS PROGRAM MODE IS FIXED AT ZERO.
C     (EQUAL WEIGHTING OF ALL POINTS)
C
   20 DO 30 I=1, NPTS
   21 IF (MODE) 22,27,29
   22 IF (Y(I)) 25,27,23
   23 WEIGHT(I)=1./Y(I)
      GOTO 30
   25 WEIGHT(I)=1./(-Y(I))
      GOTO 30
   27 WEIGHT(I)=1.
      GOTO 30
   29 WEIGHT(I)=1./SIGMAY(I)**2
   30 CONTINUE
C
C        EVALUATE ALPHA AND BETA MATRICES
C
   31 DO 34 J=1,NTERMS
      BETA(J)=0.
      DO 34 K=1,J
   34 ALPHA(J,K)=0.
      CALL ORDERA(JUGGLE,A,QA,DELTAA,QDELTAA,NTERMS)
   41 DO 50 I=1,NPTS
      CALL FDERIV(X,I,A,DELTAA,NTERMS,DERIV,JUGGLE,QA)
      DO 46 J=1,NTERMS
      BETA(J)=BETA(J)+WEIGHT(I)*(Y(I)
     &                    -FUNCTN(X,I,QA))*DERIV(J)
      DO 46 K=1,J
   46 ALPHA(J,K)=ALPHA(J,K)+WEIGHT(I)*DERIV(J)*DERIV(K)
   50 CONTINUE
   51 DO 53 J=1,NTERMS
      DO 53 K=1,J
   53 ALPHA(K,J)=ALPHA(J,K)
C
C        EVALUATE CHI SQUARE AT STARTING POINT
C
   61 DO 62 I=1,NPTS
   62 YFIT(I)=FUNCTN(X,I,QA)
   63 ACHISQR = FCHISQ (Y,SIGMAY,NPTS,NFREE,MODE,YFIT)
C
C  INVERT MODIFIED CURVATURE MATRIX TO FIND NEW PARAMETERS
C
   71 DO 74 J=1,NTERMS
      DO 73 K=1,NTERMS
```

```
   73 ARRAY(J,K)=ALPHA(J,K)/SQRT(ALPHA(J,J)*ALPHA(K,K))
   74 ARRAY(J,J)=1.+FLAMDA
   80 CALL MATINV(ARRAY,NTERMS,DET)
   81 DO 84 J=1,NTERMS
      B(J)=A(J)
      DO 84 K=1,NTERMS
   84 B(J)=B(J)+BETA(K)*ARRAY(J,K)
     &                 /SQRT(ALPHA(J,J)*ALPHA(K,K))
C
C       IF CHI SQUARE INCREASED,
C                  INCREASE FLAMDA AND TRY AGAIN
C
      CALL ORDERQA(JUGGLE,B,QA,NTERMS)
   91 DO 92 I=1,NPTS
   92 YFIT(I)=FUNCTN(X,I,QA)
   93 CHISQR=FCHISQ(Y,SIGMAY,NPTS,NFREE,MODE,YFIT)
      IF (ACHISQR-CHISQR) 95,101,101
   95 FLAMDA=10.*FLAMDA
      GOTO 71
C
C       EVALUATE PARAMETERS AND UNCERTAINTIES
C
  101 DO 103 J=1,NTERMS
      A(J)=B(J)
  103 ASIGMA(J)=SQRT(ARRAY(J,J)/ALPHA(J,J))
      FLAMDA=FLAMDA/10.
110   RETURN
      END
C
C
C*************************************************************
C
C
      SUBROUTINE ORDERA(JUGGLE,A,QA,DELTAA,QDELTAA,NTERMS)
C     STUFF PROPER VALUES FROM QA() PARAMETER ARRAY
C     INTO A() FOR OPTIMIZATION BY CURFIT
C
      IMPLICIT REAL*8 (A-H,O-Z)
      DIMENSION JUGGLE(15),A(60),QA(60),
     &                        DELTAA(60),QDELTAA(60)
      DO 100 I=1,NTERMS
      A(I)=QA(JUGGLE(I))
      DELTAA(I)=QDELTAA(JUGGLE(I))
  100 CONTINUE
      RETURN
      END
C
C
C*************************************************************
C
C

      SUBROUTINE ORDERQA(JUGGLE,A,QA,NTERMS)
```

```
C     FOLLOWING THE FITTING, UPDATE QA() WITH THE
C          OPTIMIZED PARAMETERS
C
      IMPLICIT REAL*8 (A-H,O-Z)
      DIMENSION JUGGLE(15),A(60),QA(60)
      DO 100 I=1,NTERMS
      QA(JUGGLE(I))=A(I)
  100 CONTINUE
      RETURN
      END
C
C
C*************************************************************
C
C
C       FUNCTION FCHISQ: ADAPTED FROM P.R. BEVINGTON
C       DATA REDUCTION AND ERROR ANALYSIS
C       P. 194.
C     CALCULATE ERROR: GIVEN BY THE SUM OF THE SQUARES
C     OF THE DIFFERENCES OF THE EXPERIMENTAL AND
C     CALCULATED INTENSITIES.
C
      FUNCTION FCHISQ (Y,SIGMAY,NPTS,NFREE,MODE,YFIT)
      IMPLICIT REAL*8 (A-H,O-Z)
      DIMENSION Y(1200),SIGMAY(1200),YFIT(1200)
   11 CHISQ=0.
   12 IF (NFREE) 13,13,20
   13 FCHISQ = 0.
      GOTO 40
C
C       ACCUMULATE CHI SQUARE
C
   20 DO 30 I=1, NPTS
   21 IF (MODE) 22,27,29
C     IN THIS PROGRAM, MODE IS FIXED AT ZERO.
   22 IF (Y(I)) 25,27,23
   23 WEIGHT=1./Y(I)
      GOTO 30
   27 WEIGHT=1.
      GOTO 30
   25 WEIGHT=1./(-Y(I))
      GOTO 30
   29 WEIGHT=1./SIGMAY(I)**2
   30 CHISQ=CHISQ+WEIGHT*(Y(I)-YFIT(I))**2
C
C       DIVIDE BY NUMBER OF DEGREES OF FREEDOM
C
   31 FREE=NFREE
   32 FCHISQ=CHISQ/FREE
   40 RETURN
      END
C
C
```

```
C*****************************************************************
C
C
C       SUBROUTINE MATINV: ADAPTED FROM P.R. BEVINGTON
C       DATA REDUCTION AND ERROR ANALYSIS
C     INVERT A SYMMETRIC MATRIX, ALSO CALCULATES
C     ITS DETERMINANT
C
      SUBROUTINE MATINV (ARRAY,NORDER,DET)
      IMPLICIT REAL*8 (A-H,O-Z)
      DIMENSION ARRAY(15,15),IK(15),JK(15)
   10 DET=1.
   11 DO 100 K=1,NORDER
C
C       FIND LARGEST ELEMENT ARRAY(I,J) IN REST OF MATRIX
C
      AMAX=0.
   21 DO 30 I=K,NORDER
      DO 30 J=K,NORDER
   23 IF (ABS(AMAX)-ABS(ARRAY(I,J))) 24,24,30
   24 AMAX=ARRAY(I,J)
      IK(K)=I
      JK(K)=J
   30 CONTINUE
C
C       INTERCHANGE ROWS AND COLUMNS TO PUT AMAX IN
C           ARRAY(K,K)
C
   31 IF (AMAX) 41,32,41
   32 DET=0.
      GOTO 140
   41 I=IK(K)
      IF (I-K) 21,51,43
   43 DO 50 J=1,NORDER
      SAVE=ARRAY(K,J)
      ARRAY(K,J)=ARRAY(I,J)
   50 ARRAY(I,J)=-SAVE
   51 J=JK(K)
      IF (J-K) 21,61,53
   53 DO 60 I=1,NORDER
      SAVE=ARRAY(I,K)
      ARRAY(I,K)=ARRAY(I,J)
   60 ARRAY(I,J)=-SAVE
C
C       ACCUMULATE ELEMENTS OF INVERSE MATRIX
C
   61 DO 70 I=1,NORDER
      IF (I-K) 63,70,63
   63 ARRAY(I,K)=-ARRAY(I,K)/AMAX
   70 CONTINUE
   71 DO 80 I=1,NORDER
      DO 80 J=1,NORDER
      IF (I-K) 74,80,74
```

```
   74 IF (J-K) 75,80,75
   75 ARRAY(I,J)=ARRAY(I,J)+ARRAY(I,K)*ARRAY(K,J)
   80 CONTINUE
   81 DO 90 J=1,NORDER
      IF (J-K) 83,90,83
   83 ARRAY(K,J)=ARRAY(K,J)/AMAX
   90 CONTINUE
      ARRAY(K,K)=1./AMAX
  100 DET=DET*AMAX
C
C       RESTORE ORDERING OF MATRIX
C
  101 DO 130 L=1,NORDER
      K=NORDER-L+1
      J=IK(K)
      IF (J-K) 111,111,105
  105 DO 110 I=1,NORDER
      SAVE=ARRAY(I,K)
      ARRAY(I,K)=-ARRAY(I,J)
  110 ARRAY(I,J)=SAVE
  111 I=JK(K)
      IF (I-K) 130,130,113
  113 DO 120 J=1,NORDER
      SAVE=ARRAY(K,J)
      ARRAY(K,J)=-ARRAY(I,J)
  120 ARRAY(I,J)=SAVE
  130 CONTINUE
  140 RETURN
      END
C
C
C*************************************************************
C
C
      FUNCTION FUNCTN (X,I,A)
C     THIS SUBROUTINE CALCULATES THE INTENSITY AT
C     THE POINT X(I) FOR THE PARAMETER ARRAY A().
C     THE PARAMETERS HAVE FOLLOWING SIGNIFICANCE
C     TO FUNCTN:
C     A(2) IS THE GAUSSIAN LASER LINEWIDTH CM-1, FWHM
C     A(3) IS THE LASER FREQUENCY CORRECTION, IN CM-1
C     A(5) IS THE FREQUENCY OF THE BAND ORIGIN, CM-1
C     A(6) BV ROT. CONSTANT FOR LOWER ELECTRONIC STATE
C     A(7) BV ROT. CONSTANT FOR UPPER ELEC. STATE
C     A(8) JMAX, THE HIGHEST POPULATED ROTATIONAL LEVEL
C     A(9) THE BACKGROUND NOISE LEVEL: THE BASELINE
C     A(10) DV DISTORTION CONSTANT FOR LOWER ELEC. STATE
C     A(11) DV FOR UPPER ELEC. STATE
C     A(20)-A(20+JMAX) RELATIVE POPULATIONS OF ROTATIONAL
C          LEVELS , E.G. A(20) IS THE POPULATION OF J=0
C                        A(21) IS THE POPULATION OF J=1
C                        A(20+JMAX) IS POPN. OF J=JMAX.
C     PARAMETERS 4 AND 11-19 ARE UNUSED IN THE CURRENT
```

```
C     PROGRAM.
C
      IMPLICIT REAL*8 (A-H,O-Z)
      COMMON/LINES/ R(50),P(50),RINTENS(50),
     &                    PINTENS(50),JMAX
      DIMENSION X(1200),A(60)
   20 FORMAT(A)
      JMAX=IDINT(A(8))
C     PUT FREQUENCY POSITIONS OF R- AND P- BRANCH LINES
C     INTO R() AND P()
      CALL LINEPOS(JMAX,R,P,A)
C     PUT INTENSITIES OF LINES INTO RINTENS AND PINTENS
      CALL INTENS(JMAX,R,P,A,RINTENS,PINTENS)
      FUNCTN=0.
C
C     CALCULATE INTENSITY AT X(I)
C     SUM UP CONTRIBUTIONS OF EACH CONVOLUTED LINE IN
C     IN THE SPECTRUM:
      DO 300 J=1,JMAX+1
C     R-BRANCH
      FUNCTN=FUNCTN+RINTENS(J)*GAUSS(X(I),R(J),A(2))
  300 CONTINUE
C     P-BRANCH
      DO 400 J=1,JMAX
      FUNCTN=FUNCTN+PINTENS(J)*GAUSS(X(I),P(J),A(2))
  400 CONTINUE
C
C     ADD IN THE BACKGROUND TO THE INTENSITY
      FUNCTN=FUNCTN+A(9)
      RETURN
      END
C
C
C*************************************************************
C
C
      FUNCTION GAUSS (W,WO,FWHM)
      IMPLICIT REAL*8 (A-H,O-Z)
C     COMPUTES GAUSSIAN CONVOLUTION FUNCTION
C     WO IS CENTER OF GAUSSIAN
C     FWHM IS FWHM OF GAUSSIAN
C     1.0 IS PEAK HEIGHT
C     W IS POINT TO CALC. GAUSSIAN
      Z=(W-WO)/FWHM
      IF (Z**2 .GT. 10.0D+00) THEN
        GAUSS=0.
        GOTO 100
      ENDIF
      C=4.0*DLOG(2.0D0)
      GAUSS=DEXP(-C*Z**2)
  100 RETURN
      END
C
```

```
C
C*****************************************************************
C
C
      SUBROUTINE LINEPOS(JMAX,R,P,A)
C     CALCULATES THE FREQUENCIES OF THE P- AND R- BRANCH
C     LINES, USING THE ROTATIONAL CONSTANTS
C     AND DISTORTION CONSTANTS FOR EACH ELECTRONIC STATE.
      IMPLICIT REAL*8 (A-H,O-Z)
      DIMENSION R(50),P(50)
      DIMENSION A(60)
      DO 100 J=0, JMAX
      EB=A(6)*J*(J+1)-A(10)*(J*(J+1))**2
      K=J+1
      EEPLUS=A(7)*K*(K+1)-A(11)*(J*(J+1))**2
      R(J+1)=EEPLUS-EB+A(5)+A(3)
      IF (J .GT. 0) THEN
         K=J-1
         EEMINUS=A(7)*K*(K+1)-A(11)*(J*(J+1))**2
         P(J)=EEMINUS-EB+A(5)+A(3)
      ENDIF
  100 CONTINUE
      RETURN
      END
C
C
C*****************************************************************
C
C

      SUBROUTINE INTENS(JMAX,R,P,A,RINTENS,PINTENS)
C     COMPUTE INTENSITY OF EACH LINE
C     USING THE POPULATIONS, A(20)...A(20+JMAX).
C     MUST BE CORRECTED FOR HONL-LONDON FACTORS
C     SEE, FOR EXAMPLE, HERZBERG, MOLECULAR SPECTRA AND
C     MOLEC. STRUCTURE, VOL. 1., P. 208, AND EQ. 2
C     OF CHAPTER 3 OF JIC CALTECH THESIS.
C
      IMPLICIT REAL*8 (A-H,O-Z)
      DIMENSION R(50),P(50),A(60),RINTENS(50),PINTENS(50)
      RINTENS(1)=A(20)
      DO 100 J=1,JMAX
      RINTENS(J+1)=A(J+20)*(J+1)/(2*J+1)
      PINTENS(J)=A(J+20)*J/(2*J+1)
  100 CONTINUE
      RETURN
      END
C
C
C*****************************************************************
C
C
      SUBROUTINE FDERIV (X,I,A,DELTAA,NTERMS,
```

```
     &                                DERIV,JUGGLE,QA)
C     CALCULATES DERIVATIVES OF FUNCTION FUNCTN
C     WITH RESPECT TO THE FITTING PARAMETERS, QA()
C     DERIVATIVES ARE CALCULATED NUMERICALLY
C     USING THE INCREMENTS IN DELTAA().
      IMPLICIT REAL*8 (A-H, O-Z)
      DIMENSION X(1200),A(60),DELTAA(60),DERIV(60),
     &                                JUGGLE(15),QA(60)
   11 DO 18 J=1,NTERMS
      AJ=A(J)
      DELTA=DELTAA(J)
      A(J)=AJ+DELTA
      CALL ORDERQA(JUGGLE,A,QA,NTERMS)
      YFIT=FUNCTN(X,I,QA)
      A(J)=AJ-DELTA
      CALL ORDERQA(JUGGLE,A,QA,NTERMS)
      DERIV(J)=(YFIT-FUNCTN(X,I,QA))/(2.*DELTA)
      A(J)=AJ
   18 CALL ORDERQA(JUGGLE,A,QA,NTERMS)
      RETURN
      END
```